FALL/WINTER 2013
VOLUME 5, NUMBER 2

Print ISSN: 2152-4157
Online ISSN: 2152-4165

WWW.IJERI.ORG

International Journal of Engineering Research & Innovation

Editor-in-Chief: Mark Rajai, Ph.D.
California State University Northridge

Published by the
International Association of Journals & Conferences

INTERNATIONAL JOURNAL OF ENGINEERING RESEARCH AND INNOVATION

The INTERNATIONAL JOURNAL OF ENGINEERING RESEARCH AND INNOVATION (IJERI) is an independent and nonprofit publication, which aims to provide the engineering community with a resource and forum for scholarly expression and reflection.

IJERI is published twice annually (Fall and Spring issues) and includes peer-reviewed research articles, editorials, and commentary that contribute to our understanding of the issues, problems, and research associated with the engineering and related fields. The journal encourages the submission of manuscripts from private, public, and academic sectors. The views expressed are those of the authors, and do not necessarily reflect the opinions of the IJERI or its editors.

EDITORIAL OFFICE:

Mark Rajai, Ph.D.
Editor-in-Chief
Office: (818) 677-2167
Email: ijmeeditor@iajc.org
Dept. of Manufacturing Systems Engineering & Management
California State University-Northridge
18111 Nordhoff Street
Northridge, CA 91330-8332

TABLE OF CONTENTS

The editors and staff at IAJC would like to thank you, our readers, for your continued support, and we look forward to seeing you at the upcoming IAJC conference. For this fourth IAJC conference, we will be partnering with the International Society of Agile Manufacturing (ISAM). This event will be held at the new Embassy Suites hotel in Orlando, FL, September 25-27, 2014, and is sponsored by IAJC, IEEE, ASEE, and the LEAN Institute.

EDITOR'S NOTE

Philip Weinsier, IJERI Manuscript Editor

Main Sponsors

The IAJC/ISAM Executive Board is pleased to invite faculty, students, researchers, engineers, and practitioners to present their latest accomplishments and innovations in all areas of engineering, engineering technology, math, science, and related technologies.

Selected papers from the conference will be published in the three IAJC-owned journals or 11 affiliate journals. Oftentimes, these papers, along with manuscripts submitted at-large, are reviewed and published in less than half the time of other journals. Publishing guidelines are available at www.iajc.org, where you can read any of our previously published journal issues, as well as obtain information on chapters, membership, and benefits.

I am pleased to report that, based on the latest impact factor (IF) calculations (Google Scholar method), the International Journal of Engineering Research and Innovation (IJERI), had a strong showing with an IF = 1.58, which is noteworthy as it is a relatively young journal (in publication since 2009). IJERI's sister journal, the International Journal of Modern Engineering (IJME), also now has a remarkable IF = 3.0 and continues its march toward the top 20 engineering journals. Any IF above 1 is considered high, based on the requirements of many top universities, and places the journals among an elite group.

Currently, there is no official ranking system for journals that publish areas of engineering the way that IJERI and IJME do, but the following still apply:

- Both IJME and IJERI now are indexed in most well-known indexing databases including DOAJ, which is the most prestigious and comprehensive database for open-access journals worldwide.
- Both journals now are indexed by hundreds of libraries worldwide, and in several states where there is near complete indexing across their university and college libraries.
- Both journals now are indexed in the libraries of all 10 campuses of the University of California system and the 23 campuses of the California State University system.

The biggest achievement, though, is that now both journals also are indexed by all of the top 10 universities in the world:

#1 California Institute of Technology
#2 Harvard
#3 Stanford
#4 University of Oxford
#5 Princeton University
#6 University of Cambridge
#7 Massachusetts Institute of Technology
#8 Imperial College London
#9 University of Chicago
#10 University of California, Berkeley

Indexed In

ISBN# 978-1-60643-379-9

Editorial Review Board Members

Listed here are the IAJC International Review Board members, who have devoted countless hours to the review of the many manuscripts that have been submitted for publication. Manuscript reviews require insight into the content, technical expertise related to the subject matter, and a familiarity with statistical tools and measures. Furthermore, revised manuscripts typically are returned for a second review to the same reviewers, as they already have an intimate knowledge of the work. So, as Manuscript Editor, I would like to take this opportunity to thank all of the members of the review board.

If you are interested in becoming a member of the IAJC International Review Board, send me (Philip Weinsier, IAJC/IRB Chair, philipw@bgsu.edu) an email to that effect. Review Board members review manuscripts in their areas of expertise for all three of our IAJC journals—IJME (the International Journal of Modern Engineering), IJERI (the International Journal of Engineering Research and Innovation), and TIIJ (the Technology Interface International Journal), as well as papers submitted to the IAJC conferences. Please watch for updates on our website (**www.IAJC.org**), and contact us anytime with comments, concerns, or suggestions.

A UNIQUE MOBILE HANDHELD PARTICULATE MONITORING DEVICE

Iem Heng, Manhattan College; Raymond Yap, Manhattan College

Abstract

This paper describes a mobile handheld particulate monitor (MHPM) used for monitoring microscopic airborne particles. This technology-enabled device, used for environmental sensing, allows users to record, broadcast, and map particulate status in real-time using a smart phone or a tablet computer. The technology is supported by a custom application (app) called AirCasting. In addition to detecting airborne particulates, the MHPM is able record variability in temperature and humidity, factors which can alter the size of the particulate material.

The data collected and processed by the MHPM is uploaded to an interactive web-based map that displays both individual and aggregated routing information. Each AirCasting session allows the user to capture real-world measurements, annotate the data, and share it with the local and world-wide community via the app. The platform also employs color-changing (green, yellow, orange, and red) particulate concentration indicators to communicate the air quality status at a particular place and time. This device provides a technological solution for mobile particulate monitoring that is especially useful for those at risk of respiratory disorders.

Introduction

Annually, the United States Environmental Protection Agency (EPA) [1] releases data on the air pollution that may impact human health. Pollution due to particulates, also known as particulate matter (PM), is a contributing factor to thousands of deaths each year. PM is a mixture of solid particles and liquid droplets found in the air. Some PM, such as dust, dirt, soot, or smoke, is large or dark enough to be seen with the naked eye. Other particulates are so small they can be detected only by using an electron microscope.

Figure 1 illustrates the different sizes of PM, ranging from combustion particulates to fine beach sand. PM with a size of 10 micrometers (µm) or larger does not significantly affect human health, and, thus, it is not regulated by the EPA. However, the EPA does monitor and regulate PM that is less than 10 µm in diameter, due to the potential for health problems that may ensue from particulate exposure [2].

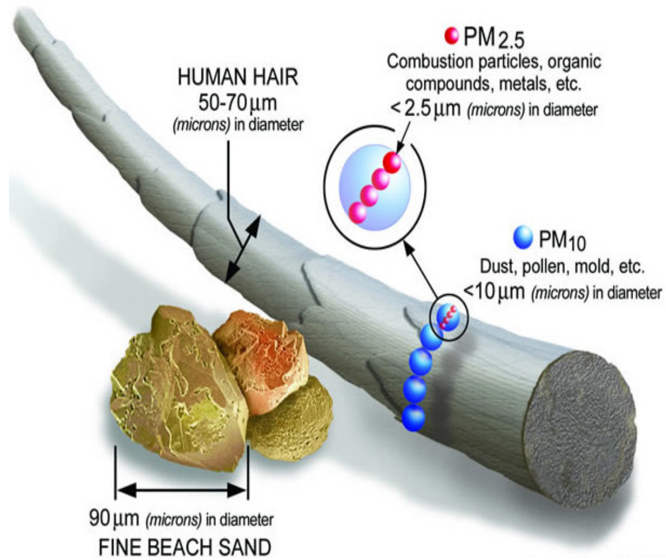

Figure 1. Typical Size for Particulates

PM can be differentiated by size. Coarse or large particles (pollen, mold, large dust, large bacteria, plant spores, dust mite feces, etc.) range in diameter between 2.5 µm and 10 µm; whereas, fine or small particles (combustion particles, organic compounds, metal, small bacteria, smoke, smog, etc.) are 2.5 µm or less.

The proposed solution has advantages over current PM monitoring systems, in that it is a portable, low cost, technology-enabled system that is user-friendly. Unlike currently available systems, the MHPM described herein is a unique and novel approach in terms of its compact size and convenience, and provides a communication link to portable devices (smart phone, tablet, and laptop). For instance, an MHPM user can walk a particular route, collect the ambient particulate data, and upload the data to an interactive web-based map that displays both the route and the aggregated particulate information. This is illustrated in Figure 2. As Figure 2 demonstrates, consumers without an MHPM still can use the AirCasting app on a portable device to check the status of particulates in areas of interest.

The objective of this paper is to present the design and construction of an MHPM that can detect PM 0.5 µm in diameter or larger, process the raw sensor data into coherent information, and interface to mobile devices. A schematic

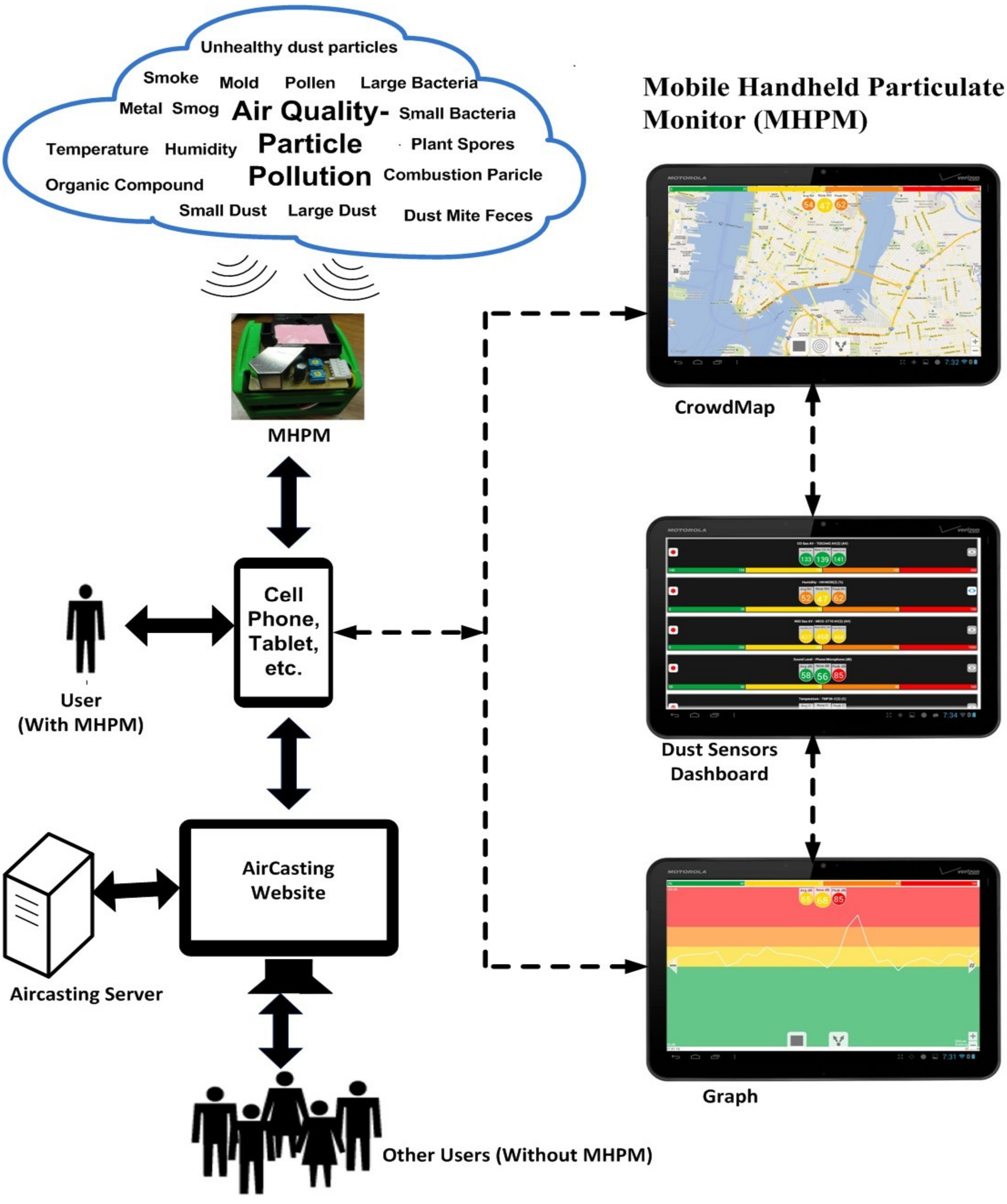

Figure 2. Overview of the MHPM and AirCasting Application

layout of MHPM was developed. Using the schematic layout, a custom-made physical prototype of the MHPM was created. The prototype was tested with portable devices to disseminate PM concentration levels via the AirCasting app.

Particulate Sensors and Sensor Calibration

This section discusses two particulate sensors and their calibration. In general, air quality sensors are available in varying sizes and shapes [3]. However, there are few compact sensors for measuring particulates 10 µm in diameter or smaller. In this study, two small form-factor sensors, the Shinyei PPD42NS [4] and the Shinyei PPD60PV-T2 [5], were used as part of the MHPM. These sensors cost $15.95 and $150.00, respectively. While the PPD60PV-T2 (T2) is an order of magnitude more expensive, it has the ability to detect particulates as small as 0.5 µm in diameter and larger, and it provides two signal outputs, one analog and one digital [6]. The PPD42NS (NS) sensor detects particulates 1.0 µm in diameter or larger, and provides one signal as a digital output. The digital output on these sensors is negative logic, and appears to be a variation on pulse width modulation, called *low pulse occupancy time*, using active low duration.

The NS is a passive sensor with 3 output pins. The 3 pins are: Vcc (voltage), GND (ground) and Sig (digital signal output). Either sensor can be connected to a microcontroller and the resulting system can be powered by a rechargeable battery pack, as illustrated in Figure 3. The T2 has similar characteristics to the NS. It is a passive dust sensor and has an active low response. However, the T2 has 6 output pins: 2 Vccs, 2 GNDs, Analog output (A_{out}), and Digital output (D_{out}). As shown in Figure 3, an analog output is available with the T2, but is not an option with the NS.

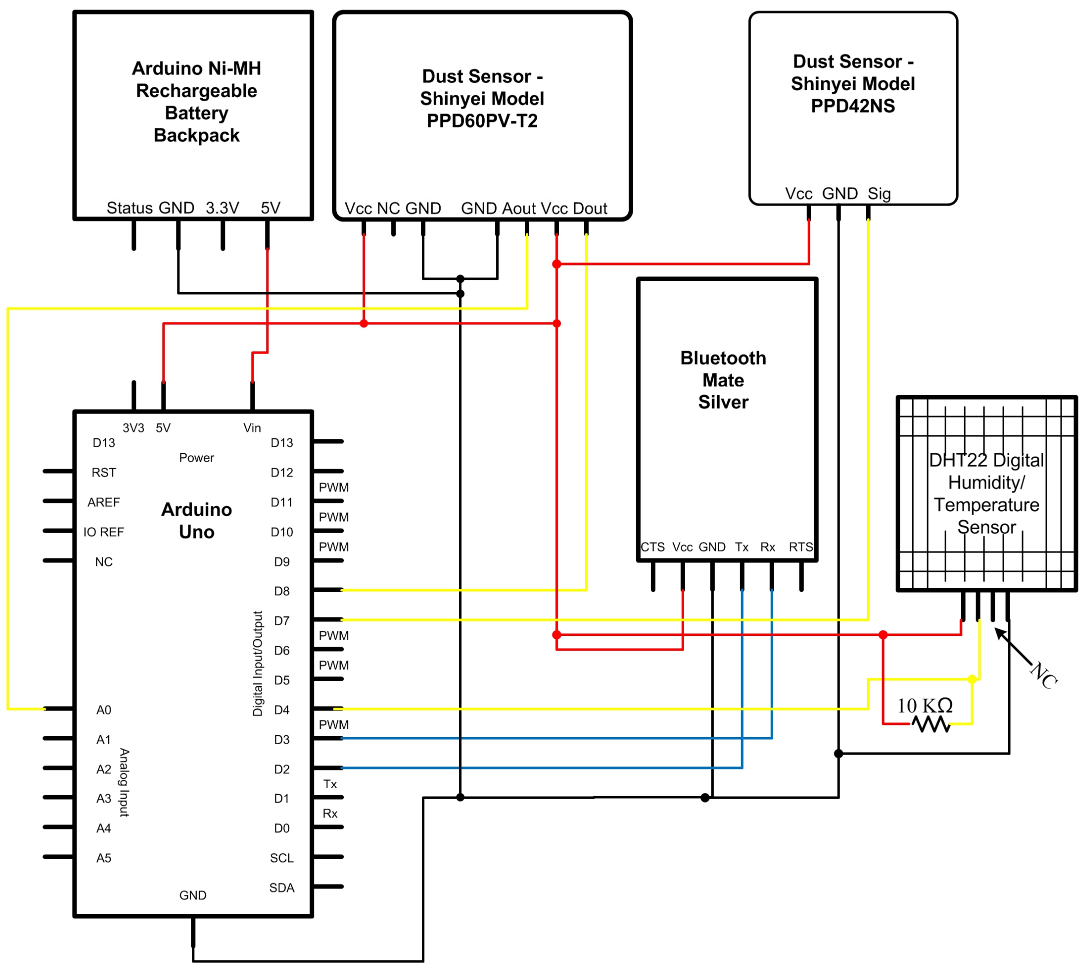

Figure 3. Schematic Layout of Dust Sensors and Humidity-Temperature Sensor

Several studies address the impact of humidity and temperature on particulate matter size [7]. To adjust for the influence of these factors, a DHT22 [8] digital humidity-temperature sensor was included as part of the MHPM system, as shown in Figure 3. This sensor (at a cost of around $9.95 per unit) has 4 output pins: Vcc, GND, Digital output (D_{out}), and NC (no connection).

The sensors provide raw signal data to the microcontroller. An Arduino part was chosen for this application. The raw signal values are processed into usable numbers that are comparable to other scales. Initially, the raw temperature sensor data is converted to the Kelvin scale using Equation (1) [9]. Then, the Celsius-Fahrenheit conversion formulas, Equations (2) and (3), are used to determine the temperature as follows:

$$\text{Kelvin} = [((\text{RSV}) / 1023.00)5]100 \quad (1)$$
$$\text{Celsius} = \text{Kelvin} - 273.15 \quad (2)$$
$$\text{Fahrenheit} = (9.00 / 5)(\text{temperature Celsius}) + 32 \quad (3)$$

Equation (1) is based on the raw signal values that correlate with the applied voltage from the microcontroller. The raw signal values range from 0 to 1023 that correlate to a voltage range of 0 to 5 volts (V). Additionally, the factor 100 in the Kelvin equation comes from the fact that the humidity-temperature sensor works like a Zener diode with a breakdown voltage proportional to the absolute temperature at 10mV/°Kelv [10]. The relative humidity can be determined by the following equations:

$$\text{MaxV} = 3.27 - [0.006706\ (\text{temperature Celsius})]$$
$$\text{RelativeHumidity} = [((\text{RSV}) / 1023.00)5 - 0.8] / ((\text{MaxV})100)$$

Note that the maximum voltage value (MaxV) drops 0.006706 for each degree Celsius over 0°C. The voltage at 0°C is 3.27. This is corrected for zero percent voltage offset, which is approximately 0.8.

Unlike the calibration of the humidity-temperature sensor, the calibration for the two Shinyei PM sensors is based on sensor tests with cigarette smoke in a confined volume of 0.01 cubic foot, per the data sheet specification [4], [5]. The tabular data for sensor calibration is shown in Table 1 and Table 2. Table 1 and Table 2 are then presented as a scatter plots, and the best-fit curves and polynomial equations for the NS and T2 calibration data are shown in Figure 4 and Figure 5, respectively.

The dust sensor calibration equations are as follows: Equation (4) is the calibration equation for the NS digital output; Equations (5) and (6) are for the T2 analog and digital outputs, respectively.

The AirCasting app uses all three equations.

$$(\text{NS})\ Y = 0.6944x^3 + 1.4861x^2 + 507.34x - 7.1779 \quad (4)$$
$$(\text{T2})\ Ya = 1244.4x^3 - 2961.9x^2 + 6007.9x - 257.14 \quad (5)$$
$$(\text{T2})\ Yd = 0.3111x^3 + 0.4268x^2 + 373.41x - 133.33 \quad (6)$$

Table 1. Shinyei PPD42NS Digital Output Concentration Data

Digital Output Data	
Low Pulse Occupancy Time	Concentration
0	0
2	1000
4	2100
6	3250
8	4500
10	5900
12	7500

Table 2. Shinyei PPD60PV-T2 Analog and Digital Output Concentration Data

Analog Output Data			Digital Output Data	
Voltage	Concent.		Low Pulse Occupancy Time	Concent.
0.0	0		0	0
0.5	1600		5	1500
1.0	4000		10	3900
1.5	6900		15	7000
2.0	10000		20	10000
2.5	15000		25	14000
3.0	25000		30	20000

Performance of the MHPM Prototype with AirCasting App

The MHPM provides important calibrated data for monitoring particulate matter. The prototype of the MHPM in Figure 2 is built from the schematic layout in Figure 3. The progressive stages of design for the MHPM physical prototype are detailed in Figure 6, which shows the physical layout of the device, including the electronic components, all sensors, and the Bluetooth module, all of which are soldered onto the breadboard. The rechargeable battery pack, breadboard, and electronic components are inserted into the protective casing, which was built using 3D rapid prototyping.

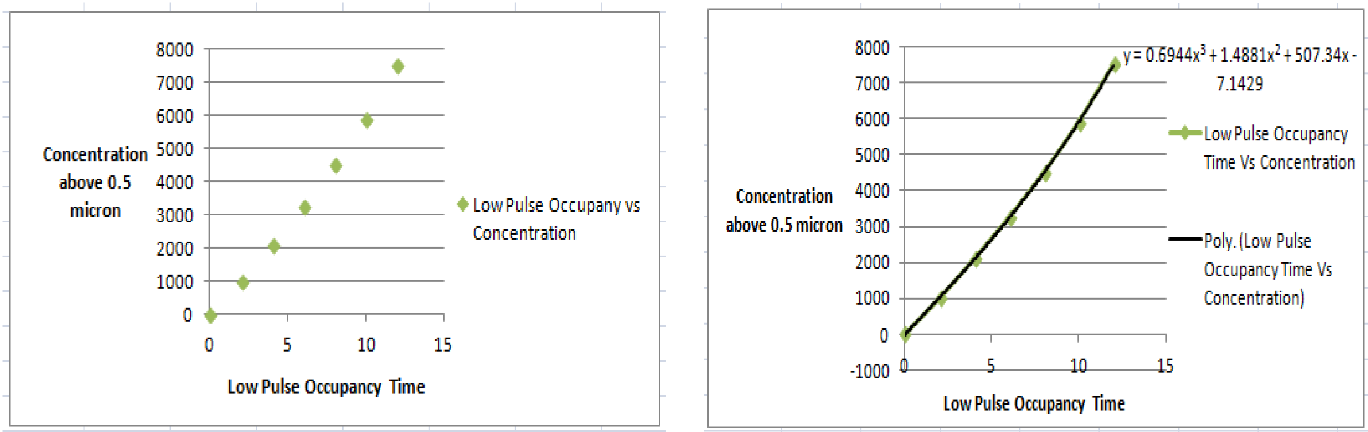

(a) Plot of Concentration Data

(b) Best-fit Fit of Concentration Data

Figure 4. Shinyei PPD42NS Best-Fit Polynomial Curve and Concentration Equation

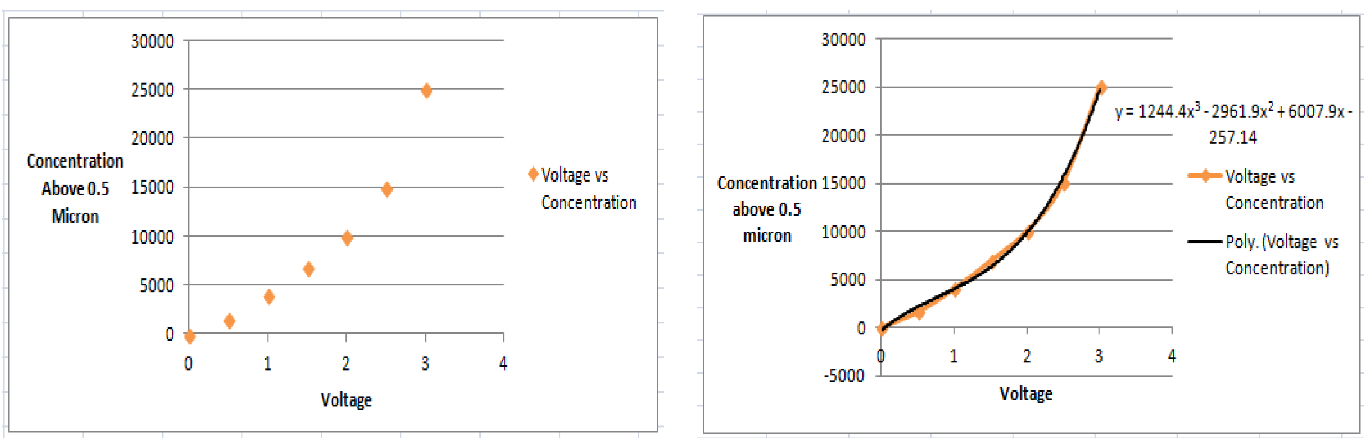

(a) Plot of Analog Output Voltage

(b) Best-fit Fit of Analog Output Voltage

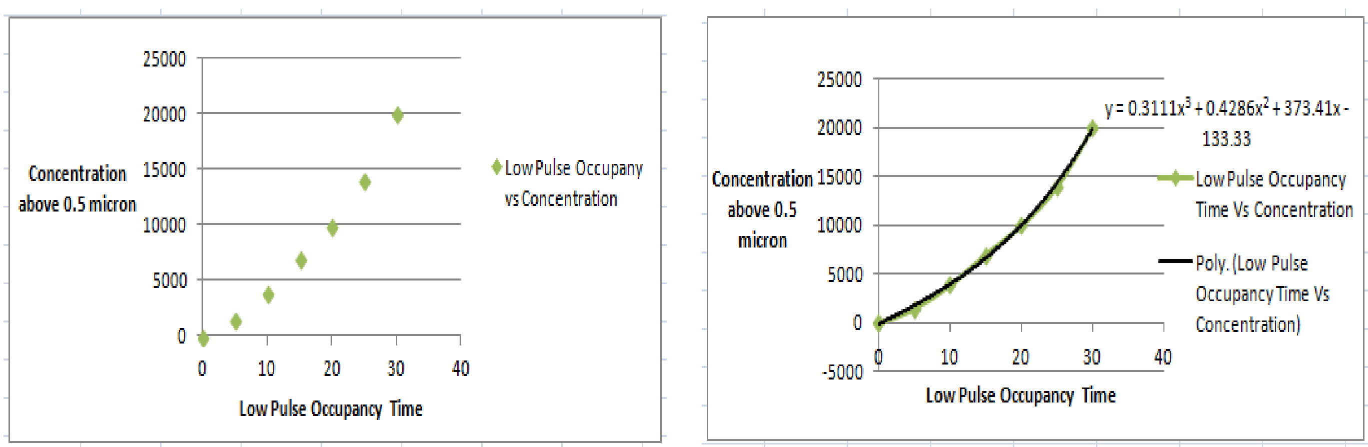

(c) Plot of Concentration Data

(d) Best-fit Fit of Concentration Data

Figure 5. Shinyei PPD60PV-T2 Best-fit Polynomial Curve and Concentration Equations

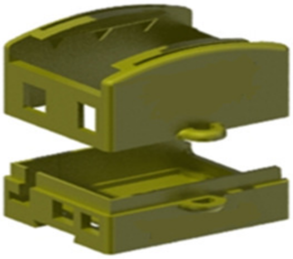

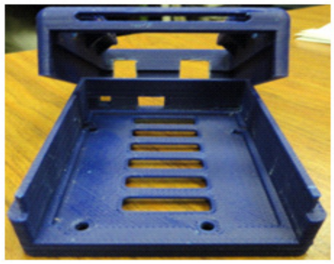

(a) 3D Computer Rendering **(b) 3D Case Rapid Prototyping**

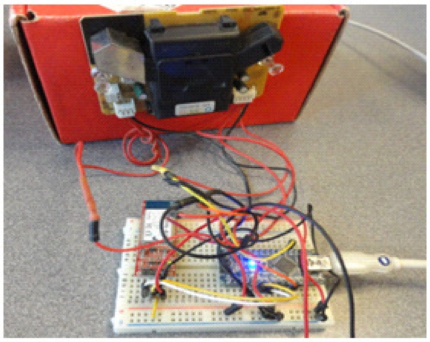

(c) Breadboard, sensorsSensors, and other Other electronic Electronic componentsComponents

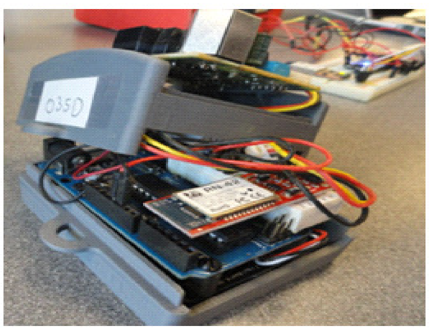

(d) Combination of caseCase, battery Battery packPack, Arduino, sensorsSensors, Bluetooth, electronic Electronic componentsComponents

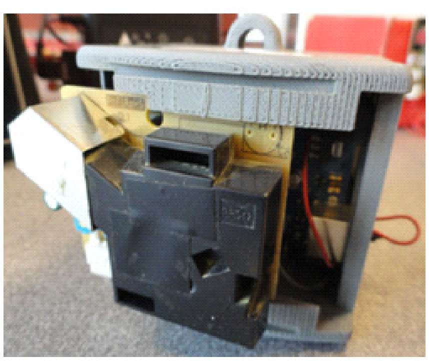

(e) Final prototype Prototype of MHPM

Figure 6. Design Stages of the MHPM Prototype

For an accurate particulate reading (PM) from either sensor, the MHPM should be operated in a vertical position. Both Shinyei sensors draw particulates in through the bottom in-take, and exhaust the particles out through the top.

Since the MHPM prototype is built with Bluetooth technology, it has the ability to communicate with a portable device, such as a smart phone, tablet, or laptop. Bluetooth wireless technology is based on the IEEE 802.15 standard, and, in general, is a low-cost communication scheme. Originally, it was developed to replace cables that were connected to desktop and portable computers, mobile phones, handheld devices, computer accessories, and peripheral electronic devices [11]. Using the MHPM prototype, three in-lab experiments were conducted using baby powder, cooking, and pillow tapping, as illustrated in Figure 7.

(a) Baby Powder Tests

(b) Cooking Tests

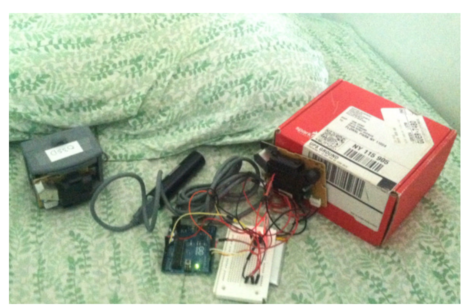

(c) Pillow Tapping testsTests

Figure 7. Tests of Baby Powder, Cooking, and Pillow Tapping

Based on the PM concentration data collected, line graphs were generated, as shown in Figure 8. Note that both the analog and digital outputs for the T2 provide similar results. The T2 detects higher concentrations of PM than the NS, as is expected, because the T2 detects particulates as small as 0.5 µm and larger; whereas the NS is limited to particulates 1.0 µm and larger. The PM difference in concentrations between the T2 and NS determines the particulate concentrations larger than 0.5 µm but less than 1.0 µm. The data from the three tests are tabulated in Table 3.

The results indicate that the baby powder test has more particulates greater in size than 0.5 µm, but less than 1.0 µm, than either cooking or pillow tapping. Based on the three tests, the greatest PM concentrations fall between 0.5 µm and 1.0 µm. All three test scenarios indicate a significant PM concentration between 0.5 µm and 1.0 µm, showing a distinct advantage of the T2 over the NS in determining air quality threats.

Conclusion

A Mobile Handheld Particulate monitor (MHPM) was described and tested, for monitoring particulate concentrations. Early detection of high PM concentration may reduce exposure to potentially harmful environments. A technology-enabled MHPM provides an affordable alternative resource that may allow consumers greater access to real-time PM conditions.

Table 3. Results of Tests for the Three Different Scenarios

	Concent. of PM	Temp. (F)	Relative Humid. (%)
Baby Powder (NS)	1085.71	75	52
Baby Powder (T2)	15724.04	75	52
(T2 – NS) for Baby Powder	14638.33	0	0
Cooking (NS)	4864.36	89	65
Cooking (T2)	16100.50	89	65
(T2 – NS) for Cooking	11236.14	0	0
Pillow Tapping (NS)	989.46	71	43
Pillow Tapping (T2)	6817.37	71	43
(T2 – NS) for Pillow Tapping	5827.91	0	0

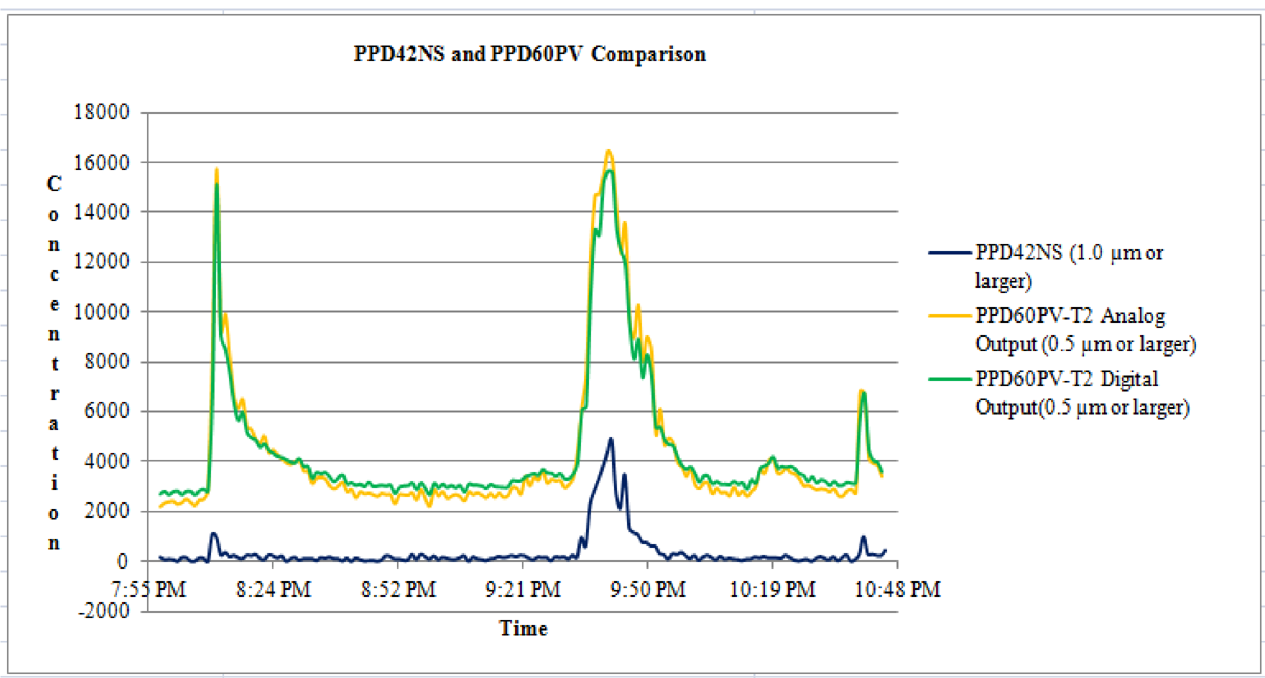

Figure 8. PPD42NS and PPD60PV-T2 Concentration Graphs

Acknowledgements

This research is partially supported by a grant from the New York Hall of Science (NYSCI), and by a grant from the HabitMap, Inc.

References

[1] U.S. EPA. 2013 *Basic Information on Particulate Matter*. (n.d.). Retrieved March 18, 2013, from http://www.epa.gov/airquality/particlepollution/index.htm

[2] Yarali, A., Claiborne, D., & Antony, S. (2011). Information Technology & Health: A New Arena in the Hospital Industry. *International Journal of Modern Engineering*, *12*(1), 56-63.

[3] Lin, C., Hsiung, S., Verma, A., & Crossman, G. (2004). Design and Analysis of an Air-Filter Sensor for a Residential Heating and Cooling. *International Journal of Modern Engineering*, *4*(2), 13-22.

[4] Shinyei Corporation of America. *Specification data sheet of PPD42NS*. (n.d.). Retrieved May 2, 2013 from http://www.sca-shinyei.com/pdf/PPD42NS.pd

[5] Shinyei Corporation of America. *Specification data sheet of PPD60PV-T2*. (n.d.). Retrieved May 2, 2013 from http://c1170156.r56.cf3.rackcdn.com/UK_SHN_PPD60PV_DS.pd

[6] Banzi, M. (2009). *Getting Started with Arduino*. (1st Ed.). Sebastopol, California: O'Reilly Media, Inc.

[7] Budde, M., Busse, M., & Beigl, M. (2012). Investigating the Use of Commodity Dust Sensors for the Embedded Measurement of Particulate Matter. *IEEE Xplore Digital Library,* pp. 1 – 4, June 2012 (ISBN: 978-1-4673-1784-9).

[8] Liu, T. (n.d.). *Digital-output Relative Humidity & Temperature Sensor / Module AM2303*. Retrieved March 30, 2013 from http://www.adafruit.com/datasheets/DHT22.pd

[9] Heng, I., Zhang, A., Heimbinder, M., & Obrok, P. (2012). Development of Low-cost Mobile Embedded AirCasting Handheld Device. *Technology Interface International Journal*, *13*(1), 14-20.

[10] McRoberts, M. (2010). *Beginning Arduino*. (1st ed.). New York City, New York: Apress.

[11] Heng, I, Zia, F., & Zhang, A. (2011). Wired and Wireless Port Communication. *In proceedings of The 118th Annual ASEE Conference & Exposition*, June 26 - 29, 2011. Vancouver, British Columbia, Canada.

Biographies

DR. IEM HENG earned his Bachelor's degree from Providence College (Providence, RI) with double majors in the Pre-Engineering Program and Mathematics. In addition, he earned a Bachelor's degree from Columbia University (New York, NY) in Mechanical Engineering, a Master's in Applied Mathematics from Western Michigan University (Kalamazoo, MI), and a Ph.D. in Computational and Applied Mathematics from Old Dominion University (Norfolk, VA). Before joining the Electrical and Computer Engineering Department at Manhattan College in the fall of 2013, he was a faculty member at NYC College of Technology (City Tech). Prior to City Tech, he was a faculty member and Chair of the CET department at DeVry College (Long Island City, NY). He worked as a researcher for NASA in Hampton, VA, for two years. In addition, he worked as a software developer for Predicate Logics for two years. His research activities include embedded systems, robotics, mechatronics, solar energy, software development for embedded systems with real time simulation, gaming and simulation programming, and web application programming.
He can be reached at iemheng@gmail.com

MR. RAYMOND YAP earned his Associate's degree in Applied Science in Electromechanical Engineering Technology in 2007, and his Bachelor of Technology degree in Computer Engineering Technology in 2010 from New York City College of Technology. Currently, he is enrolled as a graduate student at Manhattan College, majoring in Computer Engineering. His interest is in the design of electrical control systems, and the implementation of software programming in microcontrollers.

DISTRIBUTED POWER SMART GRID: A GAME THEORETIC APPROACH

Vincent Winstead, Minnesota State University, Mankato

Abstract

Since the advent of smart grid technology allows power availability and power transfer information at all points along the grid, for both generators and consumers, it is possible now for individual generators to affect overall energy flow. As a producer, each generator within the system has an independent interest in maximizing its gains. Conversely, each consumer within the system seeks to minimize its losses. Thus, the system can be modeled as a non-cooperative stochastic game. Gains and losses could be translated to dollars using current electrical kWh rates. This paper considers a construction of this type, where strategies for the players are developed to provide the best-expected payoff under conditions of both perfect and imperfect information.

Introduction

Currently, a number of hybrid electric vehicle options are available on the market for purchase [1]. These vehicles are expected to provide a bridge between internal combustion powered vehicles and potential future ultra-high efficiency, ultra-low (or zero) emission vehicles, such as those powered by electric cells or fuel cells. Recently, a number of passenger vehicle manufacturers have considered and/or made production plans for plug-in hybrid electric vehicles [2], [3]. Future consumer offerings are expected to expand in the short-term (1-5 years), with additional mid- and long-term expansion possible, as well [4].

A new paradigm of vehicle fueling will result from the development of this new technology, one that must provide options for alternative energy sources. For example, a plug-in hybrid electric vehicle can be charged from the grid and/or fueled by combustible fuels. Logically, the burden on the electrical grid due to plug-in hybrid electric vehicles could have an impact on energy delivery. If so, the capacity to provide electrical energy must be increased to compensate for additional plug-in hybrid electric vehicle usage [5]. An alternative, to mitigate stress on the grid, is to use smart grid technology and distributed generation to increase the efficiency of energy transfer between producers and consumers. Many states actively encourage alternative energy production through incentive programs [6], [7]. These programs may evolve in varying ways, but consumer-level distributed power generation, including solar electric and wind-based energy production, has emerged as a viable option. At the point of generation, energy production in excess of local, immediate needs allows producers to "sell" power, via the grid, to a regional energy provider.

The smart grid concept presupposes two things. One, information regarding electric energy usage (including flow rates and direction of flow) is expected to be measured and transferred to the responsible Independent System Operator (ISO) to improve overall energy availability, and to allow for appropriate planning [8], [9]. Two, the responsible ISO likely will take advantage of this information to adjust energy delivery costs based on supply and demand [10]. This implies that there may be an incentive for selling energy through the grid at certain times, and an incentive for purchasing energy at other times. This scenario provides consumers with several choices. Depending on the infrastructure's capabilities, an energy consumer might decide to charge a vehicle: when not in use, only when necessary (for battery protection, usage needs, etc.), according to a specific routine, or not at all (though the last is an unlikely choice). How does the consumer make those decisions?

This paper considers a future smart grid, wherein there are a significant number of plug-in electric and/or plug-in hybrid electric vehicles, and that consumers are allowed both to buy and/or to sell electric energy through the grid. Further, it is assumed that the responsible ISO collects grid usage information specific to this type of energy exchange, and dynamically adjusts the cost of electrical energy based on the number of producers and consumers. The paper considers this as a specific subset of activity on the electrical grid, independent of other activity, and models this interaction as a game between the responsible ISO and individual vehicles within the class of passenger vehicles.

A game theoretic methodology is proposed to determine the optimal decisions made by both players. This structure is inherently uncooperative among the vehicles in the class, because games are assumed to be played between individual vehicles and the responsible ISO. Also considered is the possibility that the same grid usage information is available to both the responsible ISO and the individual vehicles, and that it can be used to play cooperative games where the success of the entire class is preferred over the individual class member. Games of this type are analyzed, and optimal decisions for the players are derived.

Modeling

Game theory describes a framework for making decisions during an activity involving multiple entities, where each entity has its own goals that either may coincide with, or may contradict, the goals of the other entities. A zero-sum extensive game [11] has the following aspects:

- Player one has a set of strategies that can be employed in the game.
- Player two has a set of strategies that can be employed in the game.
- A utility is established for each combination of strategies chosen by the two players, which quantifies the gains for one player (usually denoted as player one), and the equivalent losses for the other player (usually player two).

The interaction of the class of electric/hybrid-electric vehicles is structured with the responsible ISO as a two-player zero-sum game in extensive form, where player one is the vehicle and player two the responsible ISO. The set of strategies for player one, the vehicle, is established with three elements:

1) Buy low-cost energy from the grid.
2) Sell high-cost energy to the grid.
3) Wait to play again later.

The third strategy allows player one to consider the current cost (per kWh) of energy, and to wait to see if the cost decreases. The risk is that energy cost may increase. The set of strategies for player two, the responsible ISO, includes three elements:

1) Raise the energy rate.
2) Lower the energy rate.
3) Keep the rate constant.

These strategies allow the responsible ISO to set rates based on current and/or expected future energy demand/ supply. Player one is assumed to always make the first "move". This extensive game is recursive, as well, since player one can postpone the buy or sell decision. This cannot develop into an infinite recursion, since player one (vehicle) connects to the grid with the intent of either buying or selling energy. Eventually, player one will choose the buy or sell strategy. This extensive game can be constructed in matrix form as the following nth game, G_n,

$$\begin{array}{c c} & \begin{array}{ccc} \textit{raise} & \textit{lower} & \textit{keep} \end{array} \\ \begin{array}{c} \textit{buy} \\ \textit{sell} \\ \textit{wait} \end{array} & \begin{pmatrix} u_{11} & u_{12} & u_{13} \\ u_{21} & u_{22} & u_{23} \\ u_{31} & u_{32} & u_{33} \end{pmatrix} \end{array} \tag{1}$$

where, $\cup \in R^{3x3}$ with elements u_{ij}, is the matrix of utility values gained by player one, given the strategy choices associated with row i and column j.

Game Matrix Utilities

The game matrix utilities nominally can be derived by considering the effect of adding one additional distributed generator (DG) of known capacity to the grid, i.e., by calculating its effect on the overall cost of distributed energy in the grid for the region containing the vehicle. This provides a *delta cost*. Determining an offset of this type can involve complex equations. For the purposes of this paper, it is assumed sufficient to merely determine relative costs. In other words, it is sufficient to establish whether the cost of distributed energy on the grid would change more with the addition of energy from this DG or with the additional load on the grid when a vehicle demands energy during charging. This relative cost offset also can reflect the likelihood that additional capacity will be necessary in the (near) future. A simplistic relative cost is considered, which can be scaled appropriately when more specific information is provided. In relative terms, the game favors player one if the responsible ISO adjusts energy costs down when player one is buying or when the responsible ISO adjusts energy costs up when player one is selling.

If the responsible ISO assumes only one electric/hybrid-electric vehicle exists, then the game matrix utilities are simple. The following matrix is proposed as a viable payoff matrix for the recursive game, G_n.

$$G_n = \begin{bmatrix} 1 & -1 & 0 \\ -1 & 1 & 0 \\ 0 & 0 & G_{n-1} \end{bmatrix} \tag{2}$$

Unit payoffs are utilized as normalized payoffs, since individual ISOs are expected to set energy costs differently. In addition, the game utility is assumed to represent the relative gains among the players, and presumes an inherent symmetry due to balancing between energy supply and demand. Here, player one is assumed to be as likely to buy as to sell in the future, and, therefore, the symmetric game favors neither player.

Since consumers have different vehicle usages, and since information connection decisions can be made based on different individuals' rationale, the vehicles are assumed to connect to the grid randomly. However, if the responsible ISO assumes n total electric/hybrid-electric vehicles connect to the grid daily (based on historical data), the game matrix utilities become stochastic; that is, they depend not only on the relative gains/losses that the players experience, but also on the expected number of energy buyers and sellers at the time each game is played, for which now there are n potentially recursive stochastic extensive form games being played between vehicles and the responsible ISO.

Additionally, individual consumer's electric energy usage patterns can be modeled. Aggregate usage patterns indicate the time segments during the day where energy usage is at a peak, and energy providers can utilize this type of information to schedule electric energy rates. However, in the smart grid concept proposed, the usage associated with individual members of the class becomes known to all grid-connected players at the point of connection. The games are played at random times, although it is assumed that an expected number of connections occur over periodic time segments. These times are modeled as random arrival times following a Poisson process [12].

For purposes of this paper, it is assumed that vehicles connect to the grid at least once per day to charge or discharge. This frequency is modeled as $f_c(T)$, where T is time in units of days. Generally, f_c is random, but assuming that an evaluation of prior history yields an average over all vehicles, the expected frequency is modeled as $\varepsilon\{f_c(T)\} = \alpha \bullet n$, where $\varepsilon\{f\}$ is the expected value of random function $f(\bullet)$, and α is the average number of connections to the grid per vehicle. When a vehicle connects to the grid, a notification is transmitted to the responsible ISO, and the arrival of this notification is a random process. Given a Poisson arrival process, the probability of m arrivals (i.e., connections of vehicles to the grid) over time interval $[0,T]$ is

$$\hat{p}(m,T) = \frac{(\lambda T)^m \cdot e^{-\lambda T}}{m!} \tag{3}$$

Given a time scale of one day, i.e., $T\equiv1$, then this process has a probability mass function of

$$p(x) = \hat{p}(x,1) = \begin{cases} \dfrac{e^{-\lambda}\cdot\lambda^x}{x!}; & x = 0,1,2,\ldots, \\ 0; & otherwise \end{cases} \tag{4}$$

with expected arrivals λ. The parameter $\lambda\equiv\alpha\bullet n$, and the probability of m vehicles connecting to the grid within the next day is $p(m)$.

It remains to connect this Poisson process concept to the utility modeling of the two-player game. First, the model assumes that, of the total number of connections to the grid each day, approximately half are for charging and half are for discharging. The responsible ISO is interested in the number of connections to the grid that are expected during the remainder of the day, since, if the majority of previously connected vehicles have chosen to charge, it is reasonable to expect that a greater percentage of the remaining vehicle connections will conduct a discharge. This will affect the probability of the matrix game utilities. As an example, if $\frac{\alpha\cdot n}{2}$ connections have already occurred, with all connections resulting in a discharge, then all expected remaining $\frac{\alpha\cdot n}{2}$ connections for the day will conduct charging, and the responsible ISO will be incentivized to increase per kWh energy rates.

Let $T_c \in [0,1]$ be the current time fraction of the day, and let l be the number of arrivals at time T_c, then $p(\alpha\bullet n - l, 1 - T_c)$ is the probability that the remaining expected total vehicle connections will occur by the end of the day. Now denote l_c as the number of total connections so far that day resulting in charging actions, and denote l as the total number of connections so far in the day. The responsible ISO is assumed to consider the connections to the grid from the previous second (in time). During that second, $\Delta l \geq 0$ connections have occurred, with $\Delta l_c \geq 0$ connections for charging, where $\Delta l_c \leq \Delta l$. A statistic of interest is the probability that the number of expected remaining requests for charging is greater than half of the total expected remaining requests. In other words, what is the probability that, of the expected remaining connections, at least half will request charging. This can be quantified as the following event probability,

$$\wp\left(\frac{\frac{\alpha\cdot n}{2} - (l_c + \Delta l_c)}{\alpha\cdot n - (l+\Delta l)} > 0.5\right) \tag{5}$$

where,

$\wp(X)$ is the probability of event X. This is significant, since the responsible ISO would prefer to raise energy rates if more than half the expected remaining customers that day will be making a purchase. The Poisson process model can be used to generate an equivalent probability,

$$\wp(\cdot) = \frac{\sum_{i=0}^{\alpha\cdot n-1}\sum_{j=0}^{i}\gamma_{ij}\cdot p(\Delta l = i, \Delta t)\cdot\wp(\Delta l_c = j|\Delta l)}{\sum_{i=0}^{\alpha\cdot n-1}\sum_{j=0}^{i} p(\Delta l = i, \Delta t)\cdot\wp(\Delta l_c = j|\Delta l)} \tag{6}$$

with $\Delta t = 1/(24\bullet60)$ days and

$$\gamma_{ij} = \begin{cases} 1; if\left(\dfrac{\frac{\alpha\cdot n}{2} - (l_c + j)}{\alpha\cdot n - (l+i)} > 0.5\right) \\ 0; otherwise \end{cases} \tag{7}$$

The probability measure $\wp(\Delta l_c = j|\Delta l)$ can be written as a joint probability distribution regarding vehicle connection events $y_1, y_2, \ldots y_{\Delta l}$, with sample set $\{buy, sell\}$ as

$$\wp(y_1 = buy, y_2 = buy, \ldots, y_{\Delta l_c} = buy, y_{\Delta l_c+1} = sell, \ldots, y_{\Delta l} = buy) \tag{8}$$

$$= \wp(y_1 = buy) \cdot \wp(y_2 = buy | y_1 = buy) \cdot \wp(y_3 = buy | y_1 = buy, y_2 = buy) \cdot \ldots$$

This is the same conditional probability found in the flipping of multiple "fair" coins, which can be computed using Pascal's Triangle of event probabilities [13]. Given that $\wp(\cdot) \in [0,1]$ is larger than some threshold, the responsible ISO would be incentivized to raise energy rates. This probability measure is used to generate a strategy for the responsible ISO, which could track the interaction between all vehicles and the grid, and to calculate $\wp(\cdot)$. That is, the "raise" strategy will be chosen with probability $\wp(\cdot)$, and the "lower" strategy will be chosen with probability $1 = \wp(\cdot)$. For the utility (game) matrix previously described, if optimal strategies for the players are desired, the following equations can be solved for game valuation V,

where,

$$V = q \bullet 1 + (1 - q) \bullet (-1) \tag{9}$$

$$V = q \bullet (-1) + (1 - q) \bullet (1) \tag{10}$$

and where the equations for V are derived using the method of equalizing strategies [11] and the fraction of games played using the "raise" pure strategy is q. Solving the equations for q essentially reveals that the strategy choice for player one is irrelevant. Here q=0.5 and V=0. That is, the optimal strategy favors neither player. If the probability measure $\wp(\cdot)$ is incorporated, the utility matrix is

$$\begin{bmatrix} \wp(\cdot) & -(1-\wp(\cdot)) & 0 \\ -(1-\wp(\cdot)) & \wp(\cdot) & 0 \\ 0 & 0 & G_{n-1} \end{bmatrix} \tag{11}$$

This remains a symmetric game (matrix), but it could have a different game valuation. Writing the equations for the matrix value V yields,

$$V = q \cdot \wp(\cdot) - (1-q) \cdot (1-\wp(\cdot)) \tag{12}$$

$$V = -q \cdot (1-\wp(\cdot)) + (1-q) \cdot \wp(\cdot) \tag{13}$$

where solving for V yields $V = \wp(\cdot) - \frac{1}{2}$. In fact, this new utility matrix guarantees that if player one (i.e., the vehicle) utilizes a strategy of equal buying and selling, and $\wp(\cdot) > 0.5$, then the player can expect a positive payoff. This would require that the majority of grid connections among all vehicles over the remainder of the day result in buying energy. This is clearly not a cooperative strategy among the vehicle players, since the gain of one vehicle is balanced by the loss of other vehicles. Further, if $\wp(\cdot) < 0.5$, then player one's optimal strategy is to "wait." Clearly, the availability of the $\wp(\cdot)$ information is important to maximize the payoff for player one.

Simulations

All simulations in this paper assume the number of players (vehicles) is 1000. Also, it is assumed that vehicles connect to the grid, on average, ten times per day, where each connection either leads to a "buy," a "sell," or a "wait." This does not require 10 physical connections, since the vehicle is assumed to be capable of activating/deactivating the connection without restriction. This results in 10,000 connections per day. The amount of energy transferred during each connection, in reality, would differ among the vehicles based on various factors, but this complexity is not included. For simplification, each energy exchange results in the transfer of one unit. Vehicles connect to the grid randomly, according to a Poisson arrival process at Δt=1/(24•60) (days) interval times. Figure 1 shows a sample generation of vehicle connection arrivals over a five-minute period.

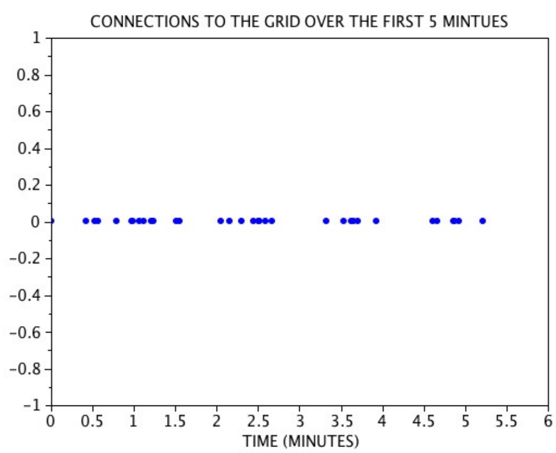

Figure 1. Example Distribution of Connections over the Span of Five Minutes

If the total connections within one individual minute are summed to yield a total for the minute, the connection events per minute can be utilized in the computation of $\wp(\cdot)$ at each minute. An example of the connection rate over a single day is shown in figure 2.

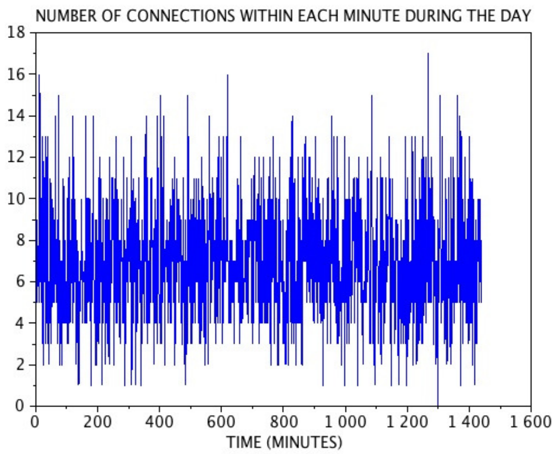

Figure 2. One Day of Simulated Connections with a Poisson Arrival Rate

The time interval for generating the simulation results is two hours. First, it is assumed that of all vehicles initiating grid connections, only one has access to the prior connections and requests. The other vehicles lack any information regarding prior connections in the day. The responsible ISO does have information concerning prior vehicle connections and expected connections over one day, but follows the strategy of raising and lowering the energy cost with equal probability at each minute. The vehicles that have no prior information on the calculation of $\wp(\cdot)$ utilize the strategy of buying and selling energy with equal probability. The first simulation result allows player one access to the computation of $\wp(\cdot)$. Player one plays the game ten times, i.e., makes ten random grid connections. The number of grid connections is allowed to be greater than ten if one or more connections result in $\wp(\cdot) \leq 0.5$. This means that one or more of the games played are recursive with zero payoff for G_1. Of the ten connections leading to buying and selling energy, half are associated with buying, but the distribution of buying events versus selling events is uniformly random among the ten connections. Figure 3 shows the changes in energy cost over the two-hour time period.

The energy costs are expected to remain close to the initial condition of \$0.1 per energy unit, since the responsible ISO chooses to raise or to lower rates with equal probability. The payoff for the ten games is \$5.25373. Assuming players buy and sell energy in equal amounts, numbers greater than zero indicate the player is ahead financially, on average, and numbers less than zero indicate the player is behind. Note that the expected payoff is zero, since the expected number of buying and selling events is the same. This positive payoff is a direct result of utilizing the "wait" strategy. As long as the "wait" strategy is not used too frequently, player one is expected to be able to effectively charge/discharge the vehicle as needed. The specific gains and losses depend on the current energy costs, and would vary depending on the time of day, and potentially from day to day. In this example, the vehicle payoff over the ten connections, assuming one unit of energy transfer per connection, is \$0.96. The overall result of gain and loss is telling, because it distinguishes the difference between strategies.

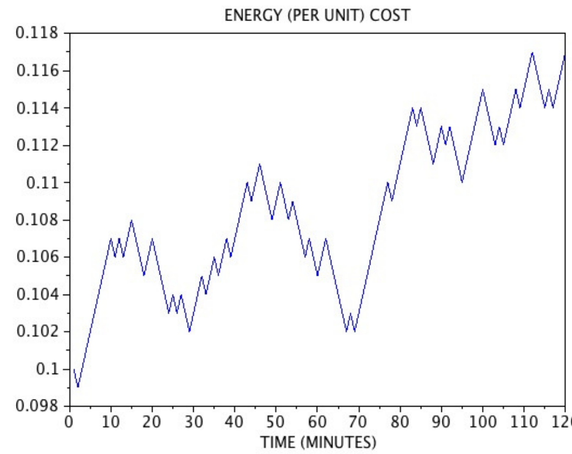

Figure 3. Energy per Unit Cost with Initial Condition \$0.1 per Energy Unit

In another simulation, the games are played using the same connection data, with player one connecting randomly ten times, but this time having no access to the $\wp(\cdot)$ computations. That is, player one does not utilize the "wait" strategy. In contrast, the payoff for these ten games is –0.07314. This result is not surprising, since given the symmetry of the game matrix, the expected payoff is zero. Of course, a "fair" coin flipped 100 times might yield 100 heads, even though the expected number of heads is 50. Over the period of days, it is likely that the average payoff would be approximately zero. This is the essence of the (weak) Law of Large Numbers [12].

Conclusions

Given a conservative model for the interaction of responsible ISOs and DGs capable of sourcing and sinking energy, it is assumed that a "fair" game will exist and be played between these players. The smart grid is expected to provide an extensive capability for information transfer to the potential benefit of the players. Results indicate that, given this level of information, players have the opportunity to improve their game payoffs.

List of Symbols and Abbreviations

$\varepsilon\{\cdot\}$	Expectation function
$\wp(X)$	Probability of event X
$\hat{p}(\cdot)$	Poisson arrival probability measure
$p(\cdot)$	Probability mass function
α	Average number of connections to the grid per vehicle
λ	Total number of expected arrivals (grid connections)
n	Total number of electric/hybrid-electric vehicles
Δl	Number of arrivals (grid connections) in one second
Δl_c	Number of charging events in one second
Δt	Delta time period
ISO	Independent System Operator
DG	Distributed Generator

References

[1] Yildiz, F., & Baltaci, K. (2011). Challenges of EVs and HVs to the U.S. Electrical Power Grid, *International Journal of Engineering Research and Innovation*, *3*(1), 68-74.

[2] Prius Plug-In Hybrid 2013. Retrieved September 18, 2013 from http://www.toyota.com/prius-plug-in/#!/Welcom

[3] Ford Escape Plug-In Hybrid. Retrieved September 18, 2013 from http://www.plugincars.com/ford-escape-plug-hybri

[4] Guilford, D. (March 25, 2013). Market Remains Tepid, But Many New EVs Are on the Way, *Automotive News* Article. Retrieved from http://www.autonews.co

[5] Ofori-Boadu, A., Shofoluwe, M., & Yeboah, F. (2013). An Assessment of the Predictors of U.S. Commercial Electricity Consumption, *International Journal of Engineering Research and Innovation*, *5*(1), 76-89.

[6] Bhattacharjee, S., Emmons, N., Mahfouz, T., & Jones, J. (2012). Comparative Analysis of the Residential Energy Efficiency Policies of Six Midwestern States of the U.S., *International Journal of Engineering Research and Innovation*, *4*(2), 38-45.

[7] Energy Incentive Programs. Retrieved September 18, 2013 from http://www1.eere.energy.gov/femp/financing/energyincentiveprograms.htm

[8] Massoud Amin, S., & Wollenberg, B. F. (2005). Toward a Smart Grid: Power Delivery for the 21st Century, *Power and Energy Magazine, IEEE, 3*(5), 34-41.

[9] Metke, A. R., & Ekl, R. L. (2010). Security Technology for Smart Grid Networks, *IEEE Transactions on Smart Grid, 1*(1), 99-107.

[10] Doner, J. (July 2012). MISO Transmission Cost Allocation Overview, Midwest ISO Presentation.

[11] Fudenberg, D., & Tirole, J. (1991). *Game Theory*, MIT Press.

[12] Grinstead, C., & Snell, J. (1997). *Introduction to Probability*, American Mathematical Society.

[13] Hazewinkel, M. (2001). *Encyclopedia of Mathematics*, Springer.

Biography

VINCENT WINSTEAD is an Associate Professor of Electrical and Computer Engineering and Technology at Minnesota State University, Mankato. He earned his B.S. degree in Electrical and Computer Engineering from Marquette University, WI; M.S.E.E (Electrical Engineering, 1994) from the University of Minnesota, Minneapolis, MN; and Ph.D. (Electrical Engineering, 2005) from the University of Wisconsin, Madison, WI. Dr. Winstead is currently teaching courses in power systems and embedded systems. His interests are in optimization, automotive powertrain controls, and autonomous robotics. Dr. Winstead may be reached at vincent.winstead@mnsu.edu.

A NOVEL DUAL-MODE GATEWAY FOR WIRELESS SENSOR NETWORKS AND LTE-A NETWORK CONVERGENCE

Garth V. Crosby, Southern Illinois University Carbondale; Farzam Vafa, Southern Illinois University Carbondale

Abstract

In recent years, the number of machine-to-machine (M2M) networks, which do not require direct human intervention, has been increasing at a rapid pace. Meanwhile, the need for a wireless platform to control and monitor these M2M networks, one with both a vast coverage area and a low network deployment cost, continues to be unmet. Mobile cellular networks (MCNs) and wireless sensor networks (WSNs) are emerging as two heterogeneous networks that can meet the challenges of M2M communication through network convergence. In this paper, a model for network convergence between a Long Term Evolution-Advance (LTE-A) cellular network and a WSN is proposed. Quality-of-Service (QoS) issues are assessed by a comparative study of the network delay in tight coupling and loose coupling LTE-A configurations. Simulation results indicate that the network delay in this proposed converged network is acceptable for various M2M applications. Additionally, it is demonstrated through simulation that the energy consumed by the implementation of the proposed protocol is suitable for resource-constrained devices.

Introduction

The authors envision a future where millions of small sensors, actuators, and other devices form self-organizing wireless networks. This vision relies heavily on the emerging *Internet of Things* paradigm, where millions of embedded systems (machines) are able to communicate with, and control, each other without human intervention. These machines should merge seamlessly into people's daily lives resulting in an enhancement of humans' well-being. Various aspects of people's lives will be affected. Major areas of impact will include:

- Healthcare: wireless body area networks will collect health data, for example, vital sign readings, and transmit this to healthcare providers. Healthcare provider computers will process the data and automatically request an ambulance to be sent to a patient's address, as needed.
- Emergency response: wireless sensor networks will collect data about the status of buildings, bridges, and highways. Emergency personnel will be notified if the data collected indicates a potential bridge collapse, a highway collision, etc.
- Supply chain and inventory management: raw material can be tracked from source to retail market in an automated manner. Sensors can determine when raw material is low, and communicate to other machines to initiate the supply chain for restocking, with little, to no, human intervention.

Currently, there is no universal platform that facilitates smooth end-to-end M2M communication via a widely accessible network. This paper attempts to fill this need by proposing a dual-mode gateway for WSN and LTE-A network convergence. The concept of a dual-mode gateway is not novel, and has been proposed in several works [1], [2]. However, a new dual-mode gateway for end-to-end communication between WSN and LTE-A cellular networks is proposed in this paper. The proposed model provides a wireless platform for the convergence of wireless sensor networks and LTE-A cellular networks, which can provide a cost effective and pragmatic solution for M2M communication.

This paper's main contributions are:

i) Exploring the challenges of developing a broad coverage, low cost solution for M2M networks.

ii) Proposing a novel dual gateway interface for WSNs and LTE-A networks.

iii) Demonstrating the feasibility of the proposed dual mode gateway.

Related Work

4G technology was meant to provide what is known as "ultra-broadband" access for mobile devices. LTE advanced was submitted as a candidate for the 4G system to the International Telecommunication Union- Telecommunication Standardization Sector (ITU-T) in 2009. It was approved into International Mobile Telecommunications (IMT) Advanced, and was finalized by the 3rd Generation Partnership Project (3GPP) as a major enhancement of the Long Term Evolution (LTE) standard in March, 2011[3].

Lee et al. [4] discuss the current state of standardization efforts in M2M communication and provide an overview of the network architecture and features of M2M communications in 3GPP, and identify potential issues including physical layer transmissions, the random access procedure, and radio resources allocation. They also proposed a solution to provide QoS guarantees to facilitate M2M applications with hard timing constraints. Attwood et al. [6] proposed a mobility architecture, IoMANETS, for wireless M2M networks. The design provides a fault tolerant solution to the mobility issue by allowing mobile nodes to seamlessly connect to M2M-Internet of Things infrastructure. The assumptions are that fixed nodes are connected to the internet with either IPv4 or IPv6, and that the mobile nodes have IEEE 802.15.4 adapters operating a 6LowPAN IP stack. IoMANETs facilitates the reachability of the device using indirections based on the original global address. The approach proposed in this paper does not focus on fault tolerant connectivity of mobile nodes, but rather on QoS issues in connecting WSN to 4G devices.

The work most similar to the one presented in this paper was proposed by Zhang et al. [2], who examined network convergence between mobile cellular networks and wireless sensor networks. They proposed that the mobile terminals in MCN act as both sensor nodes and gateways for WSN in the converged networks. Comparatively, a separate device to serve as a dual mode gateway and protocol converter (adapter) is proposed in this paper. Additionally, LTE-A is specifically addressed, while Zhang et al. [2] did not specify the cellular technology involved, and they do not guarantee end-to-end connectivity as is done in the proposed converged network. They did, however, provide a useful framework, the current research proposes specific mechanisms, with current technologies, that can be pragmatically implemented and tested.

Igarashi et al. [7] proposed node and network models for achieving internet protocol (IP) based direct communication in M2M networks. Their proposal makes several assumptions, yet it cannot be implemented in its current form. The protocol proposed in the current work makes use of the current state of art WSN technology and LTE-A to implement what is believed to be a feasible end-to-end connection between wireless sensor nodes and LTE-A devices.

LTE Network Architecture

One of the major goals in 4G systems is to provide convergence between all IP-based networks. The appropriate platform for this purpose should integrate network management, security, and QoS. LTE-A satisfies most of the requirements for being a primary platform as a converged networks enabler. It is backward compatible with previous versions of 3GPP standards, non 3GPP networks, and most of the important IP-based networks, such as the Internet. Considering the technical features of the LTE network, elaborated on later in this section, and the potential capabilities of network convergence that LTE-A possesses, it is the authors' belief that LTE-A will play a major role in the future of M2M communication. Although other 4G technologies, such as 802.16m, may be an alternative, the vast majority of subscribers use LTE for wireless communication. As such, there would be little cost for additional deployment, thus making LTE a logical choice.

The LTE system architecture is all IP-based, and, therefore, is designed to support packet-based transmission. A simplified illustration of the LTE system architecture is shown in Figure 1.

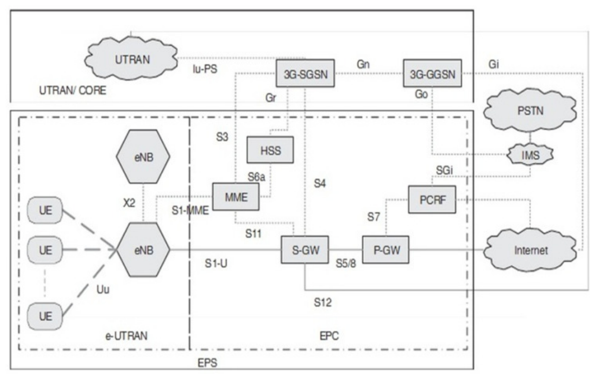

Figure 1. Simplified LTE System Architecture [8]

The two main blocks of the LTE system architecture are the Evolved Universal Terrestrial Radio Access Network (E -UTRAN) and the Evolved Packet Core (EPC). The E-UTRAN is responsible for managing radio access, and provides User Plane (U-Plane) and Control Plane (C-Plane) support to the User Equipment (UE). The U-Plane handles a group of protocols used to support end user data transmission through the network, while the control plane contains a group of protocols for managing the connection between the UE and the networks, and for controlling the user data transmissions. Some of the connection-management functions include handover, service establishment, resource control, etc. The E-UTRAN consists of only the evolved Node Base stations (eNodeBs) or eNBs, where eNB is the LTE terminology for a base station. The EPC is a mobile core network, and its main responsibilities include policy management, security, and mobility management. The EPC consists of the Mobility Management Entity (MME), the Serving Gateway (S-GW), and the Packet Data Network Gateway (P -GW).

M2M Networks

M2M is the concept of connecting machines for enabling the exchange of data. The major goal of the M2M network is both the interconnection of the individual machine nodes and the handling of data transport between the nodes. Regardless of the type of device or data, information typically flows through the network in the same general way: it is gathered from a machine over a link, and received by a controlling system where it can be processed and acted upon.

M2M communication typically is used on four network platforms: smart grids, building automation, healthcare, and automotive. The smart grid is an integration of a power network and an information network, designed to improve the efficiency of power transmission, to enhance the quality of service, and to reduce economic and environmental costs [9]. The primary purpose of home networking is media distribution. However, it can include elements of the smart grid network as described previously. Media distribution systems consist of media storage (media server), media transportation (Wi-Fi, Bluetooth), and media consumption (laptops, smart phones, tablets) [10].

Healthcare M2M networks are used to monitor health conditions, and inform monitored patients, as well as their doctors, of any abnormal conditions that may occur. In some cases, in order to measure health parameters, such as blood pressure, cholesterol, blood sugar level, etc., miniature sensors are implanted inside the human body to form a wireless body area network (BAN). Body sensors are all connected to an on-person gateway, such as a cell phone, which also acts as the collector for all sensor data. Sensors forward data to the cell phone, which in-turn sends it over the cellular network to health monitoring servers.

In recent years, research has been conducted on M2M communications support for vehicular networks. In an automotive application, an M2M network is utilized as a controlling part of the vehicle, known as a controller area network (CAN). In this application, M2M communications are divided into four different categories: traffic management, vehicle telematics, safety & collision avoidance, and entertainment [11].

There are two main restrictions in M2M communications: power consumption and computational capability. In most of the M2M networks, machine type nodes do not have access to a permanent energy source. A battery is the most common power source for a machine type node. Therefore, long distance wireless communication is not practical in M2M communication, since the high power transmission energy needs cannot be supplied with a miniature battery. Also, depending on the application, the computing capability of the sensor nodes may be extremely limited. For example, an implantable body sensor node has very limited memory and processing capability.

M2M and LTE-A Network Convergence

As the demand for M2M is increasing rapidly, M2M communication has become one of the focus areas of the LTE-A project. Within the next several years, M2M communications are expected to exceed the number of H2H (human-to-human) communications. Among other causes, one driver for the replacement of H2Hs by M2M communication is that there are almost 50 billion machines in the world, in comparison to 6 billion people.

In this research, other alternatives, including GPRS/UMTS, were considered. Indeed, there are some applications in GPRS/UMTS networks for the express purposes of metering and security alarm systems that are based on cellular M2M networks [12]. However, in general, current solutions that are based on general packet radio service (GPRS), have been proven to be inadequate for supporting the M2M system. On the other hand, LTE-A, with its higher data rate and larger network capacity, is able to cater efficiently to M2M communications.

The Proposed Dual Gateway Model

In this paper, a tight coupling, dual mode gateway is proposed. Employing a dual mode gateway, for the merging of two networks, enabled the use of specific features and protocols for each individual network. The WSN network employed the IEEE 802.15.4 standard and 6LoWPAN protocol stack, which enabled all the nodes to have distinct addresses. Therefore, the nodes could be addressed individually using the IPv6 protocol. This also facilitated power efficient connections among the resource-constrained nodes in the WSN. The WSN network was connected to the LTE-A network via the dual mode gateway, so that all of the nodes could be controlled and monitored by the LTE system via the gateway.

Merging Network Techniques

There are two major techniques for multiple network integration: loose coupling and tight coupling. In the loose coupling method of inter-networking, networks are interconnected to each other independently. For instance, the first network is connected to the IP network to obtain an indirect link with the second network. Figure 2 depicts the topology of the loose coupling method. In the tight coupling inter-networking method, the first network is connected directly to the second network. In such an inter-networking scenario, the first network's gateway is connected directly to the access layer of the second network. For the LTE-A/WSN model specifically, the WSN gateway can be merged to the UE (User Equipment), resulting in the creation of a dual mode radio. This method is quite efficient in terms of end-to-end latency. However, to the best of the authors' knowledge, prior to this work no dual mode gateway had been designed for LTE-A/WSN convergence. Hence, this dual mode gateway using tight coupling to connect LTE-A cellular and WSNs is proposed. The topology of the tight coupling, dual mode gateway is shown in Figure 3.

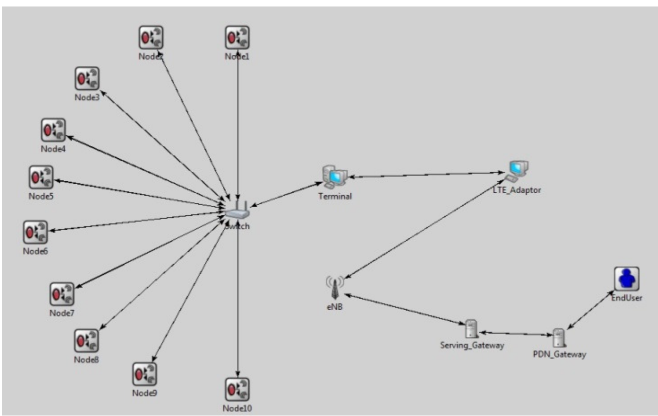

Figure 2. Loose Coupling Topology

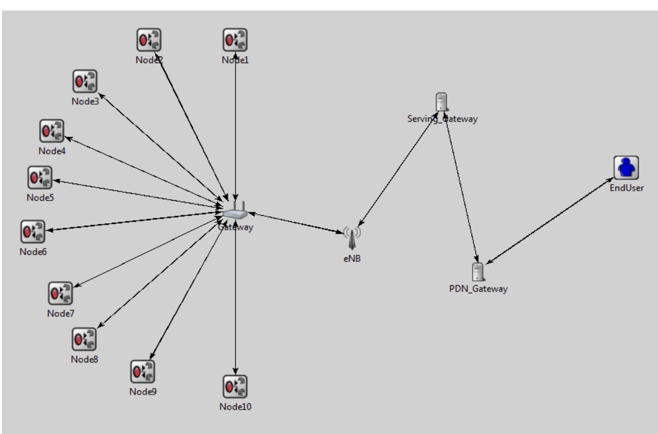

Figure 3. Tight Coupling Method with Dual-Mode Gateway

Protocol Conversion

The main effort of this research work was to establish bidirectional communication between the WSN and LTE-A devices. The protocol stacks of 6LoWPAN and the User Equipment (UE), which is the last node in the access layer of E-UTRAN, are not the same. Therefore, protocol conversion needs to occur in the gateway to make the receiving packets (packets coming from the WSN) compatible with the LTE-A network, and vice versa. The protocol stacks of 6LoWPAN and UE are shown in Figure 4.

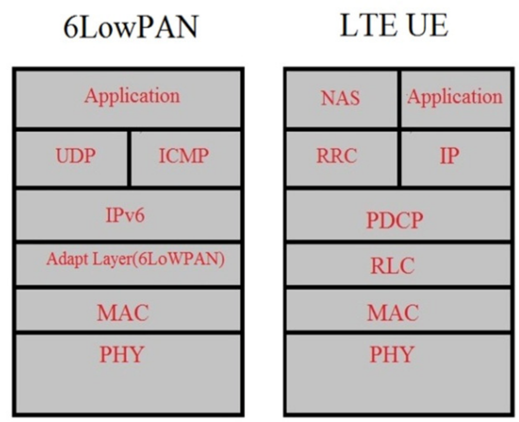

Figure 4. 6LoWPAN and LTE UE Protocol Stack

6LoWPAN technology has defined encapsulation and header compression mechanisms, which allow IPv6 packets to be sent and received over low-power wireless networks, specifically those using the IEEE 802.15.4 standard. The specification developed by the 6LoWPAN IETF group is RFC 4944, and the problem statement document is RFC 4919. IPv6 expands the IP address space from 32 to 128 bits. Also, IPv6 increases the Maximum Transmission Unit (MTU) from 576 to 1,280 bytes. In the IEEE 802.15.4's standard, the maximum packet size is 127 bytes, which perfectly fits in the IPv6 packet. The frame structure of 6LoWPAN is shown in Figure 5.

In addition to the increase in address space that IPv6 has in comparison to IPv4, and the ongoing depletion of available IPv4 addresses, there are several other reasons to prefer IPv6 implementations for resource-constrained devices. First, IPv6 reduces the size of routing tables, and makes routing more efficient and hierarchical. Second, in IPv6 networks, fragmentation is handled by the source device, rather than the router, using a protocol for the discovery of the path's maximum transmission unit (MTU). This technique increases the data transmission speed [13]. Third, in IPv6 the packet header is simplified, which makes packet processing more efficient. Compared with IPv4, IPv6 has no IP level checksum, so the checksum does not need to be recalculated at every hop. This results in comparatively reduced end-to-end latency in multi-hop networks.

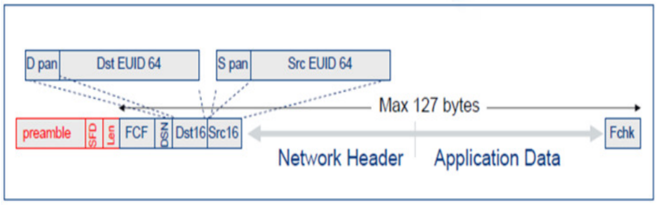

Figure 5. Frame Structure of 6LoWPAN [14]

Internet Protocols are used widely in different wired and wireless networks. Any two heterogeneous networks, regardless of the function, size, or topology, can have connection to each other through Internet protocols. WSNs employing 6LoWPAN over the IEEE 802.15.4 standard, have enabled connectivity to other networks (and the Internet) using IP routing protocols. Due to the restrictions on memory size, power consumption, and computing capability of WSNs, some type of data compression may be necessary. The distinct features of 6LoWPAN make it particularly suitable for use in IP-based M2M networks.

For the remainder of this section, the details of the protocol conversion mechanisms that are executed in the proposed dual mode gateway will be explained. First, consider data packets traveling from the WSN to the LTE-A network. Figure 6 illustrates the protocol conversion of incoming packets (outgoing from the WSN) to the LTE-A network. Since the connection is IP based, there is no need to reach the layers above the IP layer. IP tunnel encapsulation, which is illustrated in Figure 7, is employed to convert the IPv6 to IPv4 in the gateway. This is done in order to ensure the establishment of end-to-end connectivity, since IPv4 is compatible with all of the existing networks. The MAC layer of LTE UE consists of MAC header and RLC payload. The MAC header size is 42 bytes, and the RLC payload is 400 bytes. The maximum size of the packets coming from the WSN is 127 bytes, plus 20 additional bytes for the IPv4 header, which is added in the IP tunneling procedure. This makes the total maximum packet length 147 bytes. As such, the packet coming from the WSN network fits into the LTE MAC layer payload. As can be seen in Figure 1, in the user plane of the LTE network, the received packet from the UE is passed to the eNb. The LTE network's compatibility facilitated the transfer of the incoming packet from the WSN network to other IP-based networks. EUTRAN enabled the exchange of data through the SGW (Serving Gateway) and PGW (PDN Gateway), between the dual mode gateway and the IP-based network.

Second, consider data traveling in the reverse direction, that is, from the LTE-A network to the WSN. The packet frame structure is depicted in Figure 8. Here it is shown that there are three headers, namely the LTE, IPv4, and IPv6 headers. However, the LTE and IPv4 headers are not recognizable by the WSN. Therefore, the packet would be discarded by the WSN if it were delivered in this format. To deal with this issue, the LTE and IPv4 headers are discarded at the dual mode gateway. Both the LTE and IPv4 headers have constant size (42 bytes for LTE and 20 bytes for IPv4), and are easily recognized by the dual mode gateway. The dual mode gateway simple strips 62 bytes off the packets coming from the LTE-A network. The resulting packet frame is shown in Figure 9.

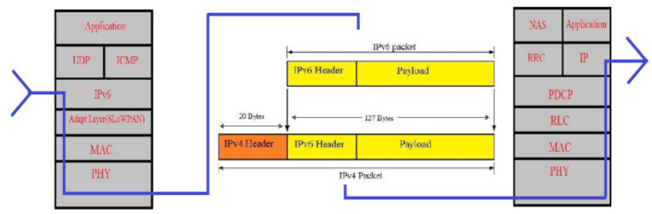

Figure 6. Protocol Conversion of Packets Traveling from WSN to LTE-A Network

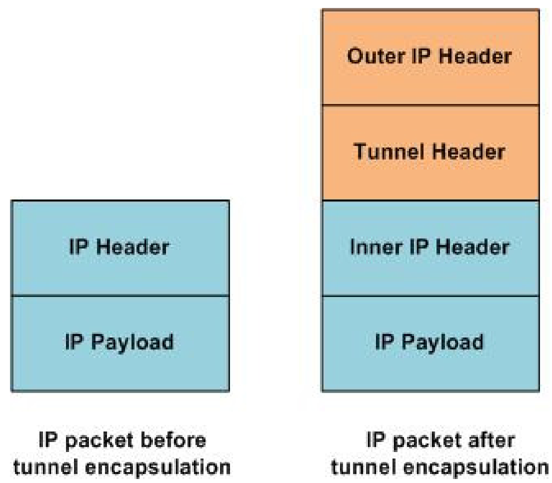

Figure 7. IP Tunneling

Figure 8. LTE-A Packet Frame

Figure 9. LTE-A Packet Frame after Protocol Conversion

In the interest of clarity, a high level, step-by-step description of the dual mode gateway operation is now provided. First, consider the packets traveling from the WSN to an LTE-A end-user. The sequence of events/processes is:

1. A wireless sensor node generates a packet containing the source IPv6 address, the destination IPv6 address, and the payload;
2. The incoming packet arrives at a port on the IPv6 side of the dual mode gateway;
3. The dual mode gateway adds an IPv4 header to the packet;
4. The dual mode gateway sets the IPv4 source and destination addresses;
5. The dual mode gateway adds the LTE header to the packet;
6. The packet is forwarded to the LTE-A cellular network.

Second, consider packets traveling in the reverse direction, that is, from the LTE-A end-user to a wireless sensor node. The steps are as follows:

1. The end user creates a packet containing IPv4 source and destination addresses, an IPv6 destination address, and the payload;
2. The dual mode gateway receives the packet from the IPv4 side interface;
3. The dual mode gateway extracts the LTE and IPV4 header;
4. The dual mode gateway identifies the destination IPv6 address from the IPv6 header;
5. The dual mode gateway sends the packet to the destination node.

Implementing the Dual Gateway Model

In this section, implementation details of the simulation model are presented. First, it provides a step-by-step description of how the M2M to end user connection is established. Second, the establishment of the end-user to M2M (in this case WSN) connection is explained.

<u>The M2M to End User Connection</u>:

i. An M2M node generates a packet;
   The packet includes the following information:
   SrcIPv6
   DstIPv6
   Payload
ii. The incoming packet arrives at a port on the IPv6 side of the dual mode gateway;
   Connection in OMNET++ is made with the following command
   Server.Out[0] -> Client.In [1]
iii. The dual mode gateway adds an IPv4 header to the packet;
   The header is encapsulated using inheritance (a feature of object-oriented programming).
iv. The dual mode gateway sets the IPv4 source and destination addresses;
   The dual mode gateway sets the IPv4 source and IPv4 destination addresses with the following commands:
   pkt->setSrcIPv4();
   pkt->setDstIPv4();
v. The dual mode gateway adds the LTE header to the packet.
   The header is encapsulated via inheritance.

<u>The End User to M2M Connection</u>:

i. The end user creates a packet containing IPv4 source and destination addresses, IPv6 destination address, and payload;
   The following commands are used:
   PKT-> SETSRCIPV4();
   PKT-> SETDSTIPV4();
   PKT-> SETSRCIPV6();
   PKT-> PSETDSTIPV6();
   PKT-> SETPAYLOAD();
ii. The dual mode gateway receives the packet from the IPv4 side interface;
iii. The dual mode gateway extracts the LTE and IPV4 headers;
iv. The dual mode gateway identifies the destination IPv6 address from the IPv6 header;

Modeling Energy Consumption

The proposed solution is feasible in real networks if it can be implemented efficiently on resource constrained M2M nodes, which in this case are wireless sensors. To assess the energy demands of this technique, a scenario is considered in which each wireless sensor node is powered by two AA batteries. This is a popular source of power for commercially available wireless sensor nodes. The length of the 6LoWPAN packet varies between 74 and 127 bytes, depending on the size of the payload. The amount of energy consumed during packet transfer was determined by evaluating the reduction in battery voltage using Equation (1):

$$V_{Battery} = V_{Initial} - \frac{E\left(\frac{J}{B}\right) * Bits(bit)}{C(mAh)} \tag{1}$$

where E is the energy consumption of the node per bit, and C is the capacity of the AA battery. In accordance with

Aslam et al. [15], it is assumed that the value of E was 50 nJ. The capacity of the AA battery typically varies between 400-3000 mAh, depending on battery characteristics. For this research, a value of C=500 mAh was chosen. This was an arbitrary value selected from the typical range.

Results and Discussion

Two sets of simulation studies were conducted. For the first set of simulations OMNET++ was utilized. The main issues investigated were: (i) the reliability of the connections, and (ii) the end-to-end delay in the proposed converged network. The approach consisted of a comparative study of both loose coupling and tight coupling. The network setups for loose coupling and tight coupling are shown in Figures 2 and 3, respectively. In the second set of simulations, analytical estimates of power consumption in wireless sensor networks were used. Additionally, MATLAB was utilized to demonstrate the rate of energy consumption.

Evaluating Reliability and End-to-End Delay

In the simulation, a dual mode gateway that separates the heterogeneous WSN and LTE-A cellular networks was modeled. For simplicity, only 10 nodes were deployed in the WSN. Network size was limited because the main consideration was the establishment and feasibility of end-to-end connections. The reliability of the converged network was limited by the low power, lossy channel of the WSN. IEEE 802.5.4 and 6LoWPAN are among the best options for the low power, lossy network, and both were utilized in these simulations. The researchers were cognizant of potential bottlenecks at the dual mode gateway. This, however, was an issue of scalability, and could easily be addressed by providing multiple gateways. Nonetheless, issues of scalability were not the focus of this research, and, therefore, were not addressed in the simulations. The delay at the dual mode gateway, as a result of buffering and protocol conversion processing, was negligible with respect to the delay caused by the noisy channel of the WSN, and was not taken into account.

The simulation parameters were: end-to-end delay and number of transmitted packets. The bit error rate, the result of collision, was not included, since the main focus was to ensure that the connection was established, rather than to evaluate the noisiness of the channel. The objective was to achieve successful protocol conversion, which is indicated by the ability of packets to travel between the M2M and LTE-A networks.

Figures 10 and 11 depict the end-to-end transmission delay time in loose coupling and tight coupling, respectively. The graphs imply that by using the proposed tight coupling method, the end-to-end delay time can be decreased significantly, from a maximum of 900 milliseconds to 500 milliseconds, which would be a significant enhancement for real time networks or systems with low latency restrictions. Also, this would meet the requirements for various applications of real-time M2M networks [16].

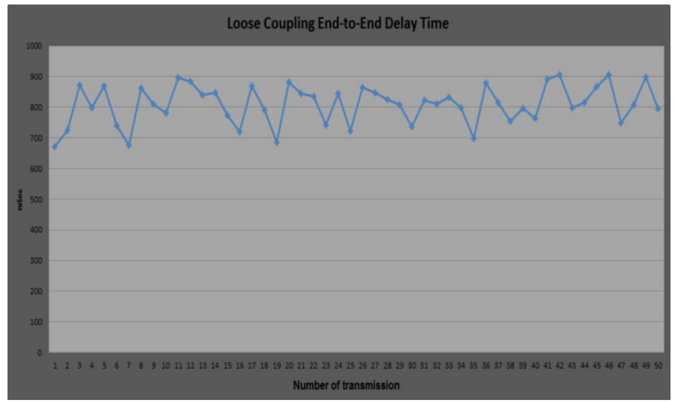

Figure 10. Loose Coupling End-to-End Transmission Delay Times

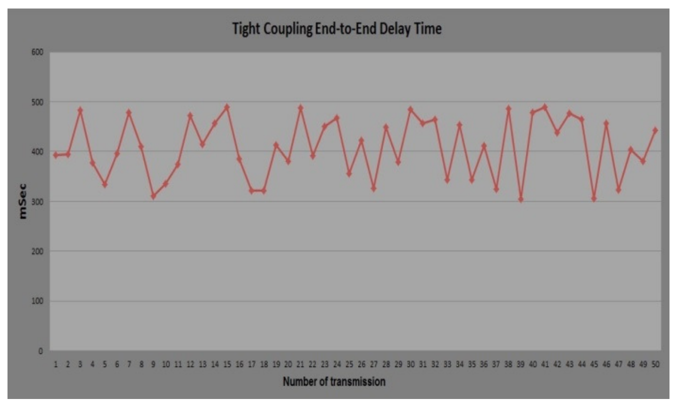

Figure 11. Tight Coupling End-to-End Transmission Delay Times

Evaluation of Power Consumption

Evaluation of power consumption for the protocol was achieved by using MATLAB simulations based on Equation (1). The WSN was configured primarily as a monitoring network, with sensors gathering and sending data via the dual mode gateway to LTE-A devices. The data rate was set at 250kps, as used in the IEEE 802.15.4 standard. A screen capture of the MATLAB simulation is shown in Figure 12. The simulation parameters are: battery voltage, battery threshold voltage, battery capacity, energy consumption, reception rate, and critical interval, which are user defined. In addition, the packet length was included, and its value is consistent with real networks. The MATLAB Graphical User Interface (GUI) simulator that was developed and utilized is shown in Figure 12.

Figure 12. Wireless Sensor Node's Battery Lifetime

Figure 13 implies that the node's operational lifetime is approximately 159 days. One solution to extend the short operational lifetime of the node is to reduce data throughput, and, thus, power consumption, by adding an interval time, for each transmission between the dual mode gateway and the nodes, once a critical battery voltage threshold is reached. The critical voltage threshold was set to 2.6 volts, while a node was considered dead if its battery voltage fell to 2.4 volts. In this scenario, after reaching the threshold voltage, a control packet, 'low life', is sent from the wireless sensor node to the dual mode gateway, indicating that the node's battery life is low. Upon receiving the 'low life' packet, the dual mode gateway adds an interval time between each transmission in order to extend the lifetime of the node's battery. This effectively lowers the data transmission rate of that particular sensor node. Also, it should be noted that, in this scenario, the interval time can be set by the LTE-A device (or end user). In this case, the interval time was set at 1000 milliseconds. Figure 14 shows that after inserting the proposed interval time in the transmission protocol, the node's lifetime was extended to 252 days.

Conclusion and Future Work

In this paper, a model for the convergence of WSN and LTE-A networks was proposed. In the model, a dual mode gateway facilitated end-to-end connection for M2M communication with access to a wide coverage network. The simulation results indicated that this is a viable option that meets the delay and power consumption requirements of various types of M2M applications. For future work, a comprehensive test-bed evaluation of this research project is recommended. Additionally, creating an end-to-end security solution is worth investigation.

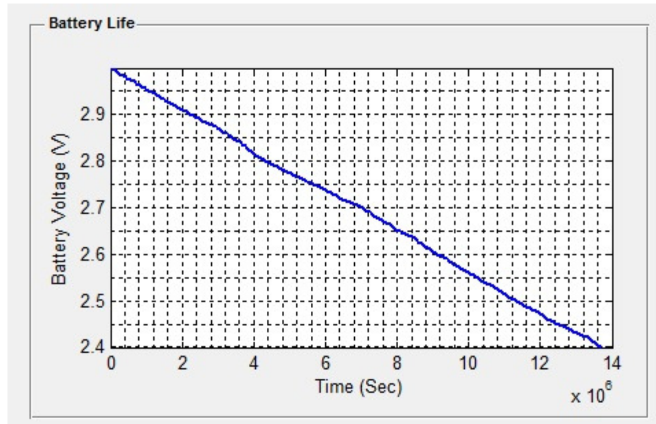

Figure 13. Wireless Sensor Node's Battery Lifetime

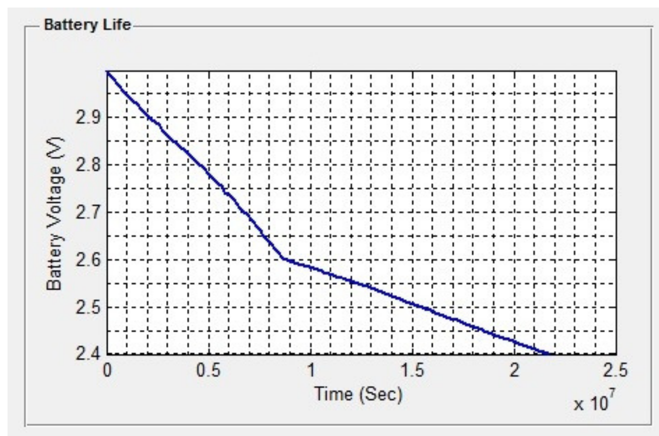

Figure 14. WSN Battery Lifetime after Employing Interval Time

References

[1] Liu, Y., Zhen, B., Xu, Y., Yang, H., & Zhao, B. (October 19-20, 2010). Current and Future Trends in Hybrid Cellular and Sensor Networks. Paper presented at the European Telecommunications Standards Institute (ETSI) M2M Workshop, Sophia Antipolos, France.

[2] Zhang, J., Shan, L., Hu, H., & Yang, Y. (March, 2012). Mobile Cellular Networks and Wireless Sensor Networks: Towards Convergence. *IEEE Communications Magazine*,50 (3), 164-169.

[3] International Telecommunication Union. (2011). ITU's History.

[4] Lee, D., Chung, J., & Garcia, R. (2012). Machine to Machine Communication Standardization Trends and End to End Service Enhancements through Vertical Handover Technology. *Proceedings of the IEEE, International Midwest Symposium on Circuits and Systems (MWSCAS)*, (pp. 840-844). Boise, Idaho.

[5] Lien, S., & Chen, K. (April, 2011). Toward Ubiquitous Massive Accesses in 3GPP Machine-to-Machine Communications. *IEEE Communications Magazine*, *49*(4), 66-74.

[6] Attwood, A., Merabti, & Abuelmaatti, O. (2011). IoMANETS: Mobility Architecture for Wireless M2M Networks. *Proceedings of the IEEE, GlobeCom Workshop, the International Workshop on Machine-to-Machine Communications*, (pp. 399-404). Houston, Texas.

[7] Igarashi, Y., Ueno, M., & Fujisaki, T. (March 4-7, 2012). Proposed Node and Network Models for an M2M Internet. *Proceedings of the World Telecommunications Congress (WTC)*, (pp. 1-6). Miyazaki, Japan.

[8] Korowajczuk, L. .(2011) *LTE, WiMAX and WLAN Network Design, Optimization and Performance Analysis*. Chennai, India: Wiley.

[9] Booysen, M., Gilmore, J., Zeadally, S., & Rooyen, G. (2012). Machine to machine communication in vehicular networks. Retrieved August 12 from http://hdl.handle.net/10019.1/2076

[10] Mohr, W. (2007). Mobile Communication Beyond 3G in the Global Context. Siemens Mobile. Retrieved October 12, 2012, from http://www.6ip.cu/pdf/werner_mohr.pd

[11] Culler, D., & Hui, J. (n.d.). 6LoWPAN Tutorial-IP on IEEE 802.15.4 Low-Power Wireless Networks. Retrieved September 16, 2012, from http://www.cs.berkeley.edu/~jwhui/6lowpan/6LoWPAN-tutorial.pd

[12] Wang, W., & Chen, Y. (2010). Machine-to-Machine Communication in LTE-A. Research & Innovation Center Alcatel-Lucent Shanghai Bell.

[13] Blackman, C. (April, 1998). Convergence between Telecommunications and Other Media: How Should Regulation Adapt?. *Telecommunication Policy, 22* (3), 163-170.

[14] Network Computing. (n.d.). Retrieved on September 16, 2012 from http://www.networkcomputing.com/ipv6/six-benefits-of- ipv6/230500009

[15] Aslam, N., Robertson, W., Phillips, W., & Sivakumar, S. (October, 2007). Relay Node Selection in Randomly Deployed Homogenous Cluster-based Wireless Sensor Networks. Proceedings of the IEEE Conference Publications, International Conference on Sensor Technologies and Applications, (pp. 418-423).Valencia, Spain.

[16] Knopp, R. (October 19-20, 2010). Latency Requirements in M2M Application Scenarios. Paper presented at the European Telecommunications Standards Institute (ETSI) M2M Workshop, Sophia Antipolos, France. Retrieved on April 10, 2013 from http://docbox.etsi.org/workshop/2010/201010_M2MWORKSHOP/08_ResearchProjects/LOLA_POSTER_NIKAEIN.pd

Biographies

GARTH V. CROSBY is an Assistant Professor of Engineering Technology at Southern Illinois University Carbondale. He earned his B.S. degree from the University of the West Indies, Mona (Jamaica), and both his M.S. (Computer Engineering) and Ph.D. (Electrical Engineering) from Florida International University, Miami, USA. He is a senior member of the Institute of Electrical & Electronics Engineers (IEEE), and a member of the American Society for Engineering Education (ASEE). His current teaching interests include electronics and embedded systems. His research interests include wireless sensor networks, network security, and trust. Dr. Crosby may be reached at garth.crosby@siu.edu.

FARZAM VAFA is currently a network engineer at Highmark Health Services, PA. Mr. Vafa is a recent graduate of Southern Illinois University Carbondale (SIUC). At SIUC he obtained a Master of Science degree in Electrical Engineering. His interests include wireless communication, computer networks, and wireless sensor networks. Mr. Vafa can be reached at farzam.vafa@siu.edu.

Carbon Footprint Reduction in a Sustainable Routing Design Concept Based on Passive Cooling Ventilation Systems

Bahar Zoghi, Farmingdale State College

Abstract

Over the past decade, the effect of climate change, energy cost, and environmental concerns awakened the building sector to synchronize with nature again and look at possible ways to easily save energy. The United States, after China, has consumed most of the world's energy. The building sector is responsible for 40% of the global energy consumption and up to 30% of annual greenhouse gas (GHG) emissions. The typical lifespan of a building is around 60 to 100 years; based on this lifespan, sustainable design is the key to decreasing the energy consumption and, consequently, carbon footprint reduction. In this paper, the author presents an overview of the problem, taking into consideration climate change and a literature review of a sustainable approach based on the traditional design concept. Prior to the development of modern heating and cooling systems, buildings were designed based on local climates and were in harmony with the environment. But, by looking back on those pre-modern designs, specific building materials and building orientations can lead us to passive ventilation systems. Suggested sustainable design was used long ago in traditional building design, and is now the focus of the Leadership in Energy and Environmental Design (LEED).

Introduction

Energy limitation and global warming are two of the biggest challenges facing our era. The United States, after China, consumes most of the world's energy. The building sector is one of the major energy consumers in the world. The building sector contributes up to 40% of the global energy consumption and up to 30% of the annual greenhouse gas (GHG) emissions. At the same time, the building sector is responsible for 50.1% of the total annual U.S. energy consumption and 49.1% of the total annual U.S. greenhouse gas emissions [1]. In addition, homes and commercial buildings use 74.5% of the electricity in the United States, according to the U.S. Energy Information Agency [1].

Building sector energy consumption is expected to grow faster than industry and transportation, based on the U.S. Energy Information Administration (EIA). The EIA reports that total building sector energy will increase by 5.85 Quadrillion Btu (QBtu) between 2010 and 2030 [2].

The relationship between greenhouse gases and buildings is undeniable. Greenhouse gas emissions from buildings mainly arise from their consumption of fossil-fuel-based energy, both through the direct use of fossil fuels and through the use of electricity that has been generated from fossil fuels. Fossil fuels supply 84% of the entire U.S. and 76% of building sector energy consumption. As shown in Figure 1, the energy used in buildings is defined in four main categories: embedded energy, grey energy, induced energy, and operational energy. Operational energy has the largest portion of the energy consumption in buildings.

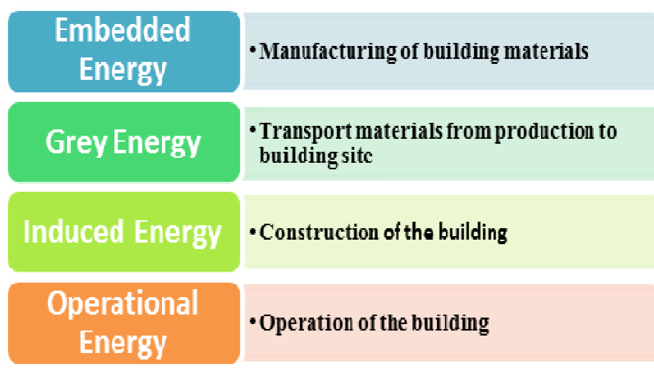

Figure 1. Energy Production During the Stage of Building Life

The primary greenhouse gas is carbon dioxide. As shown in Figure 2, atmospheric CO_2 concentrations have increased by almost 40% since pre-industrial times, from approximately 280 parts per million by volume (ppmv) in the 18th century to 390 ppmv in 2010. Figure 3 shows the recent monthly mean carbon dioxide (CO_2) and monthly mean atmospheric carbon dioxide at Mauna Loa Observatory, Hawaii. Carbon dioxide emissions increased by about 10% in the United States between 1990 and 2011 [3]. About 80% of greenhouse gas is produced during the operational phase of heating, ventilation, and air conditioning (HVAC), water heating, lighting, entertainment, and telecommunications [4].

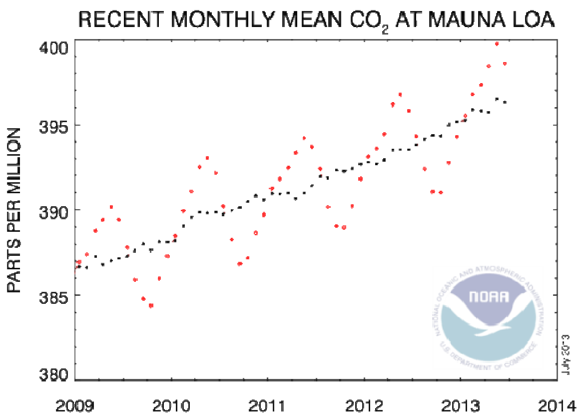

Figure 2. Recent Monthly Mean Carbon Dioxide Measured at Mauna Loa Observatory, Hawaii [5]

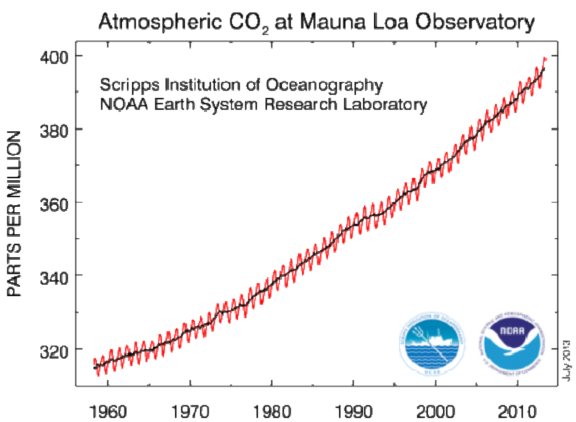

Figure 3. Monthly Mean Atmospheric Carbon at Mauna Loa Observatory, Hawaii [5]

Climate Change

Earth's average temperature has risen by 1.4°F over the past century and is projected to rise another 2 to 11.5°F over the next hundred years. Small changes in the average temperature of the planet can translate to large and potentially dangerous shifts in climate and weather [6]. The National Climatic Data Center reported that in July, 2013, Earth had its hottest temperature in climate history. This is only one of the aspects of climate change. Climate change has the following impact in the Northeast area, such as precipitation and sea level rise, impact on human health, agriculture and food supply, and forest and winter recreation [7].

Figure 4 shows how annual average temperatures in the contiguous 48 states have changed since 1901. Moreover, Figure 5 shows the temperature variance from 2003 to 2013 for the Long Island region. This temperature variation can be found for all parts of the world through the National Climatic Data Center (NCDC) website.

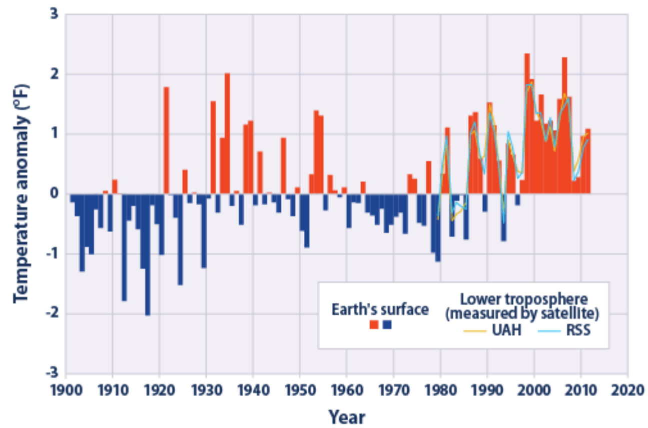

Figure 4. Temperature in the Contiguous 48 States, 1901-2011 [8]

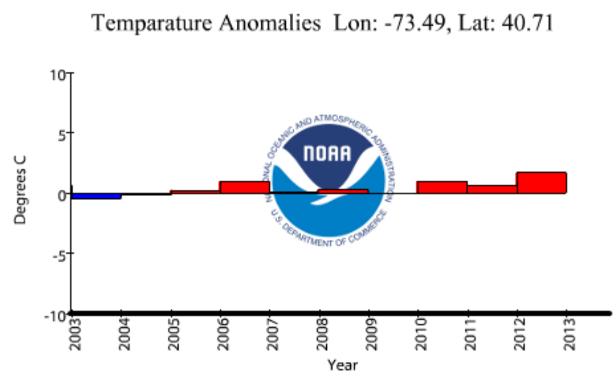

Figure 5. Temperature Anomaly for Long Island, NY [8]

Following all this information, in June, 2013, President Obama announced a series of executive actions to reduce carbon pollution and prepare the U.S. for the impacts of climate change and lead an international effort to address global climate change [9]. The following facts could be the consequences of President Obama's action plan. The National Oceanic and Atmospheric Administration (NOAA) reports that the U.S. climate extreme index in 2012 was the second most extreme year on record for the nation. New York and New Jersey were among the states with the warmest year on record. Subsequently, extreme weather changes cost the U.S. more than $100 billion. Hurricane Sandy cost almost $65 billion and efforts for resilience investment and rebuilding based on the effects from this storm are ongoing. Hurricane Sandy had a direct effect on climate change [9].

Connecting the dots, buildings in general are accountable for one third of greenhouse gas (GHG) emissions around the world. It is essential that building sector design be reevaluated in order to decrease its carbon footprint. In this paper, the author describes a passive ventilation system and its elements that could play a major role in this catastrophic issue.

Sustainable Design Aspects

There are different features of sustainable design; the focus of this study was on ventilation. In general, ventilation has many direct and indirect effects on energy consumption and the footprint of buildings. The majority of relatively new existing buildings are dependent on air-conditioning systems and electricity, and are dependent upon fossil fuels that growingly contribute to global warming.

LEED and Green Building

Several green building codes and rating systems currently address the problems that have been developed. The LEED rating system is recognized as one of the most effective and widely adopted building standards. LEED was formed by the U.S. Green Building Council (USGBC) in 2000 and "it provides building owners and operators with a framework for identifying and implementing practical and measurable green building design, construction, operations and maintenance solutions" [10]. Passive ventilation has direct and indirect impacts on the construction of buildings and, through LEED, can influence credits in energy and atmosphere. Energy from the sun can be captured and used for passive solar heating in winter. And, if the structure can be guarded against cold winds, energy can also be saved. In summer, the goal would be to capture desirable breezes and create shade to prevent solar heating in warm weather. This would also affect the indoor quality of the air, daylight, and occupant views.

Building Orientations

Building orientation can influence many features of building energy and the indoor climate. Optimal orientation has synergy with the cost of energy, internal environmental quality such as ventilation, thermal comfort, daylight, and view of the habitat space. The conventional way of building design and orientation of a building in order to capture natural energies usually does not enter into the picture. In addition, buildings are orientated to face the street and the driveways are designed to be short and as straight as possible in order to accommodate vehicles. Natural forces are free and accessible, as Bean [11] illustrates in Figure 6. Natural forces are flowing from high to low in order to create balance.

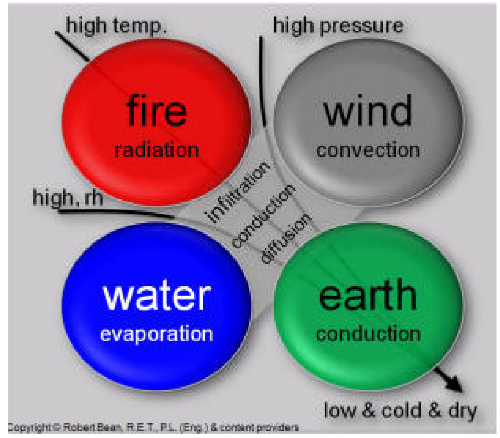

Figure 6. Forces of Nature

Building orientation to the sun has a dramatic impact on heating and cooling costs, which is the largest energy load in most buildings. The sun's position in the sky is dynamic and changing based on the time of day, time of year and latitude, as shown in Figure 7. The sun is much higher in the sky in summer, so it interacts more with high buildings and is lower in winter and relates with depth. Overhangs and trees can be used in summer to block the sun's heat.

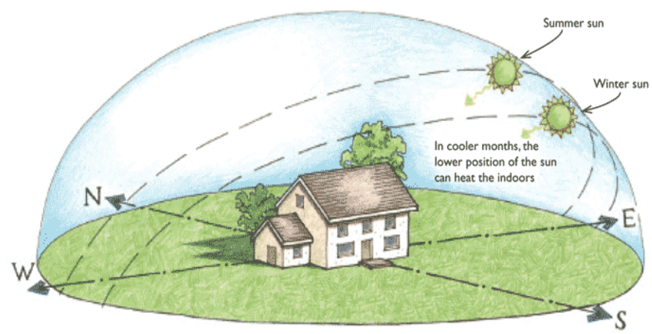

Figure 7. Building Orientation [12]

At the same time, because of the low movement of sun in the winter, buildings can benefit from the sun since its rays shine below the overhangs and the leaves are gone from the trees. In general, buildings should be orientated to benefit passive and active solar plan strategies. From a LEED point of view, there are three possible points for maintaining building orientation for passive solar. Based on LEED, meeting the following requirements could earn possible points:

- The south-facing glazing area is at least 50% greater than the sum of the glazing area on the east- and west -facing walls.

- The east-west axis of the building is within 15 degrees of due east-west.
- At least 90% of the south-facing glazing is completely shaded (by awnings, overhangs, plantings) at solar noon on the summer solstice and unshaded at noon on the winter solstice [13].

Building Materials

Building materials change building performance and energy use which leads to CO_2 reduction. A building envelope is the physical division of the interior and exterior environments of a building. The materials that are involved with the envelope are foundation, roof, walls, doors, and windows. Local climate is an important key for determining the design features that will result in the greatest reductions of energy requirements. Local climate, with the help of local materials, can bring harmony to the design. The department of energy has developed a series of practical buildings which includes five climate-specific designs in the U.S. These building best practices focus on reducing energy use and improving housing durability and comfort [14].

As mentioned in the introduction, the embodied energy is the amount of energy that is required to extract, manufacture, transport, install, and dispose of building materials. If this energy is reduced as much as possible, it has a direct effect on emissions from buildings. Besides considering local climate, locally sourced materials invariably means less transport and pollution, and offers a better chance of producing buildings and structures which are distinctive to the locality or region. This topic is mentioned in LEED as one of the grading points. The following materials have effects in building performance:

Roof:
In hot climates, roof materials and design can reduce the amount of energy to be reflected rather than absorbed by sun. In addition, as mentioned in the LEED design section on energy and atmosphere, the roof can be a site for installing onsite solar photovoltaics (PV). In this case, it could generate renewable energy compared to the consumption of indirect energy.

Walls:
Design and materials of walls impact the amount of energy that is lost or reserved through walls. Options such as solar or Trombe wall can be considered in the sustainable design. A solar wall is a passive solar system originally perceived for passive heating of buildings. It is usually made up of south-facing concrete walls painted black on external surfaces with an air layer and glazing on the exterior side. Shading devices such as overhangs deliver solar radiation control. The walls gather and store solar energy using their internal mass and are not insulated since heat exchange with the internal atmosphere is by transmission through the walls. A Trombe wall is a solar wall with vents at the top and bottom for the air thermo circulation. Figure 8 shows typical operation schemes for solar and Trombe walls [15].

In addition, the material selection and wall insulation both affect the building's thermal properties. A building's thermal property is the capability to store heat. Thermal mass materials such as stone and adobe absorb energy more slowly and hold it longer, effectively reducing indoor tempera-

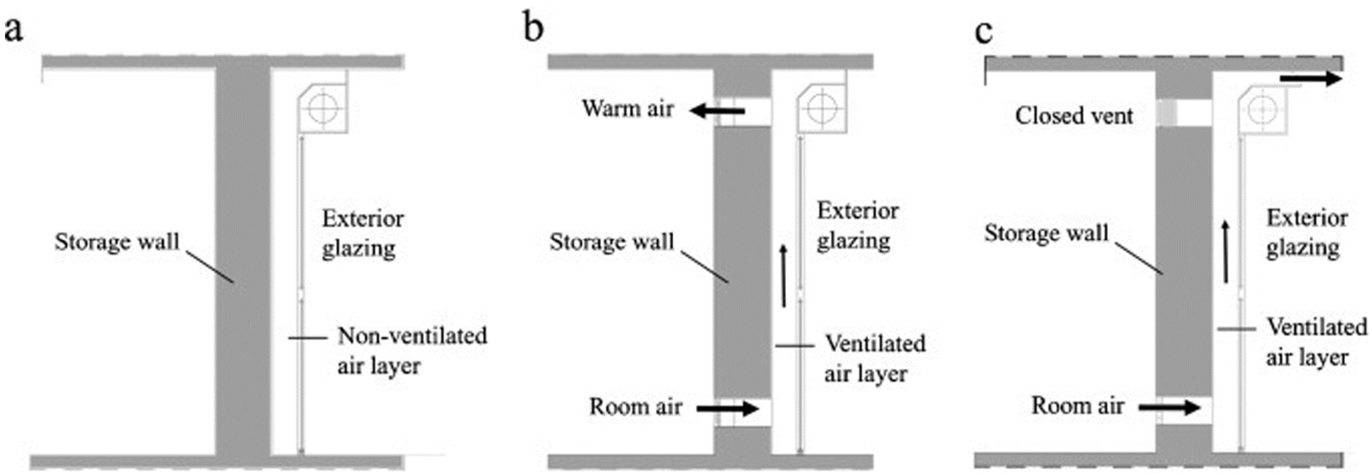

(a) Non-Ventilated Solar Wall **(b) Trombe Wall in Winter Mode with Air Thermo-Circulation** **(c) Trombe Wall in Summer Mode with Cross Ventilation**

Figure 8. Operation of Various Walls [15]

ture fluctuations and reducing overall heating and cooling requirements. These materials can be considered as wall materials if the solar or Trombe wall is not the choice.

Windows and doors:
Windows, exterior doors, and skylights, known as fenestration, impact both lighting and HVAC in the building. Using all optimum window design and glazing in residential buildings are estimated to reduce energy consumption from 10 to 50 percent below accepted practice in most climates [16]. Based on the study by Susorov et. al. [17], a series of energy simulations were performed for six climate zones in the United States using a model of a room in a typical office building created in Design Builder, an energy analysis program, to evaluate total annual energy consumption. Energy savings were, on average, 3% and 6%, reaching a maximum of 10% and 14% in hot climates.

Besides the window thermal properties in energy-efficient fenestration design, the window orientation, window-to-wall ratio, and room width-to-depth ratio are important factors, too. Thermal transmittance (or *U*-value) characterizes the rate of heat transfer through fenestration under certain environmental conditions. Alongside design deliberation, materials and installation have an effect on the amount of energy transmitted through the window, door, or skylight; new materials, coatings, and enhanced energy efficiency designs for high-performance windows, doors, and buildings must also be considered. Advanced window designs include multiple glazings and the use of two or more panes of glass for insulation. The space between panes can be further improved by filling it with a low-conductivity gas and low-emissivity (low-e) coatings. This plug reduces the flow of infrared energy from the building to the environment. In addition, installing operable windows, which occupants can control, takes advantage of natural ventilation.

Passive-Cooling Ventilation

Passive ventilation is a factor of all terms that were discussed in previous sections, although the orientations of the building and building materials have the biggest effect on it. Prior to the development of modern heating and cooling systems, buildings were designed based on local climates and were in harmony with the environment. Passive ventilation can be applied by using the thermodynamic laws of energy transfer from high to low. In passive cooling systems, heat and pressure are forms of energy. Heat transfer, which is explained by thermodynamics, has four fundamental modes: conduction, convection, radiation, and advection, all of which are used in passive ventilation.

Review of Passive Cooling Sustainable Designs

The proposed method is uses ancient wind catchers in conjunction with solar or Trombe walls. The wind catcher is a traditional Persian architectural device used for many centuries to create natural ventilation in buildings [18]. This noble, clean energy masterpiece design was widely used in the Middle East in ancient times. Figure 9 shows the tallest wind catcher in Dowlat Abad garden in Yazd, Iran. This wind catcher is 33.8 m (110 ft) and is made of brick. A wind catcher operates according to the wind direction and sun radiation. It looks like a chimney, but its end is underground and its top is set over a specific height on the roof. At the top outlet, many small openings or ducts are set. It is usually built over an underground water reservoir or pond (aqueducts), if possible.

Figure 9. Tallest Wind Catcher [19]

There are different kinds of wind catchers in two different climates in Iran: hot and humid, and hot and dry. The wind catcher is induced either by thermal buoyancy or by wind. When wind hits the building, it creates a positive pressure on the windward side (away from the wind) and negative pressure on the leeward side (toward the wind). This pressure difference based on thermodynamic laws acts as a driving force and starts ventilation by allowing air to flow into the building through the windward opening and leave the building through the leeward opening. Figure 10 shows the system.

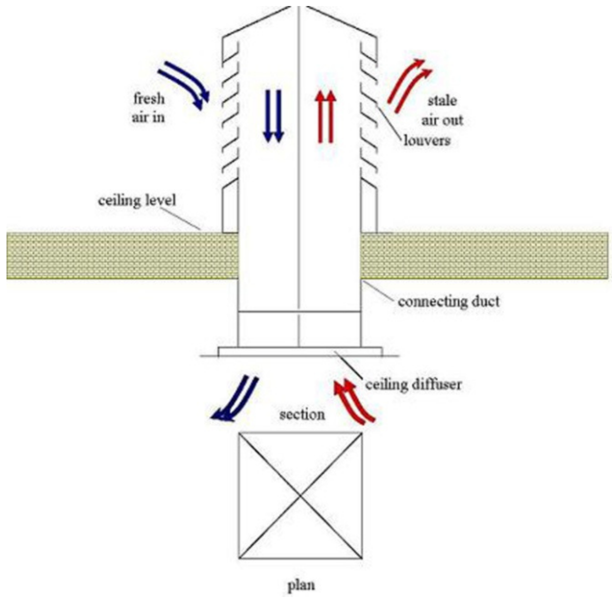

Figure 10. Schematic of Wind Catcher Operation [20]

For the simple case of cross ventilation with an isolated enclosure, the air flow rate can be calculated using Equation (1) [21].

$$Q = K \text{ x } A \text{ x } V \tag{1}$$

where,

Q = air flow (cfs)
K = coefficient of effectiveness
A = cross sectional area of the opening $(\text{ft})^2$
V = speed of outside air (ft/s)

Wind direction and intensity are the only factors that affect the ventilation of wind-catcher ventilation. These two elements together make design consideration very challenging. Buoyancy-driven ventilation depends on the temperature difference between the inside and outside of the building as well as between different zones within the building. The wind-catcher material also plays an important role. Due to a high fluctuation in temperature differences between day and night in the hot/dry climate, they are made with a mud-brick material. Mud-brick or adobe is cooled by radiation and convection. The system works, even in hot, windless summer days.

Typologies of Wind Catchers

Wind catchers were found in diverse forms and plans such as circle, octagon, polygon, square and oblong. No triangular form of it has yet been recognized or located anywhere in the Middle East [22]. The blades of wind catchers can be categorized as main and side blades. Main blades have an operational role compared with the side blades that have only aesthetic value [22]. The most common form of wind catcher has been the oblong plan, as shown in Figures 11 and 12.

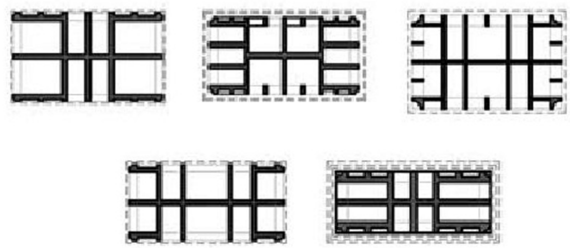

Figure 11. Wind Catchers with +Form Blades and Different Canals [23]

Figure 12. 3D Model of a Wind Catcher with Equal Canals [24]

Conclusion

The combination of high demand for indoor air quality and thermal comfort at the same time as low environmental impact and carbon footprint, make it necessary to develop a sustainable method for heating, ventilation, and air conditioning (HVAC). Erudition from empirical evidence of the originality of historical buildings, which were in agreement with nature, were considered. Local climate and materials, building orientation, and passive ventilation are great tools for making peace with nature and being in harmony with the environment.

References

[1] U.S. Energy Information Administration. (December 2008). *Annual Energy Outlook 2009, Early Release: Tables 2, 4, 5, and 18.* Using 2008 data. Retrieved from http://www.eia.doe.gov/oiaf/aeo/aeoref_tab.htm

[2] U.S. Energy Information Administration. (December 2008). *Annual Energy Outlook 2009, Tables 2, 4, and 5.* Using 2008 data. U.S. Energy Information. Retrieved from http://www.eia.doe.gov/oiaf/aeo/aeoref_tab.htm

[3] U.S. Department of Environmental Protection Agency (EPA). Retrieved from http://www.epa.gov/climatechange/ghgemissions/gases/co2.html#Trend

[4] Seppo, J. (2004). *An Environmental Impact of an Office Building throughout its Life Cycle. Espoo, Helsinki University of Technology Construction Economics and Management*. Doctoral Dissertation, Aalto University Schools of Technology. (ISBN 951-22-7284-9).

[5] National Oceanic and Atmospheric Administration, NOAA. (2013). *Earth System Research Laboratory.* Retrieved from http://www.esrl.noaa.gov/gmd/ccgg/trend.

[6] U.S. Department of Environmental Protection Agency (EPA). Retrieved from http://www.epa.gov/climatechange/basics

[7] Karl, T. R., Melillo, J. M., & Peterson, T. C. (2009). U.S. Global Climate Change Research Program, USGCRP. *Global Climate Change Impacts in the United State*. Cambridge University Press, New York, NY, USA.

[8] National Oceanic and Atmospheric Administration, NOAA. (2013). *National Climatic Data Center (NCDC).*

[9] White House. (June 2013). President Obama's Plan to Fight Climate Change. Retrieved from http://www.whitehouse.gov/share/climate-action-pla

[10] U.S. Green Building Council. (2010). *LEED public policies*. Retrieved from https://www.usgbc.org/ShowFile.aspx?DocumentID=792

[11] Bean, R. (2012). *Healthy Heating*. Retrieved July 2013 from, http://www.healthyheating.com/Building-Orientation.

[12] Green Basics. Retrieved July 2013 from http://www.greenbuildingadvisor.com/green-basics

[13] U.S. Green Building Council. (2013). Retrieved from http://www.usgbc.org/node/2612068?return=/credits/homes/v4-draf

[14] U.S. Department of Energy. (DOE). Retrieved from http://www1.eere.energy.gov/buildings/building_america/publications.htm

[15] Stazi, F., Mastrucci, A.,& Pema, C (April 2012). The behaviour of solar walls in residential buildings with different insulation levels. *Energy and Building*, *47*, 217-229.

[16] Ander, G. D. (June 2010). Windows and Glazing. Whole Building Design Guide.

[17] Susorov, I., Tabibzade, M., Rahma, A., Clac, H. L., & Elnimeir, M. (February, 2013). The effect of geometry factors on fenestration energy performance and energy savings in office buildings. *Energy and Building, 57*, 6-13

[18] Bahadori, M. N. (August 1994). Viability of wind towers in achieving summer comfort in the hot arid regions of the Middle East. *Renewable Energy, 5,* 879–892.

[19] Skyscraperpage. Retrieved July 2013 from http://forum.skyscraperpage.com/showthread.php?t=19121

[20] Li, L., & Mak, C. M. (2005). The assessment of the performance of a wind catcher system using CFD. *Building & Environment, 42*, 1135-1141.

[21] Bansal, N. K., Mathur, R., & Bhandari, M. S. (1993). Solar chimney for enhanced stack ventilation. *Building and Environment, 28*(3), 373-377.

[22] Amirkhani, A., Zamani, E., Saidian, A., & Khademi, M. (June 2010). Wind Catchers: Remarkable Example of Iranian Sustainable Architecture. *Journal of Sustainable Development*, *3*(2).

[23] Mofidi, S. (2008). Analysis on typology and architecture of wind catcher and finding the best type. *Honarhaye Ziba Journal, 36*, 29.

[24] Roaf, S. (1989). *The Windcatchers of Yazd*. Doctoral Dissertation, Oxford Polytechnic.

Biographies

BAHAR ZOGHI is an Assistant Professor of the Architecture and Construction Management Department of the Farmingdale State College of New York State University. She earned her B.S. degree from Polytechnic of Tehran (Civil Engineering, 1997) MS (Civil Engineering, 2002) from City College of New York, and Ph.D. (Civil Engineering, 2006) from the Graduate Center of City University of New York. Dr. Zoghi is a Professional Engineer and LEED accredited professional. Her interests are in sustainable and renewable energy and green building. Dr. Zoghi may be reached at Zoghimb@farmingdale.edu

APPLICATION OF A LINEARIZED SMALL-SIGNAL SWITCHED RELUCTANCE MOTOR MODEL FOR DEVELOPING A GENERAL-PURPOSE VARIABLE-SPEED DRIVE

Shiyoung Lee, Pennsylvania State University, Berks Campus

Abstract

In this study, a linearized small-signal model of a switched reluctance motor (SRM) was applied to design both PI velocity and current controllers to implement an SRM-based variable speed drive (VSD). Step-by-step PI velocity and current controller design techniques are introduced in this paper and experimental verification with a prototype SRM drive system is compared with simulation results to validate the proposed design methods. The simulation of both the design model and the actual system show a slight deviation in the actual VSD system performance versus the design model performance. The dynamic simulations of the actual model with various operating points show how the selection of parameters for the linearized system affects the performance of the actual VSD system. The proposed linearized small-signal SRM model can be applied to any SRM-based VSD system.

Introduction

The SRM is a viable candidate for many VSD applications because of its reliability and cost [1]. Currently, there are few analytical methods from which to design an SRM to meet speed performance specifications. Several speed and current controllers have been proposed for SRMs. Most controllers require digital signal processors (DSP) or high-end microcontrollers as part of their architecture [2-8]. However, these controllers lack the necessary flexibility and performance capabilities, excluding the SRM, for many of the general-purpose drive applications.

The issue this study addressed was the need for a low-cost SRM speed and current controller that could maintain an acceptable level of performance. Besides the need for a low-cost controller, there are few systematic design techniques that allow engineers to freely set control parameters. Previous research has dealt with design of speed and current controllers using feedback linearization [9-12] and observers [13], [14]. These types of precise control add to the cost and complexity of the controller.

The purpose of this study was to develop a control design methodology suitable for SRMs in general-purpose applications. There were two specific goals. First, the controller must be able to maintain a level of performance common to general-purpose motor drive controllers. Some primary capabilities of general-purpose motor drive controllers include four-quadrant operation, adaptability to specific applications, and the ability to achieve a high level of efficiency. The second goal was to develop a technique by which the speed and current controller gains could be analytically calculated and the performance analyzed by simulation. The proposed architecture of the SRM controller was a hybrid architecture consisting of both analog and digital hardware. There were three control blocks in the SRM-based VSD. The first two control blocks were the current control and speed control. Both of these types of control were accomplished with analog hardware. The third control block was the phase firing control, which was accomplished using digital hardware. The controller provides an interface between the analog and digital hardware for control coordination, and it also provides an interface to the converter, motor, and user.

For industrial drives, such as induction motor and dc motor drives, there are systematic design techniques for current and speed control loop design, which allows engineers to analyze their designs before construction [15]. This paper provides a simple design technique based on the linearized small-signal SRM model. For general-purpose VSD applications, this design technique is sufficient for choosing PI gains for the speed and current controllers. A prototype SRM was used to illustrate the effectiveness of the design technique in determining the gains of the controllers. Experimental and simulation results are given to illustrate the effect of varying design choices in the proposed design methodology.

Design of Speed and Current Controllers

It is difficult to construct a design model of an SRM because of the motor's nonlinear nature. The SRM's torque is proportional to the input current squared, and the back-EMF is proportional to the product of current and speed. In this paper, the author proposes linearized SRM voltage and torque equations for deriving a small-signal SRM model at the rated current and speed.

SRM Voltage and Torque Equations

The voltage and torque equations of an SRM were used to derive the small-signal SRM model shown below [1].

Voltage Equation $$V = R_p i + \frac{d(\theta,i)}{dt} \qquad (1)$$

Torque Equation $$T_e(\theta,i) - T_l = J\frac{d\omega}{dt} + B\omega \qquad (2)$$

The flux linkages, λ, and the air gap torque, T_e, are dependent on the phase current and the rotor position in the above equations. It is desirable to have the voltage and torque equations in a form similar to the separately excited dc motor. The separately excited dc motor is the easiest of all electric motors to deal with, and standard design procedures are well established for it [15].

The voltage equation becomes the following by using the relationship between the flux linkages and inductance, $L(\theta,i)i = \lambda(\theta,i)$:

$$V = R_p i + \frac{dL(\theta,i)i}{dt} = R_p i + L(\theta+)\frac{di}{dt} + \frac{dL(\theta,i)}{dq}\omega_m i \qquad (3)$$

In Equation (3), the three terms on the right-hand side represent the resistive, inductive, and back-EMF terms, respectively, similar to the separately excited dc motor voltage equation.

Similarly, it is desirable to arrange the torque equation into a form similar to that of the separately excited dc motor torque equation. The torque is related to the current flows in the SRM phase winding. The following equations show the relationship between the torque and the current in one phase winding of the SRM.

Energy in an Inductor:

$$\frac{d}{dt}\left(\frac{1}{2}L(\theta,i)i^2\right) = L(\theta q,\imath)i\frac{di}{dt} + \frac{1}{2}i^2\frac{dL(\theta,i)}{dt} \qquad (4)$$

Power in the SRM:

$$P = Vi = R_p i^2 + i^2\frac{dL(\theta,i)}{dt} + L(\theta,i)i\frac{di}{dt} \qquad (5)$$

By substituting Equation (4) into Equation (5), the power in the SRM becomes the following:

$$P = R_p i^2 + \frac{1}{2}i^2\frac{dL(\theta,i)}{dt} + \frac{d}{dt}\left(\frac{1}{2}L(\theta,i)i^2\right) \qquad (6)$$

The power in the SRM is represented by the three terms shown in Equation (6), which are the copper losses, air gap power, and rate of change of stored energy in the phase. The air gap power is used to determine the air gap torque in that the air gap power is equal to air gap torque times the rotor speed:

Air gap Power:

$$P_a = \frac{1}{2}i^2\frac{dL(\theta,i)}{dt} = \frac{1}{2}i^2\frac{dL(\theta,i)}{dq}\omega w_m \qquad (7)$$

Air gap Torque:

$$T_e = \frac{1}{2}i^2\frac{dL(\theta,i)}{dq} \qquad (8)$$

The resulting torque equation for the SRM is:

$$\frac{1}{2}i^2\frac{dL(\theta,i)}{d\theta\theta} - T_l = J\frac{d\omega\omega}{dt} + B\omega \qquad (9)$$

Derivation of the Linearized Small-Signal SRM Model

The selected states of the SRM model are the rotor speed, ω_m, and the phase current, i. The SRM voltage and torque equations result in a nonlinear system because the states are multiplied together, as shown in Equations (1) and (2). For general-purpose SRM VSDs, it is desirable to have a simple model in order to design the speed and current controllers effectively. The simplest approach is linearization of the actual model [16-20]. This paper takes the approach of deriving a linearized small-signal model of the SRM system equations.

The SRM system model may be written in the following form:

$$\dot{x} = \begin{bmatrix} \left(\frac{u_1}{L} - \frac{R_p}{L}x_1 - \frac{1}{L}\frac{dL}{dq}x_1x_2\right) \\ \left(\frac{1}{2J}x_1^2\frac{dL}{dq} - \frac{u_2}{J} - \frac{B}{J}x_2\right) \end{bmatrix} = f(x,u,t) \qquad (10)$$

where,

$x_1 = i$, $x_2 = \omega_m$, $u_1 = V$, and $u_2 = T_l$.

In the previous equation, for the simplification of design process, the inductance $L = L(\theta,i)$ is considered to be constant. The mean value between the aligned and the unaligned inductances at rated current is used as the inductance. The derivative of inductance with respect to rotor position is calculated between the conduction angles at the rated current value and is assumed to be a constant. It shows only a small change over the entire operating range of the SRM.

By using the linearization analysis of small deviations from the nominal, the following is the derivation procedure of the small-signal model.

$$x(t) = x_n(t) - dx \qquad (11)$$

$$u(t) = u_n(t) - du \qquad (12)$$

$$\dot{x}(t) = \dot{x}_n(t) - d\dot{x} = f(x_n, u_n, t) + \left[\frac{\partial f}{\partial x}\right]dx + \left[\frac{\partial f}{\partial u}\right]du \qquad (13)$$

$$\dot{x} = \begin{bmatrix} \frac{\partial f_1}{\partial x_1} & \frac{\partial f_1}{\partial x_2} \\ \frac{\partial f_2}{\partial x_1} & \frac{\partial f_2}{\partial x_2} \end{bmatrix} \qquad (14)$$

$$\dot{u} = \begin{bmatrix} \frac{\partial f_1}{\partial u_1} & \frac{\partial f_1}{\partial u_2} \\ \frac{\partial f_2}{\partial u_1} & \frac{\partial f_2}{\partial u_2} \end{bmatrix} \qquad (15)$$

where,

$$\frac{\partial f_1}{\partial x_1} = -\frac{R_p}{L} - \frac{1}{L}\frac{dL}{dq}x_{20} \quad \frac{\partial f_1}{\partial x_2} = -\frac{1}{L}\frac{dL}{dq}x_{10} \quad \frac{\partial f_2}{\partial x_1} = -\frac{1}{J}\frac{dL}{dq}x_{10}$$

$$\frac{\partial f_2}{\partial x_2} = -\frac{B}{J} \quad \frac{\partial f_1}{\partial u_1} = \frac{1}{L} \quad \frac{\partial f_2}{\partial u_2} = -\frac{1}{J} \quad \frac{\partial f_1}{\partial u_2} = \frac{\partial f_2}{\partial u_1} = 0$$

and x_{10} is the rated current and x_{20} is the rated speed.

While the total linearized system contains a steady-state portion, $x_n(t)$ and $u_n(t)$, that has a constant value determined by the rated speed and current of the SRM, the small-signal deviation portion of the linearized system is of more interest in developing the design model. Therefore, the steady-state portion is ignored in order to develop the design model. The following is the set of linearized small-signal voltage and torque equations:

$$\frac{d\delta}{dt} = \left(-\frac{R_p}{L} - \frac{1}{L}\frac{dL}{d\theta}\omega_{mo}\right)d\delta - \frac{1}{L}\frac{dL}{d\theta}i_o d\omega_m + \frac{d\delta}{L} \qquad (16)$$

$$\frac{d\delta\omega_m}{dt} = \left(-\frac{1}{J}\frac{dL}{d\theta}i_o\right)d\delta i - \frac{B}{J}\delta\omega_m + \frac{dT_l}{J} \qquad (17)$$

After substituting the rated speed, ω_{mo}, and the rated current, i_o, a linear model was achieved which was used to design the controllers. For the rest of the derivation, the following substitutions were used:

$$R = R_p + \frac{dL}{d\theta}\omega_{mo} \qquad (18)$$

$$K_b = \frac{dL}{d\theta}i_o \qquad (19)$$

The following block diagram shown in Figure 1 can be obtained to illustrate the linearized small-signal SRM model based on the small-signal voltage and torque equations. This model was similar to the separately excited dc motor model. It was desirable to reduce the block diagram model to eliminate the back-EMF feedback loop. The back-EMF feedback loop crossed over the current feedback loop and complicated the controller design. Therefore, by making the torque load equal to a friction constant B_l times the speed, the block diagram was reduced to the following [14]:

The constants in Figure 1 are defined below as

$$B_t = B + B_l \qquad (20)$$

$$K_1 = \frac{B_t}{K_b^2 + RB_t} \qquad (21)$$

$$T_m = \frac{J}{B_t} \qquad (22)$$

$$-\frac{1}{T_1}, -\frac{1}{T_2} = -\frac{1}{2}\left[\frac{B_t}{J} + \frac{R}{L}\right] \pm \sqrt{\frac{1}{4}\left(\frac{B_t}{J} + \frac{R}{L}\right)^2 - \frac{K_b^2 + RB_t}{JL}} \qquad (23)$$

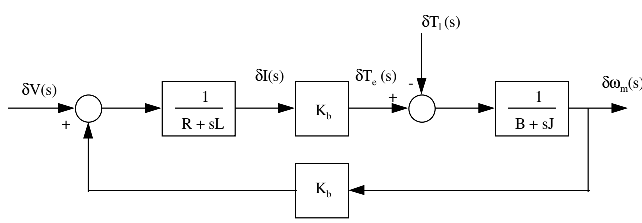

(a) Simplified Block Diagram of the Linearized SRM Model

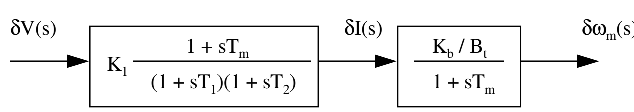

(b) Reduced Block Diagram of the Linearized SRM Model

Figure 1. Original and Reduced Block Diagrams of the Linearized SRM Model

Current Controller Design with the Linearized Small-Signal SRM Model

The entire block diagram of the proposed SRM-based VSD is given in Figure 2 for reference. For the rest of the paper, the small-signal model is treated as the design model, where $\delta I(s) = I(s)$, $\delta\omega_m(s) = \omega_m(s)$, etc. Once the linearized small-signal SRM model was identified, the current controller was designed. A PI controller was selected for the current controller because of its simplicity to implement, and the integral portion of the controller would prevent the control signal from varying erratically between the saturation levels of the controller.

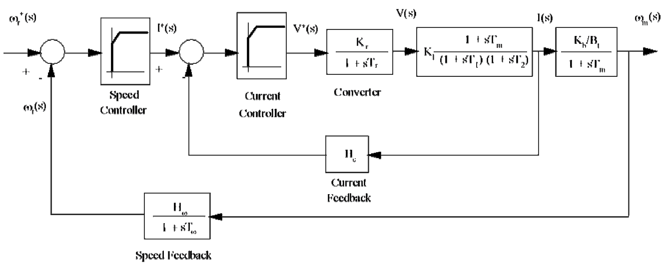

Figure 2. Overall Block Diagram of the SRM-Based VSD

The block diagram of the current loop is given in Figure 3. The converter had a delay, T_r, but it was assumed to be ten times faster than the current loop delay and not considered in the design process for simplification purposes. The current loop transfer function is shown in Equation (24):

$$\frac{I(s)}{I^*(s)} = \frac{b_0 + b_1 s + b_2 s^2}{a_0 + a_1 s + a_2 s^2 + a_3 s^3} \tag{24}$$

where,

$b_0 = K_c K_r K_1$, $b_1 = K_c K_r K_1 (T_c + T_m)$, $b_2 = K_c K_r K_1 T_c T_m$, $a_0 = H_c K_c K_r K_1$, $a_1 = T_c + T_m H_c K_c K_r K_1 + T_c H_c K_c K_r K_1$, $a_2 = T_c T_1 + T_c T_2 + T_c T_m H_c K_c K_r K_1$, $a_3 = T_c T_1 T_2$.

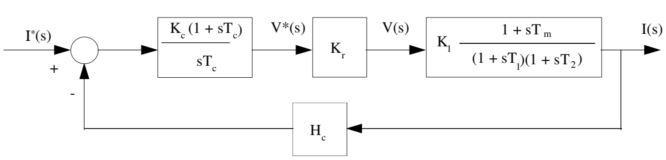

Figure 3. Current Loop Block Diagram

The term $(1+sT_m)$ was approximated as sT_m because the mechanical time constant of the system, T_m, was large enough. With this approximation, the current loop became a second-order system in which second-order system design techniques were applied. Below is the approximated system:

$$\frac{I(s)}{I^*(s)} = \frac{K_c K_r K_1 T_m (1+sT_c)}{T_c (1+sT_1)(1+sT_2) + H_c K_c K_r K_1 T_m (1+sT_c)} \tag{25}$$

It was desirable to specify a bandwidth for the current loop based on the switching frequency of the converter to design the current controller gain and time constant. The bandwidth of the converter must be ten times faster than the bandwidth of the current loop to approximate the converter as a simple gain block. The characteristic equation of the approximated current loop in Equation (26) was needed to design the current controller using the bandwidth method.

$$s^2 + s\left(\frac{T_1 + T_2 + H_c K_c K_r K_1 T_m}{T_1 T_2}\right) + \frac{H_c K_c K_r K_1 T_m + T_c}{T_c T_1 T_2} \tag{26}$$

The natural frequency, ω_n, and damping ratio, δ, were used to obtain the current controller gain and time constant since the characteristic equation was a second-order equation. The damping ratio and the natural frequency of the approximated system are specified in Equations (27) and (28).

$$2\delta\omega_n = \frac{T_1 + T_2 + H_c K_c K_r K_1 T_m}{T_1 T_2} \tag{27}$$

$$\omega_n^2 = \frac{H_c K_c K_r K_1 T_m + T_c}{T_c T_1 T_2} \tag{28}$$

The gain, K_c, and the time constant, T_c, were solved for a given natural frequency and damping ratio from these two equations. The derived K_c and T_c equations are

$$K_c = \frac{2dT_1 T_2 \omega_n - T_1 - T_2}{H_c K_r K_1 T_m} \tag{29}$$

$$T_c = \frac{H_c K_c K_r K_1 T_m}{T_1 T_2 \omega_n^2 - 1} \tag{30}$$

Once the gain and time constant of the current controller were found, the exact current loop was simulated for a step response and frequency response.

Design of the Speed Controller with the Linearized Small-Signal SRM Model

Once the current loop was defined, the outer speed loop was designed. In order to design the speed controller gain and time constant, the symmetric optimum method was chosen. The symmetric optimum method gives a flat frequency response over the bandwidth of the system, optimum phase margin, and stability [15]. For general-purpose systems, the bandwidth is not as much of a concern as the tracking capability of the general-purpose drive may not be an issue. This is the reason why the symmetric optimum method was chosen for the speed controller design over the bandwidth method [21].

It was assumed that the delay of the current loop was ten times faster than the response of the speed loop when designing the speed loop. Therefore, the current loop gain was approximated as a unity to simplify the design equations. Normally, the delay due to the speed feedback is neglected, which reduces the speed loop to a second-order system. It must be considered in the design process when the speed feedback delay is slow compared to the delay of the other subsystems [1]. Figure 4 is the block diagram of the approximated speed loop.

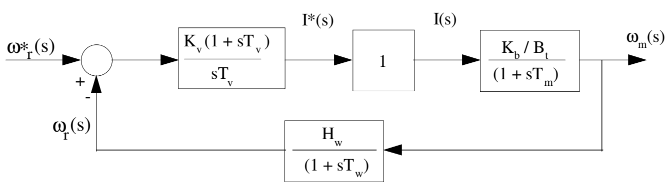

Figure 4. Approximated Speed Loop Block Diagram

The transfer function for the approximated speed loop is given by Equation (31):

$$\frac{\omega_m(s)}{\omega_r^*(s)}=\frac{K_bK_v(1+T_v)(1+T_w)}{T_vH_cB_ts(1+sT_m)(1+T_w)+H_wK_bK_v(1+sT_v)} \tag{31}$$

The design by the symmetric optimum is made easier if the transfer function is in the following form:

$$\frac{\omega_m(s)}{\omega_r^*(s)}=\frac{d_0+d_1s+d_2s^2}{c_0+c_1s+c_2s^2+c_3s^3} \tag{32}$$

where,

$$d_0 = K_vK_b \quad d_1 = K_vK_b(T_v + T_w) \quad d_2 = K_vK_bT_vT_w$$

$$c_0 = H_wK_bK_v \quad c_1 = H_wK_bK_vT_v + B_tT_v$$

$$c_2 = (T_m + T_w)B_tT_v \quad c_3 = T_mT_wB_tT_v$$

To develop a speed controller which gives a symmetric optimum performance, the frequency magnitude response is taken from Equation (32).

$$\left|\frac{\omega_m(j\omega)}{\omega_r^*(j\omega)}\right|=\sqrt{\frac{d_0^2+(d_1^2-2d_0d_2)\omega^2+d_2^2\omega^4}{c_0^2+(c_1^2-2c_0c_2)\omega^2+(c_2^2-2c_1c_3)\omega^4+c_3^2\omega^6}} \tag{33}$$

From Equation (33), the two middle coefficients of the denominator need to be zero for the system to be a symmetric optimum. Therefore, the two following conditions must hold:

$$c_1^2 = 2c_0c_2 \tag{34}$$

$$c_2^2 = 2c_1c_3 \tag{35}$$

Following the calculation of the speed controller gains, the step response was obtained from the approximated speed loop. By using Equation (35), the speed controller gain was obtained, and by using Equation (37), the speed controller time constant was calculated.

$$K_v = \frac{B_t((T_m + T_w)^2 - 2T_mT_w)}{2K_bT_mT_wH_w} \tag{36}$$

$$T_v = \frac{2H_wK_bK_v(T_m + T_w)B_t}{(B_t + H_wK_bK_v)^2} \tag{37}$$

To get a better view of how the entire system responds, the exact speed loop step response and frequency response must be obtained. The exact speed loop transfer function includes the transfer function of the current loop and has the following form:

$$\frac{\omega_m(s)}{\omega_r^*(s)}=\frac{e_0+e_1s+e_2s^2+e_3s^3+e_4s^4}{f_0+f_1s+f_2s^2+f_3s^3+f_4s^4+f_5s^5+f_6s^6} \tag{38}$$

where,

a_0 to a_3 and b_0 to b_2 are obtained from Equation (24) and,

$$e_0=b_0K_bK_v \quad e_1=(b_1+b_0(T_v+T_w))K_bK_v$$

$$e_2=(b_2+b_1(T_v+T_w)+b_0T_vT_m)K_bK_v$$

$$e_3=(b_1T_vT_m+b_2(T_v+T_w))K_bK_v \quad e_4=T_vT_mK_bK_vb_2$$

$$f_0=K_bK_vH_wb_0 \quad f_1=B_tT_va_0+b_0H_wK_bK_v+K_bK_vH_wb_1$$

$$f_2=B_tT_va_1+b_2H_wK_bK_v+T_vK_bK_vH_wb_1+T_vB_t(T_m+T_w)a_0$$

$$f_3=B_tT_va_2+a_0T_wT_mB_tT_v+T_vK_bK_vH_wb_2+T_vB_t(T_m+T_w)a_1$$

$$f_4=B_tT_va_3+a_1T_wT_mB_tT_v+T_vB_t(T_m+T_w)a_2$$

$$f_5=a_2T_wT_mB_tT_v+T_vB_t(T_m+T_w)a_3 \quad f_6=a_3T_wT_mB_tT_v$$

After simulating the step response of the exact system, there is often a large overshoot due to the time constant of the speed controller. To minimize the overshoot of the system, it is desirable to cancel the zero due to the speed controller time constant with a pole of the same magnitude. This is a soft-start for the drive system and it is implemented with a simple RC low-pass filter circuit [15]. Upon designing the soft start, the system is simulated once more to observe the change in the step response and frequency response.

Design of the Prototype SRM Drive

An SRM VSD system based on a 5hp SRM-based VSD was designed to validate the developed design technique using the linearized small-signal model. The specifications for the 5 hp SRM-based VSD are listed in Table 1:

Table 1. SRM-Based VSD Parameters

Velocity Command	±10 V	Rated Speed	2,500 r/min
Bus Voltage	400 Vdc	Rotor Friction Constant	0.001 N-m/rad/s
Maximum Current	15A	Rotor Inertia	0.006 kg-m^2
PWM Frequency	8 kHz	Speed Feedback Gain	0.383 V/rad/s
Phase Resistance	0.931W	Speed Feedback Time Constant	0.1s
Power	5 hp	Unaligned Inductance	3.4 mH
Back-EMF Constant	0.96 V/1Kr/min	Aligned Inductance	31.8 mH
Rated Current	10A		

The following constants listed in Table 2 were calculated to design the speed controller and current controller with the linearized small-signal SRM model.

Table 2. SRM-Based VSD Design Constants

Slope of Inductance Curve	$dL/d\theta$	*0.234 H/rad*
Linearized Torque/Back -EMF Constant	(19)	K_b=2.81
Linearized Phase Resistance	(18)	R=62Ω
Converter Gain	$K_r = V_{dc}/V^*_{max}$	40
Current Transducer Gain	$H_c = i^*_{max}/i_{max}$	0.667 V/A
Speed Transducer Gain	$H_\omega = \omega_{r-max}/\omega_{m-max}$	$H_\omega = 0.0382$
Speed Transducer Delay		T_w = 0.01 s
Total Friction Constant	(20)	*0.001*
Gain	(21)	*0.000126*
Mechanical Time Constant	(22)	*6 s*
Motor Transfer Function	(23)	T_1 = 0.0464 s T_2 = 0.000359 s

Current Controller Design

Equations (29) - (30) were used to design the current controller gain and time constant: K_c=9.42 and T_c=0.000113. For the prototype, a bandwidth of 1.6 kHz and damping ratio of 0.707 were targeted for the current loop. Shown below are the current controller gain and time constant. Figure 5 shows the step response of the current loop transfer function described in Equation (24). The current loop was given the maximum step current command of 10 V and the result was the maximum current of 15 A. The current loop had a rise time of 0.14 ms, 13% overshoot, and settling time of 0.5 ms. The exact step response is shown, which does not approximate the mechanical time constant, T_m.

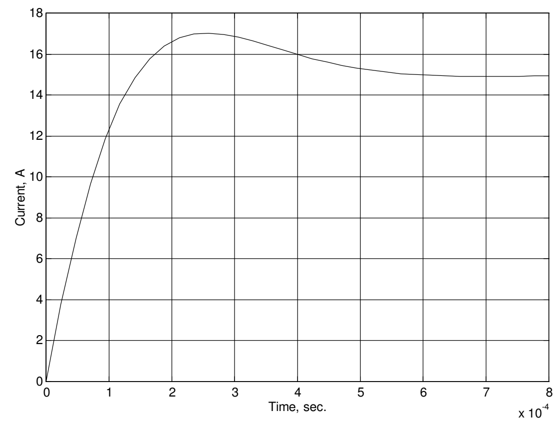

Figure 5. Step Response of the Current Loop Transfer Function in Equation (24)

The frequency response in Figure 6 shows that the designed control loop meets the bandwidth of 1.6 kHz. With the exception of a slightly larger overshoot due to the exact mechanical time constant, the design meets specifications.

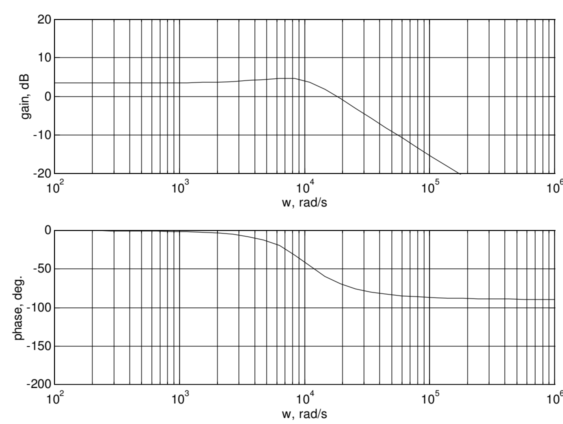

Figure 6. Frequency Response of the Current Loop Transfer Function in Equation (24)

Speed Controller Design

In order to design the speed controller, Equations (36) and (37) were used with K_v=2.79 and T_v=0.04s. Figure 7(a) shows the step response of the exact speed loop transfer function described in Equation (38). The exact speed loop contains the current loop in the system transfer function. The speed loop was given a maximum speed command of 10 V and the result was the maximum speed of 261 rad/s. A soft-start circuit was inserted between the reference command and the SRM drive system in order to reduce the overshoot for the step response. The transfer function of the soft-start became. $S(s) = \frac{1}{1 + 0.04s}$ The magnitudes of the time constants for the soft-start and speed controller were same.

The step response of the speed loop transfer function with a soft-start is shown in Figure 7(b). The same condition applies in this simulation as the other step speed response. The overshoot was eliminated even though the rise time and settling time were increased to 0.055s and 0.14s, respectively. The step response had a rise time of 0.015s, 57% overshoot, and a 0.11s settling time.

The frequency response of the speed controller presents a bandwidth of approximately 15.9 Hz, as shown in Figure 8 (a). The bandwidth of the speed loop, shown in Figure 8(b), was reduced from 15.9 Hz to 6.37 Hz with a soft start. For many industrial applications, the response time is not as important as the speed overshoot of the drive. Therefore, a soft-start is a necessary part of an SRM speed drive.

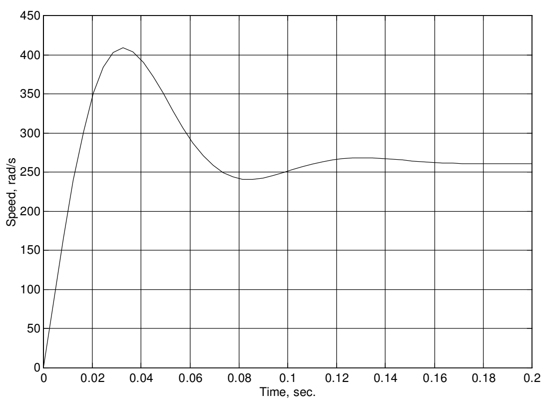

(a) Without Soft Start

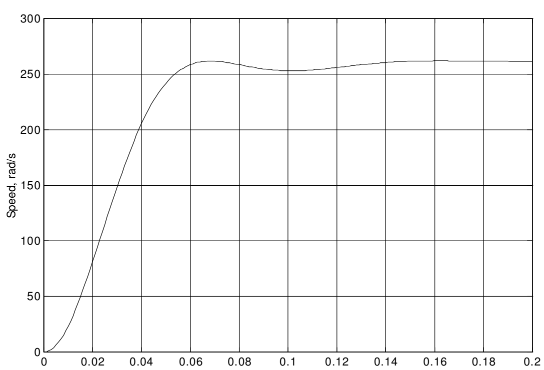

(b) With Soft Start

Figure 7. Step Response of the Speed Loop Transfer Function in Equation (38)

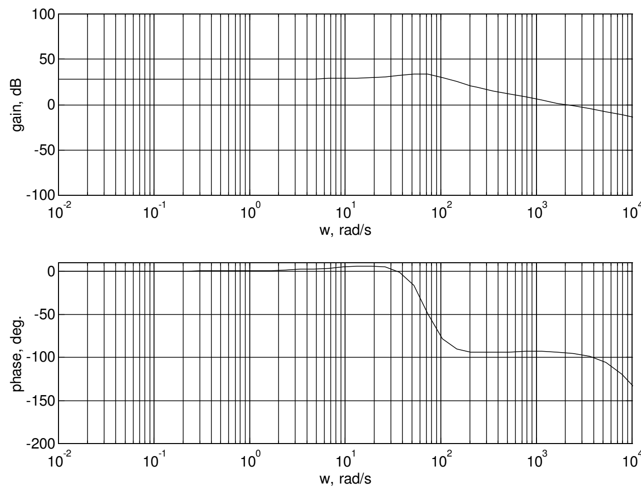

(a) Without Soft Start

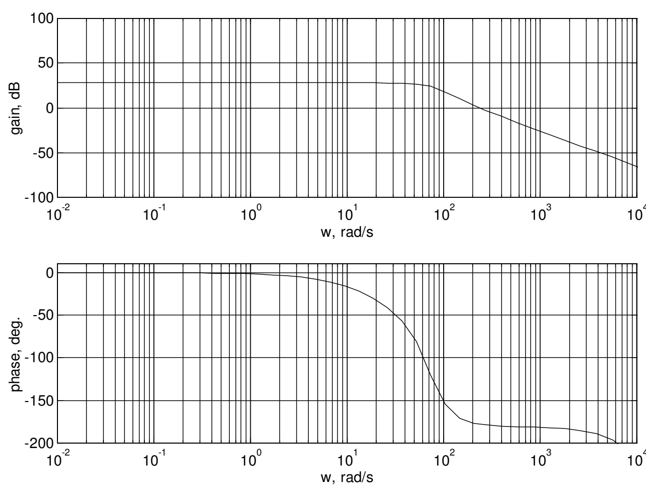

(b) With Soft Start

Figure 8. Frequency Response of the Speed Loop Transfer Function in Equation (38)

Experimental Verification

To verify the controller architecture and design methodology, a prototype controller was built. Verification covers the two control blocks: current control and speed control. Through verifying these types of control, it can be shown that the proposed architecture meets performance levels necessary for general-purpose drives.

Current Control Verification

The current control loop was implemented using the analog PI controller. The gain for the current controller was 9.42, and the delay was 1.13×10^{-4}. The advance angle was 3^{o} and fall angle was 9^{o}. Figure 9 is the actual phase current at a commanded value of 10A, 400 Vdc link voltage, and a speed of 1000 r/min. In the figure, each vertical division equals 2.5A of current.

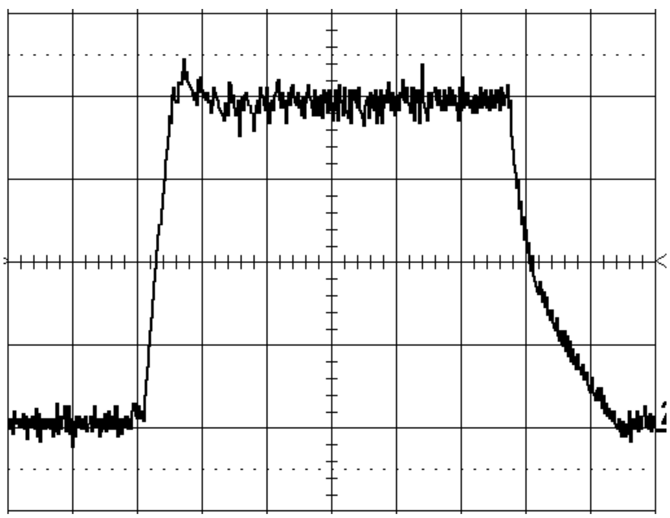

Figure 9. Actual Phase Current at 1000 r/min (Horizontal: 0.5ms/div, Vertical: 2.5A/div)

The rise time was approximately 0.15 ms and the fall time was approximately 0.85 ms. The errors between the actual performance and simulation may be attributed to deviations in the assumed phase inductances.

Speed Control Verification

The gain for the speed controller was 8.39, and the delay was 0.04. In Figure 10, the actual results of the step speed command on the prototype 5 hp SRM is shown. For the figure, each vertical division equals 500 r/min. The rise time for the actual speed was 0.3s and the percent overshoot was 10%. The reasons for the deviations are as follows. First, the current loop was not simulated in the speed simulation. The commanded value of current was assumed to be the actual current. Second, the problem with the small torque produced near alignment was not simulated. This problem reduces the torque generated in the regenerative quadrants.

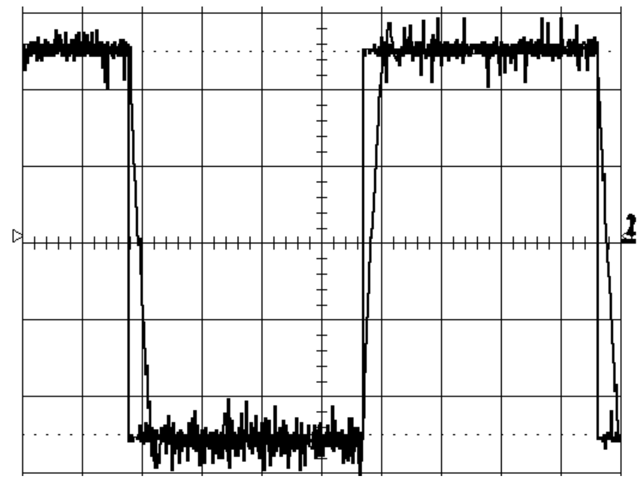

Figure 10. Actual Response to a Bi-Directional 1250 r/min Step Speed Command (Horizontal: 1 sec/div, Vertical: 500 r/min)

Conclusions

In this study, a design methodology for current and speed controller design of variable speed SRM drives, based on the linearized small-signal model, was developed, simulated, and experimentally verified. The unique methodology was simple and adequate for general-purpose applications. Through experimental tests, the controller proved its ability to meet general-purpose standards. The developed SRM controller demonstrated its ability to provide four-quadrant operation and complies with industrial standard inputs.

References

[1] Krishnan, R. (2001). *Switched Reluctance Motor Drives*. CRC Press.

[2] Reinert, J., Enslin, J. H. R., & Smith, E. D. (1993). Digital Control and Optimization of a Rolling Rotor Switched Reluctance Machine. *IEEE-IAS Conference Record*, 130-136.

[3] Inderka, R. B., Menne, M., & De Doncker, W. A. A. (2002). Control of Switched Reluctance Drives for Electric Vehicle Applications. *IEEE Trans. Industrial Electronics*, *49*(1), 48-53.

[4] Rahman. K. M., & Schulz, S. E. (2002). High-Performance Fully Digital Switched Reluctance Motor Controller for Vehicle Propulsion. *IEEE Trans. Industrial Electronics*, *38*(4), 1062-1071.

[5] Islam, M. S., Anwar, M. N., & Husain, I. (2003). Design and Control of Switched Reluctance Motors for Wide-Speed-Range Applications. *IEE Proceedings-Electric Power Applications*, *150*(4), 425-430.

[6] Schulz, S. E., & Rahman, K. M. (2003). High-Performance Digital PI Current Regulator for EV Switched Reluctance Motor Drives. *IEEE Trans. Industry Applications*, *39*(4), 1118-1126.

[7] Lin, Z., Reay, D., Williams, B., & He, X. (2010) High-Performance Current Control for Switched Reluctance Motors Based On On-Line Estimated Parameters. *IET Electric Power Applications*, *4*(1), 67-74.

[8] Wang, S-C., & Liu, Y-H. (2011). A Modified PI-Like Fuzzy Logic Controller for Switched Reluctance Motor Drives. *IEEE Trans. Industrial Electronics*, *58*(5), 1812-1825.

[9] Ilic'-Spong, M., Marino, R., Peresada, S. M., & Taylor, D. G. (1987). Feedback Linearization Control of a Switched Reluctance Motor. *IEEE Trans. on Automatic Control*, AC-*32*(5), 371-379.

[10] Kim, K-H., Jeung, Y-C., Lee, D-C., & Kim, H-G. (2012). LVERT Scheme of PMSG Wind Power Systems Based on Feedback Linearization. *IEEE Trans. Power Electronics*, *27*(5), 2376-2384.

[11] Yang, H., Panda, S. K., & Liang, Y. C. (1996) Experimental Investigation of Feedback Linearization Controller for Switched Reluctance Motor. *IEEE-PESC, Conf. Record*, 1804 - 1810.

[12] Xia, C., Geng, Q., Gu, X., Shi, T., & Song, Z. (2012). Input-Output Feedback Linearization and Speed Control of a Surface Permanent-Magnet Synchronous wind Generator with the Boost-Chopper Converter. *IEEE Trans. Industrial Electronics*, *59*(9), 3489-3500.

[13] Shi, C., & Cheok, A. D. (2002). Performance Comparison of Fused Soft Control/Hard Observer Type controller with Hard Control/Hard Observer Type Controller for Switched Reluctance Motors. *IEEE Trans. Systems, Man, and Cybernetics – Pt. C: App. and Reviews*, *32*(2), 99-112.

[14] McCann, R. A., Islam, M. S., & Husain, I. (2001). Application of a Sliding-Mode Observer for Position and Speed Estimation in Switched Reluctance Motor Drives. *IEEE Industry Applications*, *37*(1), 51-58.

[15] Krishnan, R. (2001). *Electric Motor Drives: Modeling, Analysis, and Control*. Prentice Hall.

[16] Vijayakumar, K., Karthikeyan, R., Paramasivam, S., Arumugam, R., & Srinivas, K. N. (2008). Switched Reluctance Motor modeling, Design, Simulation, and Analysis. *IEEE Trans. Magnetics*, *44*(12), 4605-4617.

[17] Hossain, I., & Hossain, S. A. (2005) Modeling, Simulation, and Control of Switched Reluctance Motor Drives. *IEEE Trans. Industrial Electronics*, *52*(6), 1625-1634.

[18] Roux, C., & Morcos, M. M. (2002). On the Use of a Simplified Model for Switched Reluctance Motors. *IEEE Trans. Energy Conversion*, *17*(3), 400-405.

[19] Baoming, G., Xiangheung, W., Pengsheng, S., & Jinping, J. (2002) Nonlinear Internal-Model Control for Switched Reluctance Drives. *IEEE Trans. Power Electronics*, *17*(3), 379-388.

[20] Essah, D. N., & Sudhoff, S. D. (2003). An Improved Analytical Model for the Switched Reluctance Motor. *IEEE Trans. Energy Conversion*, *18*(3), 349-356.

[21] Umland, J. W., & Safiuddin, M. (1990). Magnitude and Symmetric Optimum Criterion for the Design of Linear Control Systems: What Is It and How Does It Compare with the Others? *IEEE Trans. Industry Applications*, *26*(3), 489-497.

Biography

SHIYOUNG LEE is an Associate Professor of Electrical Engineering Technology at The Pennsylvania State University, Berks Campus, Reading, PA. He earned his B.S. and M.S. degrees from Inha University, Inchon, Korea, MSEE degree from Stevens Institute of Technology. Hoboken, NJ, and Ph.D. degree from Virginia Polytechnic Institute and State University, Blacksburg, VA. His primary research interest is the development of software configurable and full digital controllers for various electric motor drives. Other research interests include, but are not limited to the following topics: efficient power converter topologies, wireless power transmission, input power factor correction, LED lighting, alternative energy production, such as solar and wind power generation, and digital power processing for numerous industrial, medical and defense applications. He is a Senior Member of IEEE and member of ASEE, KIEE, and IAJC. He can be reached at sul28@psu.edu.

ULTRASONIC CHARACTERIZATION OF CYLINDRICAL SPECIMENS OF CONCRETE AND ROCK USING COMPRESSION WAVES

Nick Hudyma, University of North Florida; Faris A. Malhas, Central Connecticut State University

Abstract

Ultrasonic compression waves have been used to characterize laboratory specimens of concrete and rock for over seventy-five years. Although this technique may seem antiquated, advances in data collection and processing have let it remain relevant to both practitioners and researchers. Depending on both the sensor configuration and the type of data collected, ultrasonic characterization can provide a qualitative assessment of specimen properties, a quantitative assessment of elastic properties and damping, or an image of the internal structure of the specimen. This paper discusses four ultrasonic characterization techniques using compression waves applied to cylindrical specimens: a first arrival technique along the length of a specimen, a free-free resonant column test, a first arrival technique along the circumference of a specimen, and computed tomography.

The first arrival technique conducted along the axial dimension of a specimen can be used to provide a qualitative assessment of specimen properties. Free-free resonant column testing, which is also conducted axially along a specimen, uses both time domain and frequency domain analyses, and provides quantitative measures of dynamic elastic modulus, Poisson's ratio, and damping characteristics. The first arrival technique conducted along the specimen circumference can be used to assess variations in specimen properties along the axial direction. Computed tomography, which uses an array of compression wave transducers placed along the specimen circumference, is used to develop images of the internal structure of specimens. Examples of data generated using the four ultrasonic characterization techniques are provided.

Introduction

Ultrasonic characterization is a common tool employed by geotechnical and structural engineers to perform both qualitative and quantitative assessment on cylindrical concrete and rock specimens. Ultrasonic characterization is used either as an alternative to destructive testing, or to augment destructive testing. Destructive testing of both concrete and rock to determine strength and elastic parameters, such as elastic modulus and Poisson's Ratio, is both expensive and time consuming. A laboratory must have a strain-controlled load frame with the proper instrumentation and also an adequate capacity for testing the specimens. Prior to testing, the specimens must be properly prepared, which requires both specialized equipment and preparation time. In addition to the expensive and specialized equipment, a laboratory needs to have trained engineers or technicians, to operate and to calibrate the equipment. Because of these issues, some engineers prefer to employ ultrasonic methods as an alternative to destructive testing. Ultrasonic testing can be used to estimate strength, and to determine the dynamic elastic parameters of elastic modulus and Poisson's ratio.

However, many practitioners and researchers prefer to incorporate ultrasonic characterization as part of a larger testing program. The ultrasonic data is used to augment data collected from destructive testing. In this situation, ultrasonic characterization is considered a pre-test characterization technique. Knowing the dynamic properties or internal structure of a specimen prior to destructive testing may provide clues to anomalous results from destructive testing.

Brief History of Ultrasonic Characterization of Concrete and Rock

Ultrasonic characterization of concrete predates the characterization of rock. In 1938, Powers employed an early type of resonant frequency test to establish the elastic modulus of prismatic concrete specimens. The specimens were struck with a hammer, and the resulting natural frequencies of the specimens were compared to tones of calibrated steel bars. Beginning in the mid-1940s, ultrasonic testing was conducted on in-place concrete to determine the extent of cracking [1]. In 1949, the first use of longitudinal waves, with full wave form capturing to investigate the elastic properties of cylindrical specimens, was first documented by Hughes, et al. [2]. In this seminal work, it was demonstrated that the first arrival of pulsed longitudinal waves is a dilatational wave, which is better known as a P-wave or a compression wave. In the early 1950s, attempts were made to correlate pulse velocity with concrete strength in laboratory prepared specimens [1].

Beginning in the 1950s and 1960s, early experimentalists in the field of rock physics were attempting to understand how lithology, porosity, confining stress, pore pressure, pore fluid composition, degree of saturation, anisotropy, degree of fracturing, temperature, and ultrasonic wave frequency influenced the velocity and attenuation of P-waves and S-waves in sedimentary rock [3]. This work was performed for the oil industry. During this time, ultrasonic characterization systems were becoming commercially available, and the first arrival technique was commonly employed [3]. One of the earliest geotechnical studies using ultrasonic characterization dates from 1965 [4].

This paper describes ultrasonic techniques that are used to characterize cylindrical specimens. This specimen shape is convenient, since rock specimens are prepared from drill core samples, and concrete specimens are either cored from concrete structures, or prepared in the laboratory. Such specimens have specimen lengths twice that of the specimen diameter. To augment the discussion on the ultrasonic characterization techniques, data from a number of studies is presented as part of this paper.

Characterization Along the Specimen Axial Length

The most common approach for determining the ultrasonic characterization of cylindrical specimens is to evaluate the sample along its axial length. The input compression wave is introduced at one end of the specimen, and the output response is received at the other. In this technique the compression wave travels along the specimen's axial length. The majority of current studies in ultrasonic rock characterization utilize first arrival techniques along the long axis of specimens. The first arrival technique simply refers to detecting the arrival of the compression wave, and not to recording the full waveform. However, more sophisticated techniques are available which provide additional information about specimens.

The next sections will discuss both the first arrival technique and the Free-Free Resonant Column (FFRC) test. The first arrival technique is often referred to as a UPV (Ultrasonic Pulse Velocity) test or a PUNDIT (Portable Ultrasonic Nondestructive Digital Indicating Tester) test in the field of structural/materials engineering. The Free-Free Resonant column test incorporates full waveform capturing and analyses, in both the time and frequency domains. To augment the discussion, data from weathered limestone ultrasonic characterization studies will be used as an example of how the two tests can be used.

First Arrival Technique

The first arrival ultrasonic characterization technique is the measurement of compression wave propagation time through a specimen of known length. The experimental setup for this technique is shown in Figure 1. Two transducers, a transmitter (Tx) and a receiver (Rx), are used. An ultrasonic stress wave is sent from the TX, and the first arrival of the transmitted wave is detected by the RX. The TX and RX are coupled to the specimen using a coupling gel (usually vacuum grease). Typically, the TX and RX are held by hand against the ends of the specimen, but some studies have used specially designed coupling mechanisms to seat the pair against the specimen [5]. The travel time of the wave is determined empirically.

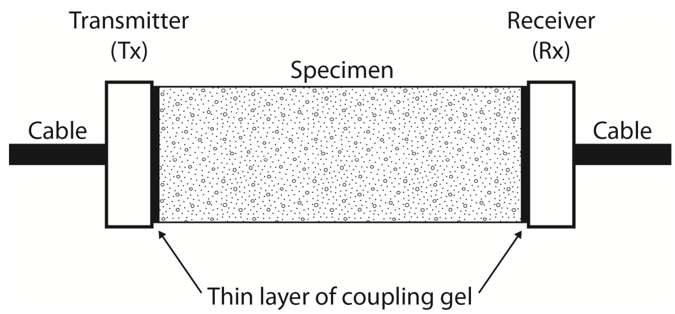

Figure 1. Schematic Setup of a PUNDIT Test

These transducers are available in a number of different frequencies, depending on the application. Typically, 54 kHz P-wave transducers are used in rock characterization studies. Commercially available systems have a large number of sensors available, ranging from 24 kHz to 1 MHz. Additionally, shear wave transducers are available. In some commercial systems, full waveforms are captured as part of the testing. This test is conducted in accordance to ASTM C597 [6].

The purpose of this test is to determine the longitudinal propagation velocity (V) of a compression wave through a specimen, which represents an average longitudinal wave velocity. Since the length of the specimen (L) is known, and the travel time (Δt) of the wave is determined by the apparatus, the longitudinal wave velocity can be computed using Equation 1.

$$V = \frac{\Delta t}{L} \tag{1}$$

Longitudinal wave velocity is used in the characterization of both concrete and rock, to estimate various physical and mechanical properties, as well as material states. For concrete applications, longitudinal wave velocity can be used to estimate concrete strength and modulus, as well as to estimate internal structural properties, such as homogeneity, hydration, and quality [6]. For rock characterization, longitudinal velocity has been used to estimate strength, stiffness, porosity, moisture content, slake durability, and Schmidt hardness [7-11]. This technique is also used to estimate the internal structural characteristics of rock, including discontinuities [11] and weathering [12].

The longitudinal wave sent through the specimen is an elastic wave. The velocity of an elastic wave through an elastic solid is a function of the dynamic elastic modulus (E_d), dynamic Poisson's ratio (ν_d), and material density (ρ). Equation 2 shows the relationship between wave velocity, elastic constants, and material density.

$$V = \sqrt{\frac{KE_d}{\rho}} \tag{2}$$

where,

$$K = \frac{(1-\nu_d)}{(1+\nu_d)(1-2\nu_d)}$$

The dynamic elastic modulus is an important parameter, because it can be related to the static elastic modulus. Since the longitudinal wave velocity is a function of dynamic elastic modulus (E_d), many practitioners and researchers believe the dynamic elastic modulus can be determined using the first arrival technique from the ultrasonic pulse velocity test. This assumption is based on the notion that Poisson's ratio has a very limited range of values. However, this is not a recommended practice for determining the dynamic elastic modulus [6].

Limitations of the First Arrival Technique

While the first arrival technique provides valuable results when measuring the travel time of an ultrasonic pulse during specimen characterization, it has limitations. The process does not yield absolute results. The wave velocity can be used to *estimate* the dynamic elastic modulus, and the magnitude of the velocity can be *related to* a number of material states, including specimen homogeneity, strength, moisture content, and hydration. In essence, the first arrival technique only provides a qualitative description of essential material properties.

Free-Free Resonant Column Testing

To overcome the limitations of the first arrival technique, more advanced techniques have been developed. One such technique is the free-free resonant column test, which can be used not only to determine the longitudinal wave velocity, but also to calculate the dynamic elastic modulus, dynamic Poisson's Ratio, and specimen damping.

Free-free resonant column (FFRC) testing (see Figure 2) involves impacting a freely suspended cylindrical specimen, and measuring the response. This type of testing also has been referred to as impact resonance (IR) testing [13], modal testing [14], or modal analysis [14]. Energy is input into one end of the specimen using a small duration impact from an instrumented hammer. The impact energy is received by a miniature accelerometer on the other end of the specimen. The accelerometer is attached to the rock specimen using either wax or hot glue. The accelerometer's mass must be small to minimize its effect on the dynamic properties of the specimen. The time history response for both the hammer and the accelerometer are recorded simultaneously by a high-speed data acquisition system, which also acts as a dynamic signal analyzer for transforming the captured full waveforms from the time domain into the frequency domain.

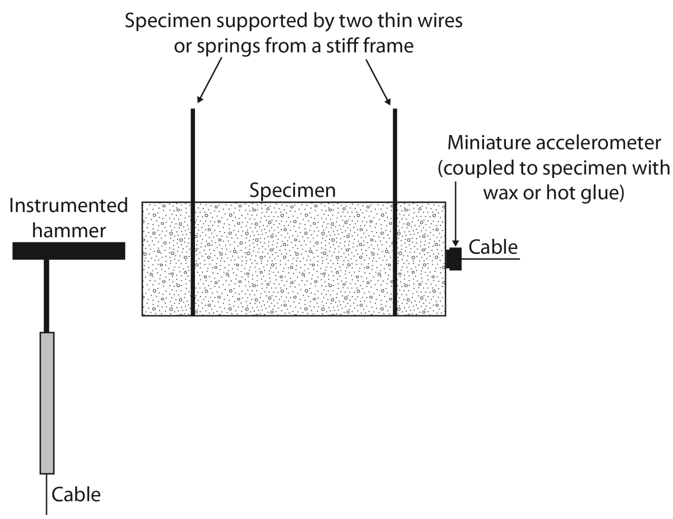

Figure 2. Schematic Setup of a Free-Free Resonant Column Test

Time Domain Analysis

The instrumented hammer's impact on the specimen triggers the system to record the respective responses. The impulse of the hammer and the response of the particle, as captured by the accelerometer due to the hammer's impact, are traced as a function of time, with resolution dictated by the sampling rate. These two responses are captured in the time domain. Figure 3 shows an example of a hammer impulse and an accelerometer response.

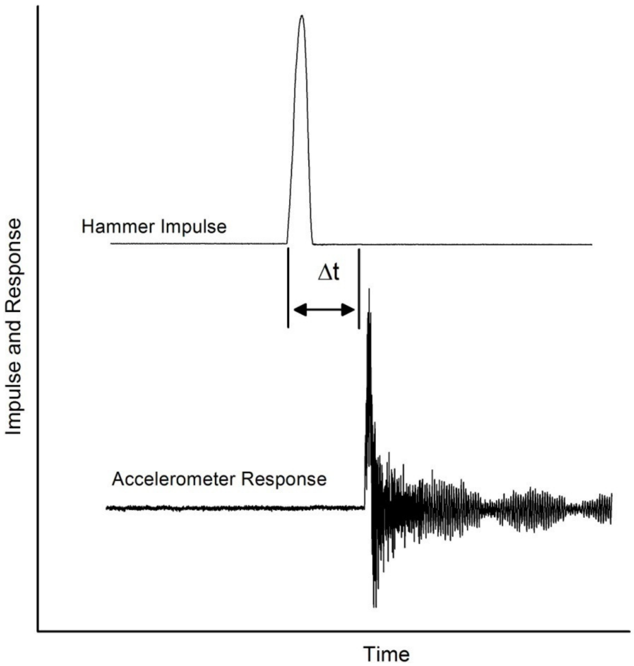

Figure 3. Hammer Impulse and Accelerometer Response from Free-Free Resonant Column Testing

From the time domain plots, it is possible to determine the travel time (Dt) of the elastic wave through the specimen. Knowing the length of the specimen (L), the constrained compression wave velocity can be computed using Equation 3. The result is assumed to be the constrained velocity, because particle motion along the centerline of a short specimen is sufficiently confined to prevent the generation of lateral motion [15]. Using the constrained compression wave velocity (V_P), and the mass density (ρ) of the specimen, the constrained elastic modulus, M, can be determined using Equation 4.

$$V_P = \frac{L}{\Delta t} \tag{3}$$

$$M = \rho V_P \tag{4}$$

Frequency Domain Analysis

In order to transform the time domain waveforms into the frequency domain, a fast Fourier transform (FFT) is used. Once the signals have been transferred to the frequency domain, a frequency response function (FRF) is computed. In the frequency domain, FRF is defined as the ratio of the output motion to the input force that caused that output response [16]. The FRF, using both magnitude and phase information, provides the relationship of a specimen's acceleration response per unit excitation force (see Figure 4). It describes the response level relative to the input, as a complex valued function of frequency [17].

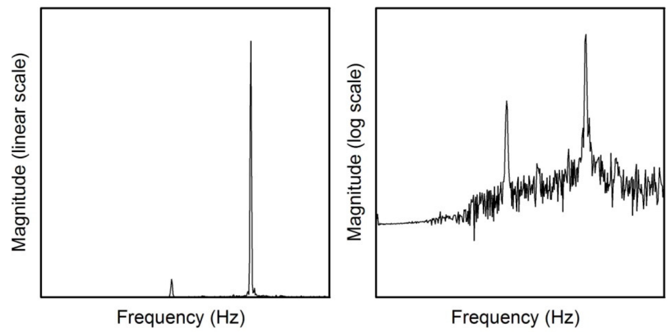

Figure 4. Example of the Frequency Response Function for a Cylindrical Aluminum Specimen [18]

Within the frequency response function, there are a number of clearly defined peaks. The peaks represent the natural frequencies of the specimen. The natural frequency with the greatest amplitude is the resonant frequency (f_n). Using both the resonant frequency and the specimen length (L), the unconstrained compression wave velocity can be computed using Equation 5. The dynamic Young's modulus (E_d) and the dynamic Poisson's ratio (ν_d) can be written in terms of the unconstrained compression wave velocity (V_c) and the specimen mass density (ρ) using Equations 6 and 7, respectively.

$$V_c = 2 f_n L \tag{5}$$

$$E_d = V_c^2 \rho \tag{6}$$

$$\nu_d = \frac{0.25\left[V_c^2 - V_P^2 + \sqrt{V_c^4 - 10V_c^2V_P^2 + 9V_P^4}\right]}{10V_P^2} \tag{7}$$

Another important parameter that can be obtained from free-free resonant column testing is the damping of the specimen. Damping is the result of a material property that causes free vibrations, within a specimen, to decrease in amplitude as a function of time [19]. Typically, damping is computed using the half power method, which is a geometrical shape function applied to the resonant frequency in the FRF. Damping can be computed using the resonant frequency (f_n) and the frequencies (f_1) and (f_2) [15] using Equation 8. Damping has been used for a number of studies, including the weathering and deterioration of concrete specimens [19], and the weathering of limestone specimens [18].

$$D = \frac{f_1 - f_2}{2f_n} \quad (8)$$

where,
f_1 and f_2 are frequencies computed at $\frac{1}{\sqrt{2}}A_{\max}$ and A_{max} is the amplitude at the natural frequency.

As part of FFRC testing, it is desirable to determine the quality of the response measurements. The coherence function, which is a measure of that portion of the output signal caused by the input impulse, is used to assess the quality of the response measurements. The coherence function, which is measured linearly and varies from zero to one, is represented by a function comprised of individual data points that contain information gathered from the input and output signals simultaneously. Each data point can be directly correlated to the position of that same data point on the FRF [20].

When a sufficient impact produces a vibration response that is perfectly correlated to the impact, the coherence graph will plot near 1.0 over the entire frequency range. Conversely, if a coherence graph drops below 1.0, it is likely that the hammer is not exiting the entire frequency range, or that noise is present as another source of vibration. Also, it is possible that residual motion from the first impact did not fully settle before applying a successive impact [20]. An example of a coherence function with an associated frequency response function is shown in Figure 5.

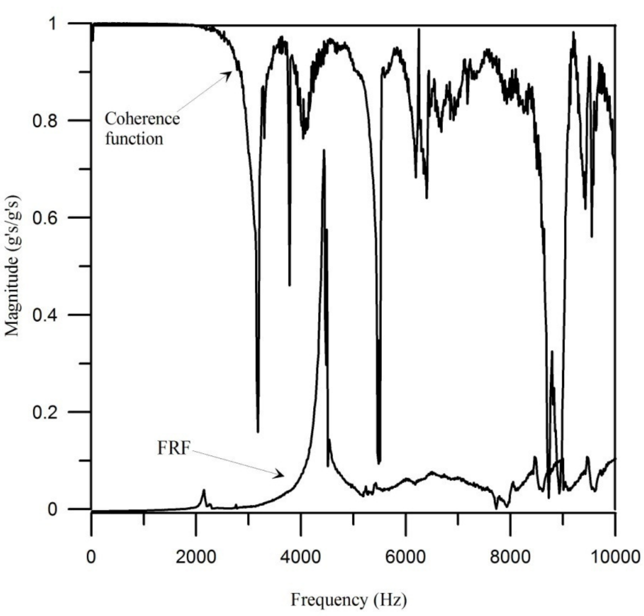

Figure 5. Coherence and Frequency Response Functions for a Cylindrical Aluminum Specimen [18]

Comparison of First Arrival and Free-Free Resonant Column Data

In a practical application of these techniques, both first arrival testing (using a PUNDIT system) and free-free resonant column testing were used to characterize Florida limestone specimens. The cores were obtained from a geophysical/ground truthing test site, located outside of Newberry, Florida, on State Road 26, in Alachua County. The site is approximately 29 kilometers west of Gainesville, and approximately 150 kilometers southwest of Jacksonville, Florida. The PQ sized cores (83 mm diameter) were obtained through double barrel wireline drilling into the Ocala Limestone formation [12]. Ocala Limestone consists of nearly pure limestone and dolostones, and is from the upper Eocene age. The top of the limestone is extremely variable, due to karstification caused by weathering and erosion [21].

The first arrival technique used a James Instruments ultrasonic pulse velocity system, which transmitted ultrasonic pulses at a 10 Hz rate, using 54 kHz transducers. The transducers were coupled to the specimen ends using vacuum grease. Alternatively, the free-free resonant column technique used a miniature accelerometer (PCB model 353B15), an instrumented hammer (PCB model 086C03), and an IOtech four-channel dynamic signal analyzer with eZ-Analyst software. The accelerometer was attached to the specimens using hot glue.

A total of twenty-two specimens were tested. The longitudinal wave velocities ranged between 1313.3 and 3369.8 m/s. The average longitudinal wave velocity was 2097.2 m/s, and the coefficient of variation was 24.4%. The unconstrained compression wave velocities (V_c from FFRC testing) ranged between 618.5 and 3215.6 m/s. The average unconstrained compression wave velocity was 1636.7 m/s, and the coefficient of variation was 41.1%. The two velocities are plotted in Figure 6.

For all but one specimen, the longitudinal wave velocities from first arrival (PUNDIT) testing are higher than the unconstrained velocity from free-free resonant column testing. These results are similar to that of Cha and Cho [22]. It is important to note that the two velocities are not the same; the first arrival (PUNDIT) test provides the longitudinal wave velocity, whereas the free-free resonant column test provides the unconstrained velocity. Care must be taken when computing the dynamic elastic modulus (E_d) from dynamic tests; the wave velocities presented in Equation 2 and Equation 6 are not interchangeable.

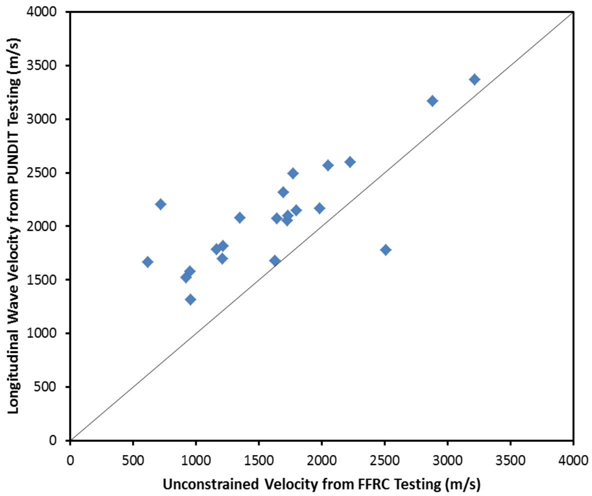

Figure 6. Comparison of Longitudinal Wave Velocity and Unconstrained Velocity

Advantages of the Free-Free Resonant Column Test

The more sophisticated free-free resonant column test provides much more information regarding the dynamic properties of the specimen. Like the first arrival technique, the free-free resonant column test provides the longitudinal wave velocity from the time domain analysis. However, when the time domain data is transformed into the frequency domain, the unconstrained compression wave velocity can be computed. Knowing the longitudinal wave velocity and the unconstrained compression wave velocity, the dynamic elastic modulus and Poisson's ratio can be computed. It is the quantification of these elastic parameters that make the free-free resonant column test very desirable.

In addition to the elastic parameters, the resonant frequency and damping of the specimen can be computed. These two parameters can be qualitatively related to various specimen properties. Additionally, the coherence function provides a quality check on the signal transmitted through the specimen. However, the free-free resonant column test does have one drawback. Moving from the relatively straightforward first arrival technique to the free-free resonant column technique requires much more sophisticated equipment and software/analyses.

Characterization Along the Specimen Circumference

Characterization along the axial dimension of a cylindrical specimen, using either first arrival or free-free resonant column testing, only provides an average wave velocity and dynamic elastic properties along the axial length. It is conceivable that within a single specimen there may be zones of varying material quality, but a single specimen measurement along the axial dimension cannot delineate such features. If ultrasonic characterization is conducted along the circumference of a cylindrical specimen, zones of varying quality can be detected.

Ultrasonic characterization along the circumference of a specimen is much less common than characterization along the axial dimension. Although the two techniques are similar, i.e. either the first arrival or full waveforms are measured, the experimental constraints and equipment requirements are different. The predominant experimental constraint is that of precise transducer location. The predominant equipment requirements are transducer size and frequency.

Single Transmitter/Receiver Pair

The input compression wave is introduced by the transmitter at one side of the specimen and is received by the receiver, which is situated diametrically opposite to the transmitter. The transmitter and receiver must be at the same height. It is important that the transmitter and receiver locations are known precisely, because the compression wave velocity is a function of the distance travelled. The diameter of the ultrasonic transducers must be small enough to be fully coupled to the specimen surface, to ensure sufficient signal quality. As the specimen diameter increases, the transducer diameter can increase also. Figure 7 shows a typical setup for a single transmitter and receiver pair used in circumferential characterization.

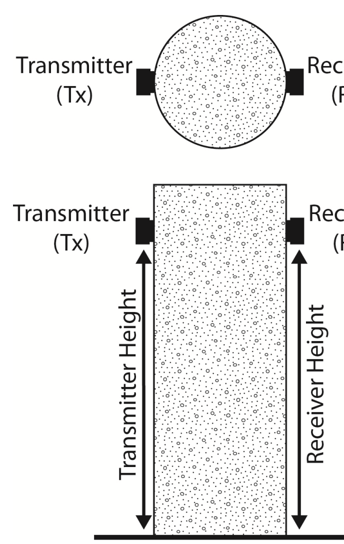

Figure 7. Typical Setup of a Single Transmitter and Receiver Pair

The use of a single transmitter/receiver pair allows for specimen characterization in two, typically orthogonal directions. The transmitter/receiver pair can be moved along the long axis of the specimen to determine changes in compression wave velocity across the specimen's diameter, as a function of specimen length. Figure 8 shows orthogonal compression velocity data using a first arrival technique across a plaster of Paris specimen. The difference in the velocity measurements indicates there is compression wave anisotropy within the specimen.

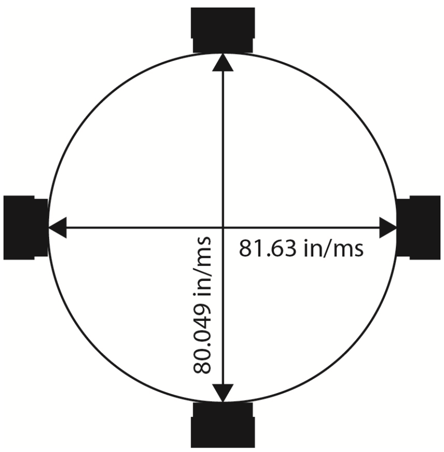

Figure 8. Results from compression wave velocity measurements cross orthogonal axes of plaster of Paris

Computed Tomography

Ultrasonic compression wave characterization of specimens along the sample's circumference is time consuming and tedious. For these reasons, researchers often do not conduct characterization using single transmitter/receiver pairs, but will utilize multiple transmitters/receivers in an array. These transducer arrays often are computer controlled, and each transducer can act both as a transmitter and as a receiver. The wave propagation data can be processed using tomographic principles to produce an image of the internal structure of a specimen.

Computed tomography (CT) is an imaging technique where cross-sectional images are reconstructed from two-dimensional energy wave projections through a body. CT is most often associated with X-ray energy use in medical imaging applications. However, any wave-based energy source can be used. The compressive wave velocity is a function of the material's elastic properties. If a body contains at least two materials with distinct elastic properties, it is possible to detect the velocity contrast. Ultrasonic computed tomography has been used to characterize cylindrical specimens of both concrete and rock [23–26].

Many different experimental configurations for conducting CT scans on cylindrical laboratory specimens are used. The theory behind CT is beyond the scope of this paper, but, in general, it is imperative to maximize the number of transducer and receiver locations across the specimen diameter; the greater the number of computed travel times through sections of a specimen, the more detailed the cross-sectional image. Multiple tomographic cross-sections are stacked together, and interpolation is performed between the cross-sections to create a volume. In the case of medical computed tomography, the distance between successive cross-sections is very small, and, as such, the quasi three-dimensional volume is quite detailed.

Computed Tomography Characterization Study

ACT study was conducted on 15.24 cm by 30.48 cm (6 x 12 inch) plaster of Paris specimens containing large Styrofoam® inclusions [25], [26]. The smallest inclusions were 2.54 cm (1 inch) diameter spheres. The authors referred to their tomographic technique as cross-specimen acoustic tomography (CSAT). A set of eight ultrasonic transducers (frequency of 1.26 kHz) were used to characterize the specimens. Each of the eight transducers was able to act as both a transmitter and a receiver. The transducer configuration is shown in Figure 9. The eight transducers were spaced at forty-five degree increments around the specimen circumference. In the figure, the top graphic shows the straight-line ray path with a single transducer acting as a transmitter, and the remaining seven transducers acting as receivers. The second graphic shows all of the ray paths for each of the eight sensors acting as both a transmitter and as a receiver. To increase the ray path coverage, the set of eight transducers was rotated 22.5 degrees, and the process was repeated. The third graphic shows all ray paths used to develop a single tomographic cross-section. To completely characterize each of the plaster of Paris specimens, tomographic cross-sections were produced every 1.27 cm (0.5 inches) along the specimen length. It took approximately four hours of laboratory time to characterize a single specimen. The photograph in Figure 9 shows a plaster of Paris specimen with the transducers attached.

To produce the tomographic cross-sections, an initial velocity within the specimen is assumed. Then, a forward model for each of the straight line ray paths is calculated. Next, the model travel times are compared to the actual travel times to determine the model error. The error is used to update the velocity model, and the model travel times are recalculated. This iterative process is repeated until the overall error is minimized for the model. The commercially available computer code GeoTomCG, by GeoTom, LLC, was used to produce the tomographic cross-sections. An example of an interpreted tomographic cross-section is shown in Figure 10. The scale shown indicates velocities with units of inches per millisecond.

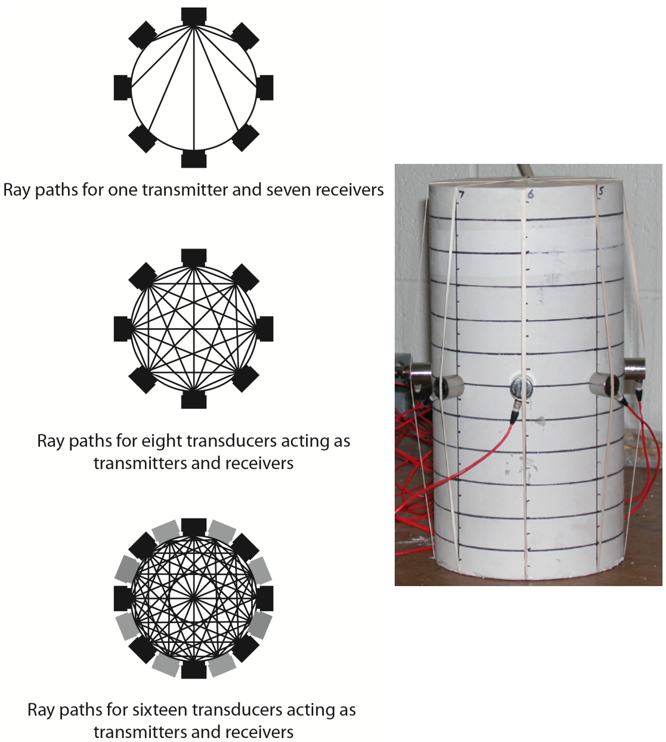

Figure 9. Ray Paths for Specimen Tomography and a Picture of the Specimen with Transducers Attached

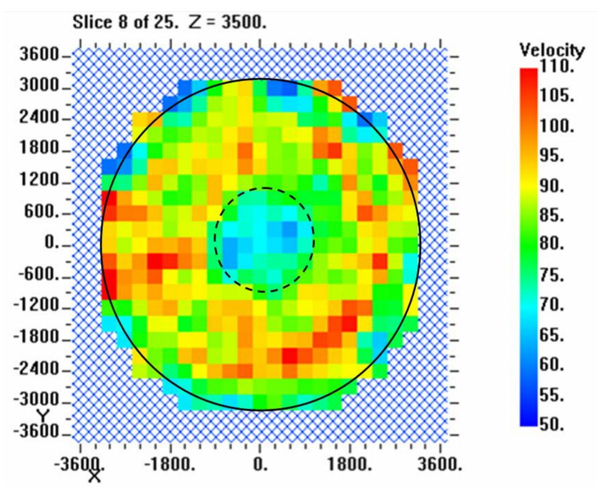

Figure 10. Tomographic Cross-Section of a Plaster-of-Paris Specimen (outlined with a solid line) with a Large Circular Styrofoam® Inclusion (dashed line). The Velocity Scale has Units of Inches per Millisecond.

The tomographic cross-section shows many different colored pixels. Each of the colors represents a wave velocity. To interpret the tomography cross-sections of plaster specimens containing Styrofoam inclusions, a solid plaster of Paris specimen was characterized to determine the range of velocities of the plaster. Based on the analysis, it was determined that velocities less than approximately 70 in/millisecond correspond to a Styrofoam® inclusion.

The twenty-five horizontal tomographic cross-sections were stacked together to form a volume for visualization. As the volume was formed, the two-dimensional pixels became three-dimensional voxels. In order to form the volume, the tomographic cross-sections were stacked with a vertical spacing of 1.27 cm (0.5 inches), and a linear interpolation scheme was applied between the cross-sections. The result was a cylindrical object that could be sectioned along any plane to view the internal Styrofoam® inclusions. Figure 11 is a section through a specimen that had two large Styrofoam® inclusions. The red colors represent plaster of Paris, and the yellow-to-green colors represent the Styrofoam® inclusions.

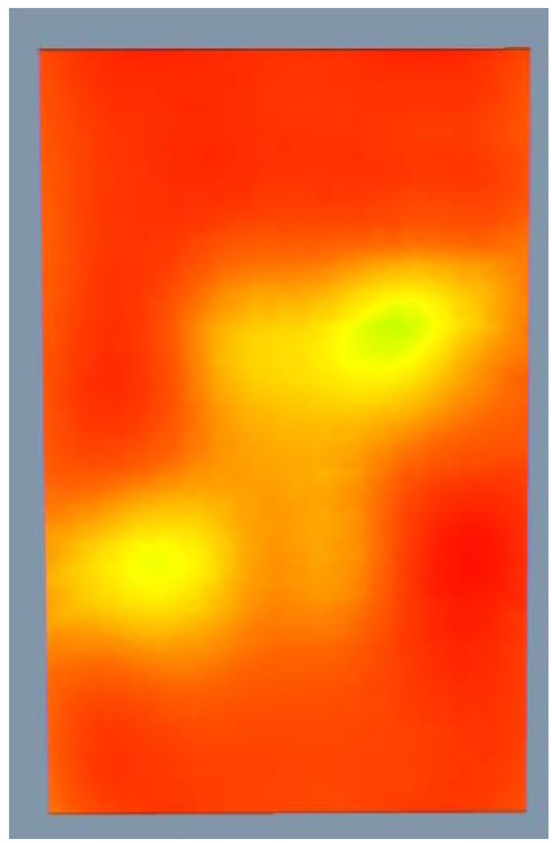

Figure 11. Results of the Tomographic Characterization of Plaster-of-Paris Specimens Containing Large Styrofoam® Inclusions

The ultrasonic tomographic characterization was able to successfully detect the presence and relative size of the Styrofoam® inclusions. However, the ultrasonic tomography was not able to delineate the shapes of the inclusions. A range of the total volume of the inclusions could be made, based on the assumed wave velocity through the Styrofoam [26].

Conclusions

Ultrasonic characterization using compression waves provides valuable information to engineers and researchers. Using various configurations of ultrasonic testing with compression waves, it is possible to provide information regarding specimen properties prior to destructive testing. As the ultrasonic characterization technique's sophistication increases, more valuable information is obtained. Using first arrival techniques, which were developed in the mid-1940s, qualitative assessment of a specimen's elastic modulus can be obtained. However, the first arrival technique provides the compression wave velocity, which can only provide estimates for concrete and rock specimen properties, such as strength and porosity. The more sophisticated free-free resonant column test, which analyzes data in both the time and frequency domains, provides a quantitative assessment of elastic modulus and Poisson's ratio. In addition, the free-free resonant column test provides compression wave velocity and material damping.

The first arrival technique and the free-free resonant column test are conducted along the axial length of cylindrical specimens. When compression waves are passed across a specimen diameter, it is possible to assess changes along the length of the specimen, and to determine the presence of compression wave velocity anisotropy. Using an array of transducers, which function as both transmitters and receivers, and then processing the data using tomography principles, it is possible to develop a cross-section image showing zones of wave velocities within a specimen. If multiple planes are characterized in this manner, it is possible to produce a detailed image of the internal structure of the entire specimen.

Acknowledgements

The work presented in this publication has been supported by funding from the National Science Foundation (Grant Number CMMI-0555812); the Florida Department of Transportation District 2; and the University of North Florida. Numerous faculty members and students have worked on the various topics presented within this paper. Notable contributors include Mary MacLaughlin and Curtis Link from Montana Tech of the University of Montana and students Ariel Sarno and Chris Sherman.

References

[1] Carino, N. J. (1994). Nondestructive Testing of Concrete: History and Challenges. In P. K. Mehta (Ed.), ACI SP-144 Concrete Technology – Past, Present and Future (pp. 623 – 678). Detroit, MI: ACI.

[2] Hughes, D. S., Pondrom, W. L., & Mims, R. L. (1949, May). Transmission of Elastic Pulses in Metal Rods. *Physical Review, 75*(10), 1552-1556.

[3] King, M. (2005, November). 75th Anniversary: Rock -Physics Developments in Seismic Exploration: A Personal 50-year Perspective. *Geophysics, 70*(6), 3ND-8ND, doi:10.1190/1.2107947

[4] D'Andrea, D. V., Fischer, R. L., & Fogelson, D. E. (1965). Prediction of Compressive Strength from Other Rock Properties (U. S. Department of Interior Report No. 6702) Washington, DC: Bureau of Mines

[5] Basu, A., & Aydin, A. (2006). Evaluation of Ultrasonic Testing in Rock Material Characterization. *ASTM Geotechnical Testing Journal, 29*(2), 117-125

[6] Naik, T. R., Malhotra, V. M., & Popovics, J. S. (2004). The Ultrasonic Pulse Velocity Methods. In V. M. Malhotra & N. J. Carino (Eds.), Handbook on Nondestructive Testing of Concrete (second edition, pp. 8-1 - 8-19). Boca Raton, FL: CRC Press.

[7] Kahraman, S. (2001). A Correlation between P-wave Velocity, Number of Joints and Schmidt Hammer Rebound Number. *International Journal of Rock Mechanics & Mining Sciences, 38*(5), 729-733.

[8] Yasar, E., & Erdogan, Y. (2004). Correlating sound velocity with the density, compressive strength and Young's modulus of carbonate rocks. *International Journal of Rock Mechanics and Mining Sciences, 41* (5), 871-875, doi:10.1016/j.ijrmms.2004.01.012

[9] Kahraman, S., & Yeken, T. (2008). Determination of physical properties of carbonate rocks from P-wave velocity. *Bull. Eng. Geol. Environ., 67*(2), 277-281, doi:10.1007/s10064-008-0139-0

[10] Khandelwal, M., & Ranjith, P. G. (2010, May). Correlating index properties of rocks with P-wave measurements. *Journal of Applied Geophysics, 71*(1), *1-5*, doi:10.1016/j.jappgeo.2010.01.007

[11] Yagiz, S. (2011, July). P-wave velocity test for assessment of geotechnical properties of some rock materials. *Bull. Mater. Sci. 34*(4), 947-953

[12] Hudyma, N., Hiltunen, D. R., & Samakur, C. (2007). Variability of karstic limestone quantified through compressional wave velocity measurements. *Problematic Soils and Rocks and In Situ Characterization, Geotechnical Special Publication (GSP) 162, Pro-*

ceedings of sessions from Geo-Denver 2007, (A. Puppala, N. Hudyma, and W. Likos, eds.) February 18-21, 2007, Denver, CO, ASCE Press.

[13] Lee, K.-M., Kim, D.-M., & Kim, J.-S. (1997). Determination of dynamic Young's modulus of concrete at early ages by impact resonance test. *KSCE Journal of Civil Engineering, 1*(1), 11-18.

[14] Avitabile, P. (2001). Back to basics. *Experimental Techniques. 25*(2), 11-12, doi:10.1111/j.1747-1567.2001.tb00010.x

[15] Jeon, S. Y. (2008). *Dynamic and cyclic properties in shear of tuff specimens from Yucca Mountain, Nevada*. Unpublished doctoral dissertation, University of Texas, Austin.

[16] He, J., & Fu, Z. F. (2001). *Modal Analysis*, Butterworth Heinemann, Boston.

[17] Richardson, M. H. (1999). Structural Dynamics Measurements. *Technical Report SD2000*. Vibrant Technology, Inc., Jamestown.

[18] Sarno, A. I. (2010). *Correlations of static, dynamic, and physical properties to the weathering state of Ocala limestone.* Unpublished Master's thesis, University of North Florida.

[19] Malhotra, V. M., & Sivasundaram, V. (2004). *Resonant frequency methods*. In V. M. Malhotra & N. J. Carino (Eds.), Handbook on nondestructive testing of concrete (second edition, pp. 7-1 – 7-21). Boca Raton, FL: CRC Press.

[20] Goldman, S. (1999). *Vibration Spectrum Analysis*. Industrial Press Inc., New York.

[21] Scott, T. M. (2001). *Text to accompany the geologic map of Florida.* (Florida Geological Survey Open File Report Number 80), Tallahassee, FL.

[22] Cha, M., & Cho, G. C. (2007, July) Compression wave velocity of cylindrical rock specimens: engineering modulus interpretation. *Japanese Journal of Applied Physics, 46*(7B), 4497-4499, doi:10.1143/JJAP.46.4497

[23] Diagle, M., Fratta, D., & Wang, L. B. (2005). Ultrasonic and X-ray imaging of highly contrasting inclusions in concrete specimens. *Proceedings of 2005 Geo-Frontiers Conference*, *Geotechnical Special Publication 138 Site Characterization and Modeling*. Austin, TX, http://dx.doi.org/10.1061/40785(164)40

[24] Martins, J. L., Soares, J. A., & da Silva, J. C. (2007). Ultrasonic travel-time tomography in core plugs. *Journal of Geophysics and Engineering, 4*, 117-127, http://dx.doi.org/10.1088/1742-2132/4/2/001

[25] Sarno, A., N., Hudyma, D. R., Hiltunen, & MacLaughlin, M. (2009, November). Modal Testing: An Innovative Approach to Dynamic Rock Specimen Characterization. *The Joint 14th Intermountain Conference on the Environment & 42nd Engineering Geology and Geotechnical Engineering Symposium.* (pp. 77-82).

[26] Hudyma, N., Johnson, K., Sherman, C., & MacLaughlin, M. (2010). Comparisons of 2D imaging techniques for internal macropore characterization, *Proceedings of the 44th US Rock Mechanics Symposium and 5th U.S.-Canada Rock Mechanics Symposium*, Paper Number ARMA 10-376, Salt Lake City, UT.

Biographies

NICK HUDYMA is a Professor of Civil Engineering at the University of North Florida. He earned his B.S. from the University of Manitoba (Geological Engineering), his M.S. (Civil and Environmental Engineering, 1994) from the University of Nevada Las Vegas, and his Ph.D. (Engineering, 1999) from the University of Nevada, Las Vegas. His interests are pre-test characterization of rock, including ultrasonics, laser scanning, and photogrammetry; laboratory characterization of soil and rock; and ground penetrating radar in infrastructure and geotechnical site characterization. Dr. Hudyma may be reached at nhudyma@unf.edu

FARIS MALHAS is Dean of the School of Engineering and Technology at Central Connecticut State University. He earned his B.S.E. and M.S.E. (Civil Engineering) from the University of Michigan, Ann Arbor, and his M.S. (Engineering Mechanics) and Ph.D. (Civil Engineering) from the University of Wisconsin, Madison. His research interest is in structural concrete. Dr. Malhas may be reached at fmalhas@ccsu.edu

RENEWABLE ENERGY WORKSHOPS FOR PROMOTING STEM EDUCATION IN RURAL SCHOOLS

Faruk Yildiz, Joe Muller, Doug Kingman, Doug Ullrich, Keith Coogler, William Crockford, Sam Houston State University

Abstract

Emphasis on Science, Technology, Engineering, and Math (STEM) education has become very important due to a lack of interest in STEM components, especially from female students. Government agencies, non-profit and profit organizations, academia, and foundations have been investing in this area to increase interest and retention rates for STEM fields. There have been many attempts using a variety of different methods to increase student interest in STEM fields. The renewable energy workshop series is a three-year project designed to increase K5-12 school students' interests in and desire to pursue STEM careers. Additionally, workshops were offered to science, math, and technology teachers to enable the program's curriculum to be transferred back to the students who were not present for the workshops. A team of faculty and students has been offering a series of educational workshops since 2010 to promote STEM education through applied Renewable Energy (RE) workshops in East Texas school districts. A mobile unit (an enclosed and retrofitted trailer) was used to solve transportation issues of the students for the rural school districts by taking all of the equipment directly to school districts instead of having students come to the college campus. In this paper, the author discusses workshop curricula, goals and objectives, demographics, participants, methods used, equipment and materials, the retrofitting process of the mobile unit, and survey results.

Introduction

According to Brian Kelly [1], STEM is

> …an acronym that represents the fields of science, technology, engineering and math. It's also shorthand for an important issue that is key to the U.S. economy, namely, the growing disconnect between the skills that employers need in an increasingly technological world and the talent—or lack thereof—that our education system produces. (p.1)

Kelly states that the gap between industry and skilled workers has been growing, particularly in the energy sector. This gap needs prompt attention in STEM fields because of a lack of STEM skilled workers. Kelly mentions that this problem must be solved in order to carry our nations' global competitiveness into the future.

STEM education takes a critical place on state and federal government agendas. The need for high-quality STEM education has been publicized in various reports that indicate that the nation's future economic success and security depends on a highly skilled STEM workforce [2-6]. Recent studies and statistics show that interest in STEM components has been dropping due to several reasons. These studies concluded that STEM education in the U.S. needs to be improved and K-12 (between 6th and 12th grade students) students' attention should be centered on this field. Feedback from students in the 5th and 6th grades suggests that they do not like science and math. According to the National Science Boards 2010 report, STEM fields are widely regarded as critical to the national economy. There is a growing concern about our young people's ability in order for the U.S. to maintain its competitive position in the global market place. This has prompted calls for the U.S. education system to produce more graduates with training and expertise in STEM fields. Academia, government agencies, and non-profit and profit organizations have been working to strengthen each component of STEM education throughout the states. These attempts have a common goal to increase the proficiency of all students in STEM and increase the number of students who pursue STEM careers and advanced studies [7-9]. According to Government Accountability Office statistics, there are billions of dollars being spent to encourage students to enter STEM fields. However, the percentage of U.S. undergraduates pursuing and earning STEM-related degrees has changed little during recent years [10-13].

One of the most recent studies was prepared by the Joint Economic Committee of United States Congress. The report was entitled "STEM Education: Preparing for the jobs of the future." The study, based on the demand for qualified STEM workers, projected an increase in numbers in the near future. "While it is difficult to project trends in the labor market, the demand for STEM-skilled workers is expected to continue to increase in the future, as both the number and proportion of STEM jobs are projected to grow" [14]. "New Bureau of Labor Statistics data show that employment in STEM occupations is expected to expand faster than employment in non-STEM occupations from 2010 to 2020 (by 17 versus 14 percent)" [15]. While the projected difference between the STEM and non-STEM employment growth rates does not appear to be particularly dramatic, this small difference is due in large part to the Great Recession and the severe job losses concentrated in non-STEM occupations. Figure 1 shows projected growth for STEM occupations [16].

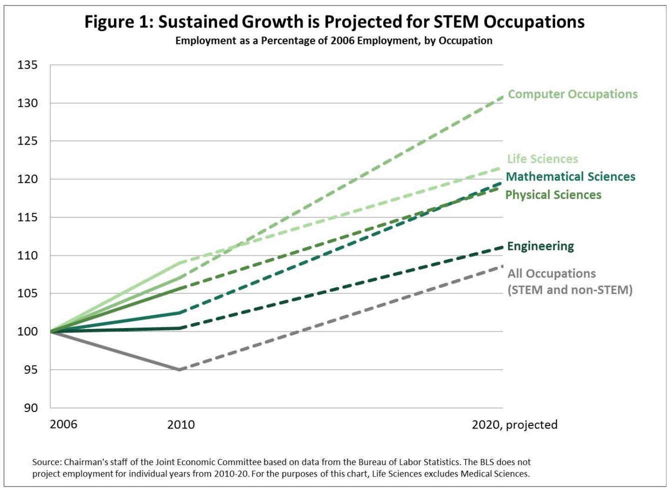

Figure 1. Sustained Growth Projections for Stem Occupations [16]

Various ways to attract young minds to STEM fields have been tried by non-profit organizations and institutions through volunteer work and funding. One of the programs funded by the Department of Education is the Upward Bound TRIO program. The Upward Bound Math-Science program is one of three types of programs funded under the Upward Bound program, one of seven outreach and student services programs under the TRIO umbrella. The other programs are a) educational opportunity centers, b) Ronald E. McNair post-baccalaureate achievement, c) student support services, d) talent search, e) training program for federal TRIO programs, and f) veterans Upward Bound [17], [18]. In 2012, 113 grants totaling more than $30.8 million were distributed to Upward Bound programs to strengthen students' math and science skills, and to prepare them for post-secondary education programs that lead to careers in STEM fields.

Other ways is to increase youth interest include science fairs and student competitions such as robotics and science Olympiads [19-23]. Students in middle school and high school have the opportunity to use their knowledge and skills of science at the Science Olympiad and other such competitions. Some of the institutions offer science fairs and science Olympiad competitions on their campuses and invite K-12 students and teachers. These science fairs and Olympiads are also used for student recruitment purposes. Science fairs are also offered by science and engineering programs at colleges and universities to demonstrate student abilities and institutional resources. Usually the target is the student rather than the teacher, but teachers use what they see at science fairs in their classes. For the teachers, there are summer science training programs offered at various levels funded by state/federal government or charitable foundations [24-26].

In addition to the variety of STEM education promotion activities explained above, another popular method is the use of mobile education. The main purpose of mobile education is to visit school districts, especially the ones in rural areas with limited transportation abilities. Each discipline may have a specific topic or topics for promoting STEM components. For example, one way is to teach GIS systems, an attractive tool for focusing youth attention on STEM. Another way is to teach ecology, weather education, and energy relations by having field studies with students [27-31]. Some units teach clean and renewable energy technologies to promote STEM. There are many ways to offer renewable energy workshops, demonstrations, and fairs to K-12 education systems and local communities [32-34]. A mobile unit (van or a trailer) is a unit for the demonstrations and workshops for the mobile education. In this current study, renewable energy projects were initially offered on campus as workshop training and then extended to school districts with a modified enclosed trailer. All of the findings from the workshops are summarized here.

Project Goals

Based on the results and experiences of the workshops offered at the college campus, the project team wanted to extend workshops to promote STEM education in rural school districts. Several school districts showed an interest in workshops, but due to issues in scheduling, budget, and transportation, workshops were not offered at school districts. The interest came mainly from school districts in rural areas in East Texas. It was difficult to transport and load/unload equipment and tools to rural area schools districts due to the lack of a specially designed mobile unit (van or trailer). A proposal to purchase and modify an enclosed trailer was presented to a local electric utility company for funding [35]. The proposal was funded to buy a 22' enclosed v-nose trailer that was modified for loading and mounting all equipment and tools for transportation anywhere in East Texas for further workshops. This way, more school districts could participate in workshops on their campuses and have the opportunity to receive applied hands-on renewable energy education with a specially designed Entergy vehicle.

One of the goals of the workshops was to engage young minds early and accelerate the progress of targeted students toward a sustainable world and offer opportunities for secondary and high school students not otherwise available. This would afford students the opportunity to prepare themselves as future engineers and scientists with a greater understanding of global issues and energy problems. Another goal was to promote interest in STEM fields by solving energy-related problems throughout the world by supporting teachers and helping them become more familiar with sustainable energy sources. This goal was supported through the use of a number of renewable energy based hands-on projects to promote mathematics and science for middle school teachers and students.

Mobile Renewable Energy Education (MREE) is a long-term project aimed at providing area (especially rural) K5-12 students and teachers with an applied mathematics, engineering, and science curriculum package based on Photovoltaic (PV), wind power, energy conversion and conservation, energy safety and awareness, human power, global warming, and hydrogen fuel-cell fundamentals. The MREE project has established a partnership between the university and selected area schools for the improvement of students' mathematical and scientific skill sets, and their technological literacy by creating an environment where they must understand and figure out relationships in basic mathematics, science, and engineering technology. The students can then apply their new-found skills to study renewable energy fields in order to manage their studies effectively. Students gain a professional skill set for successfully applying mathematics and science to technical projects with diverse teams throughout their careers. The use of a number of renewable energy and energy efficiency-based hands-on projects such as a nationwide solar electric project promotes mathematics and science for teachers and students.

Project Description

This MREE project was sponsored by the Entergy Charitable Foundation and Sam Houston State University. A partnership was established on Math-Science-Engineering-Technology in Texas on Applied Renewable Energy Areas between Sam Houston State University and area school districts. Renewable energy applications such as wind, solar, and hydrogen fuel-cell theory and applications were covered in the workshop curricula. The workshops were designed to attract students' interest in applied renewable energy areas. Projects were aimed at providing area school teachers and students with an applied mathematics and science curriculum package based on photovoltaic (PV) systems, wind energy systems, human power, biomass, and hydrogen fuel-cell fundamentals. A partnership between the University and selected area high schools and middle schools was established for the improvement of students' mathematical and scientific skill sets and to improve teachers' knowledge about renewable energy systems. In order to mentor and manage the learning environment effectively, students were given a professional skill set for successfully applying mathematics and science to technical projects with diverse teams, which could be applied throughout their careers. The use of a number of renewable energy and energy efficiency-based hands-on projects also was used to promote mathematics and science for high school teachers and students. The workshops on Applied Renewable Energy Areas project used undergraduate senior design, class projects, and independent (directed) study projects, such as the energy bike and hand-crank generator, which were introduced through a series of after-school visits and weekend professional development workshops during 2010. Teachers who completed workshops are now implementing the conventional and renewable energy concepts in their classrooms by having students learn about the energy bike, PV solar cells, and model wind generators. This learning creates an environment where young students become familiar with relationships in basic mathematics, science, and engineering technology that are applied to renewable energy fields.

Mobile Unit

A 22-foot V-nose enclosed trailer was purchased and modified to house various renewable energy equipment, tools, and materials. This trailer was modified only to transport necessary platforms for the workshop. It was not intended as a classroom or demonstration unit. All of the platforms were unloaded into an outdoor environment for experiments after the trailer arrived at the school districts. After completion of the workshops, all of the platforms were loaded onto the trailer in order to transport all of the equipment back to campus; the trailer was pulled by a department truck. To hold the training boards and other equipment, cabinets with shelves were built by construction management students as class projects. Volunteer students and faculty traveled in a department van to school districts. Figure 2 shows a photograph of the modified trailer.

The project team wanted to make a wrap outside of the trailer to promote and advertise the project when the trailer was in motion. However, due to the proposed cost of the wrap by several local companies, the team decided to use the University's Sign shop, which offered to make a simple decal at an inexpensive price. A graphic design student accomplished the design work for the project logo and motto (Figure 3) as volunteer work. A design and development major student designed several cabinets to build inside the trailer to hold materials and tools.

Figure 2. Workshop Trailer

Equipment and Materials Housed by the Trailer

For science, agriculture, and technology education teachers, a portable mini-lab training unit was custom built and used. This training unit was also used for high school student experiments. The system has the capability to accept several different renewable energy sources at a time and convert these intermittent voltage sources to a constant voltage for charging a battery. The charge controllers handle the charging process of the battery at different input voltages that vary with the intensity of light energy, wind speed, or human kinetic energy. The modules and sub-modules of power generation from ambient energy sources using the Alternative Energy training unit are detailed for each energy source in Table 1.

Promoting STEM MREE
Mobile | Renewable | Energy | Education

Promoting Science Technology Engineering Mathematics

Figure 3. Project Logo and Motto

Table 1. Components Used for Hands-on Experiments of the Workshops

Photovoltaic System	Wind System	Human Power
PV modules	wind turbine	electric bike
light and charge controller	charge controller	bike power generator
lightning arrestor	lightning arrestor	portable power pack and power monitor
circuit breakers and fuses	start/stop switch	bridge rectifier
solar pathfinder	circuit breaker/fuse	DC/AC light bulbs
battery	amp-meter	fuses
amp-meter	DMM & precision resistor	hand-held power analyzer
digital multimeter (DMM)	anemometer	tachometer
temperature sensor	wind vane	hand-crank generator
irradiation sensor	battery	

General Components
DC loads (DC receptacles, DC motor, LED light bulbs, windshield heater, resistors)
AC loads (AC receptacles, LED light bulbs, heater, AC motor)
power inverter and step-down transformer
battery (with protection fuse)
solar thermal air heating system
solar thermal water heating system
DMMs and amp-meters
temperature, light, sound, mass, rotary, force, VI, rainfall, humidity sensors
barometric pressure, heat index, wind chill, dew point sensors
piezoelectric materials
friction, thermoelectric, and flywheel kits

For the K5-K8 grade level students, various renewable energy kits were purchased or built. These kits usually were accompanied with lab manuals, which were more simplified and extended in order to offer more experiments and demonstrations. These kits were used mainly for K5-K8 grade level students. The units included a) Power House Green Essentials Edition, b) Solar Super Racing Car, c) 6-in-1 Educational Solar Kit, d) Intelligent Fuel Cell Car Lab, e) Alternative Energy Lab, f) Wind Power Educational Kit, g) Hand-Crank Generator, and h) Kinetic Energy (E-Bike). The Kinetic Energy E-Bike demonstrates energy generation through a generator by pedaling. Students learn how power is generated by pedaling and can see the voltage, power, current, and total power generated. Students also monitor and visualize the light intensity of various light bulbs with LED lights while pedaling.

Material Distributions and Advertisement

In addition to the project logo and motto labeled on the trailer, a website was built to distribute workshop materials. The website name was put on the trailer (see Figure 4). This website has project information, photographs, useful links, workshop schedules, etc. The website is still being developed to add more information.

www.shsu.edu/energy

1-936-294-1216

Figure 4. Website Information Logo on the Trailer Decal

Facts and Demographics

Since May, 2010, twelve renewable energy workshops were conducted to promote alternative energy and STEM education in K-12 schools. Table 2 (next page) summarizes the workshop facts. There are three more workshops scheduled for the spring, 2013, semester listed in the table.

There was only one workshop offered to teachers. The school districts where workshops were offered had a limited number of STEM teachers. Usually there was only one or two science and vocational education teachers, except in the Conroe ISD High School. Unfortunately, it was not possible to invite teachers from several school districts for one day at one location. The project team tried to determine a school district that was close enough to other school districts in order to schedule a STEM teacher workshop. This way, teachers could travel to the closest school district for a workshop on one of the Fridays during the spring, 2013, semester. A summary of participant and instructor numbers is given in Table 3.

A series of workshops was held on and off campus with participation from local area schools. The statistical information in Table 3 is given according to the registration and attendance rosters. This table gives a summary of facts based on the number of K-12 students and teachers. Student teachers, in particular, were involved and helped workshop instructors intensively. The hands-on sections of the workshops were conducted by student teachers under the supervision of the instructors. Student teachers were trained by the project investigators before the workshops to help students and teachers during the applied sections of the workshops. All of the materials applying to the workshops—including design work, surveys, forms, workshop workbooks, website, building affordable educational equipment, etc.—were prepared with the help of Industrial Technology program students and faculty.

Table 3. Workshop Facts - Summary

Number of students workshops offered (Boys and Girls Club of Walker County)	12
Number of teachers (Science and Vocational – including those teachers participated as mentor to student workshops)	32
Number of students (9-12 Grades)	185
Number of students (6-8 Grades)	54
Number of students (4-5 Grades)	46
The number of SHSU student teachers (Helped to conduct workshops)	24
The number of SHSU faculty and graduate students helped to conduct workshops	7

Curricula

Three different types of programs were developed and offered on different levels to students and teachers. Different curricula were developed and implemented for the workshops to increase student and teacher knowledge. Morning sessions were lectures and afternoon sessions were hands-on applied training under SHSU faculty or qualified student supervision. There were 3 faculty and 16 SHSU Industrial Technology students who served during the workshops to assist attendees, especially for hands-on training. Student teachers were trained by project investigators before the workshops to help students and teachers during the applied sections of the workshops. Three laboratories and two classrooms (Electronics, Production, and Biomass) were used to conduct the workshops at the SHSU campus. Laboratory manuals, registrations forms, flyers, and brochures were developed for teachers and students separately. Depending on the level of the participants, different lab equip-

Table 2. Workshop Information

#	School	Group	Place	Time/Date	Participation	Status
1	Conroe ISD	Science and Technology Teachers	Conroe ISD	8am-4pm May 12 2010	21 teachers	Conducted
2	Huntsville ISD, T-STEM Academy	High School Students	SHSU Campus	8am-3:30pm October 6 2010	22 students	Conducted
3	Boys & Girls Club of Walker County	Middle School Students	SHSU Campus	8am-3:30pm June 25 2010	20 students	Conducted
4	Boys & Girls Club of Walker County	Middle School Students	SHSU Campus	8am-3:30pm October 9 2010	14 students	Conducted
5	Conroe ISD	High School Students	Conroe ISD	8am-4pm May 16, 2012	20 students	Conducted
6	Huntsville ISD	High School Students	Huntsville ISD	8am-3pm November 29, 2012	18 students	Conducted
7	Coldspring ISD	High School Students	Coldspring ISD	8am-4pm April 26, 2012	28 Students	Conducted
8	Coldspring ISD	High School Students	Coldspring ISD	8am-4pm April 27, 2012	31 Students	Conducted
9	Coldspring ISD	High School Students	Coldspring ISD	8am-3pm October 19, 2012	29 Students	Conducted
10	Centerville ISD	High School Students	Centerville ISD	8am-3pm December 13, 2012	17 Students	Conducted
11	Centerville ISD	Middle School Students	Centerville ISD	December 13, 2012	20 Students	Conducted brief demonstrations.
12	Groveton ISD	High School Students	Groveton ISD	December 6, 2012	20 Students	Conducted
13	Richards ISD	High School Students	Richards ISD	March 7, 2013	Max 30 students	Scheduled
14	Palacious ISD	Middle and High School Female Students	SHSU Campus	February 22, 2013	30 Students	Conducted
15	Splendora ISD	High School Students	Splendora ISD	Spring 2013	Max 30 students	Cancelled by the school district. New date is being determined
16	Huntsville ISD	Teachers	Huntsville ISD	Spring 2013	Max 20 teachers	Date is being determined
17	Apple Spring ISD	High School Students	Apple Spring ISD	Spring 2013	Max 30 students	Cancelled by the school. New date is being determined
18	Willis ISD	Elementary School Students	Willis	Spring 2013	46 students	Conducted

ment was used to apply theory in a lab environment. Lunch and refreshments were provided to attendees. At the end of the workshops, surveys were conducted to receive feedback to create more effective workshops and to update curricula for both lectures and laboratory sections. The workshops that were introduced to area teachers and students centered on PV (photovoltaic) systems, wind technology, human power (kinetic energy), biomass (biodiesel), energy safety, energy conservation, and hydrogen fuel-cell basics. Discussions and demonstrations included in the workshops were aimed at increasing teacher and student knowledge of this exciting new area of research on renewable energy sources.

The ultimate goal of this new curriculum was its implementation into the classroom, which should have an overall effect of increasing the performance of Texas school students in math, science, and engineering courses. The project was used as a tool for fundamental pedagogical research in methodologies for the inclusion of renewable energy content in science classes, and three different curricula were developed for the purpose of the workshops. There was a single schedule for students and teachers in terms of topics. However, the level of topics drastically changed based on participant knowledge. For example, teaching photovoltaic systems for 9-12 grade students was different than information given to teachers. Additionally, hands-on experiments were different, based on participant knowledge. K-12 level students were offered low-power kits.

A tentative schedule of a typical day workshop is listed below. This schedule was subject to change based on the school district preference. Some school districts only allowed half-day workshops. In that case, workshop presenters kept lectures and hands-on activities short with basic demonstrations. The content of the presentation sessions and hands-on activities changed based on the grade level of students and background of the teachers.

8:00 - 8:15am: Introduction
8:15 - 8:45am: Basic Electronics
8:45 - 9:45am: Photovoltaic (Solar) Systems
9:45 - 10:00am: Break
10:005 - 11:00am: Wind Energy Systems
11:00 - 11:30pm: Energy Conservation and Auditing
11:30 - 12:00pm: Lunch
12:30pm - 3:00pm: Hands-on Experiments and Demonstrations (Workbook is provided)
3:00pm - 3:30pm: Feedbacks, Discussions, and Conclusions

Hands-on Activities

Table 4 (next page) summarizes the experiments conducted during the workshops. Experiments were divided into four categories based on the knowledge level of participants. In the table, some of the experiments are grayed out for the first three categories. These types of experiments were conducted using custom-built training equipment in the program and designed to offer a variety of experiments at several levels. Several selected photographs of learning activities are shown in Figure 5. There are more activity pictures by the school districts provided on the website.

Figure 5. Activities from the Workshops

Table 4. Experiments Offered to the Participants

Overview to Experiments Introduction to the Training Unit - Training Unit Guide Overview of Equipment and Materials					
Assignments		K5-8 Grade	K9-12 Grade	Teachers	Optional
Exp. 1	Basic Electricity & Measurements (Voltage, Current, Resistance, and Power)				
Exp. 2	Overview to Photovoltaic Technology				
Exp. 3	Solar Panel Output Measurements (Voltage, Current, Power, Temperature)				
Exp. 4	Series-Parallel Connections of Solar Modules				
Exp.5	Effects of Temperature, Irradiation, Humidity, Wind to Solar Module Output				
Exp. 6	Solar Panel Efficiency – Shading Effects				
Exp. 7	Solar Path Finder - Side Shading Analysis and Solar Tracking				
Exp. 8	Overview to Wind Power Technology				
Exp. 9	Wind Turbine Output Measurements (Voltage, Current, Resistance, and Power)				
Exp. 10	Series-Parallel Connections of Wind Turbines				
Exp. 11	Wind Power Efficiency – Wind Speed vs Turbine Efficiency				
Exp. 12	Wind Speed and Direction Measurements				
Exp. 13	Battery Charging & Protection				
Exp. 14	AC/DC Load Characteristics and AC/DC Conversions				
Exp. 15	Hybrid Systems - Wind and Photovoltaic				
Exp. 16	Energy Generation from Human Power – Electric Bike and Hand Crank Generators				
Exp. 17	LED (Light Emitting Diode) Technology and Comparison to Traditional Lighting				
Exp. 18	Energy Harvesting from Piezoelectric Materials				
Exp. 19	Flywheel Energy Harvesting and Storage				
Exp. 20	Energy Harvesting from Friction Technology				
Exp. 21	Thermoelectric Energy Harvesting Technology				
Exp. 22	Energy Harvesting from Hydrogen Fuel Cell				
Exp. 23	Hydrogen Generation – Electrolysis				
Exp. 24	Measurements I – Light, Temperature, VI				
Exp. 25	Measurements II – Sound, Mass, Rotary, Force, Rainfall				
Exp. 26	Measurements II – Humidity, Barometric Pressure, Heat Index, Wind Chill				
Exp. 27	Alternative Energy Laboratory Experiments Kit				
Exp. 28	6 in 1 Solar Educational Kit				
Exp. 29	Wind Power Science Kit				
Exp. 30	Power House Green Essentials				
Exp. 31	Measuring Wind Speed with Anemometer				
Exp. 32	DIY. Solar Super Racing Car				
Exp. 33	DIY. Solar Electric Boat				
Exp. 34	Human Power Lab (Energy Bike)				

Brief Questionnaire for Feedback

To evaluate the effectiveness of the workshops, students were asked to fill out a brief survey after completing the workshop. Pre- and post-tests were not conducted. Students verbally shared their feedback about the workshop content and wrote down their comments on the survey sheets. Surveys were conducted for each group that participated in the workshop in order to determine how satisfied participants were at the end of the workshops. Survey results are summarized in Figures 6-8. Survey questions were merged in Table 5 (next page) into two columns, each column corresponding to a workshop group (students and teachers), since there were minor changes in the survey questions.

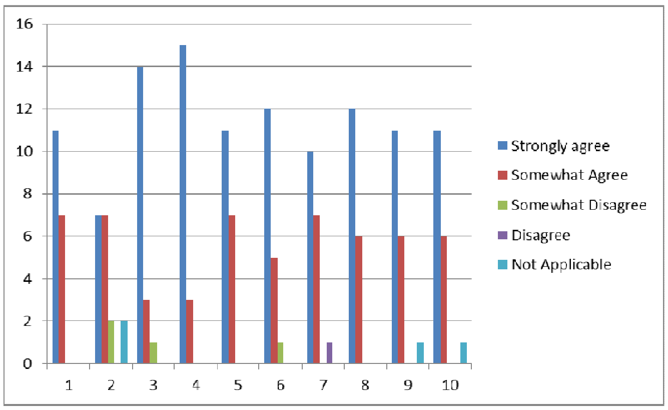

Figure 6. End-of-Workshop Survey Completed by STEM Teachers

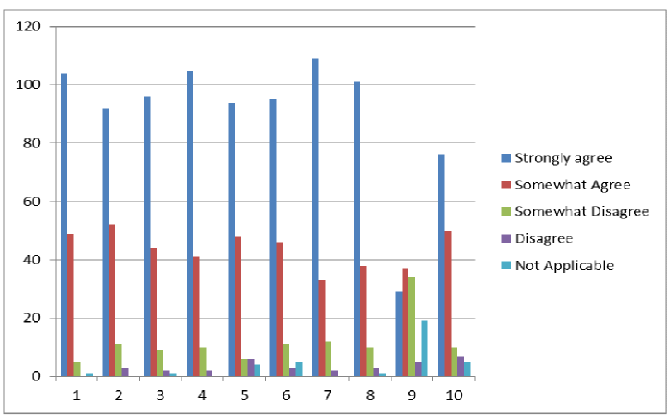

Figure 7. End-of-Workshop Survey Completed by High School Students

Summary

A successful partnership between the Agricultural and Industrial Sciences Department at Sam Houston State University and Entergy Inc. focused on providing educators and students with exciting, hands-on, unique learning tools that would initiate discussions about renewable energy applications, energy efficiency, and energy conservation in their students' lives. Though still in its infancy, there is an emerging movement in engineering education across the country, as evidenced by the growth in Science, Technology, Engineering, and Mathematics (STEM) academia and programs in secondary schools as well as the development and deployment of engineering and science curricula. However, rural school districts are often at a disadvantage; there are not sufficient student populations, resources, or qualified teachers necessary to implement these specialized programs.

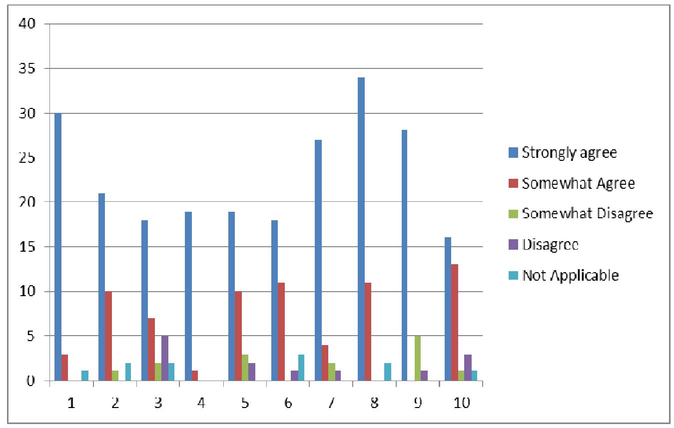

Figure 8. End-of-Workshop Survey Completed by Students from the Boys and Girls Club of Walker County

Research suggests that rural students are less likely to pursue engineering careers due in part to the lack of exposure to or unfamiliarity with the field. Collaboration between schools and institutions is an efficient way to promote engineering education by integrating renewable energy systems into coursework, which can generate more student interest than providing equation-based curricula. Renewable energy-related summer camps and workshops have proven to generate more student interest and promote STEM education, especially in rural areas where there is a lack of teaching tools and equipment. Teachers who have completed the workshop are then able to implement the energy concepts in their classrooms with renewable energy projects in order to create an environment in which students understand basic relationships among mathematics, science, and engineering technology applied to renewable energy fields.

Conclusion

The project anticipated helping rural schools teachers and students in K-12 education systems to learn STEM concepts by building renewable energy systems. The project, thus far (in its early stages) has provided professional development for up to 32 teachers in the content area of energy conver-

Table 5. Survey Questions for STEM Teachers, High School Students, and Boys and Girls Clubs

Intermediate, Middle and High School	STEM Teachers
1. Have you found workshop useful to improve your knowledge and skills on overall renewable energy applications?	1. Have you found workshop useful to improve your knowledge and skills on overall renewable energy applica-tions?
2. Have you found workshop useful to improve your knowledge and skills on energy efficiency and efforts on reduction of carbon foot prints?	2. Have you found workshop useful to improve your knowledge and skills on energy efficiency and efforts on re-duction of carbon foot prints?
3. Are Mathematical relations and calculations selected in this work-shop appropriate for your grade level?	3. Are Mathematical relations and calculations selected in this workshop appropriate for ***K5-K12***?
4. Do you think solar, wind, solar thermal, and human power applica-tions will help students to understand energy better?	4. Do you think solar, wind, solar thermal, and human power applications will help students to understand energy better?
5. Do you think renewable energy applications would be a good tool to promote STEM related careers for students?	5. Do you think renewable energy applications would be a good tool to promote STEM related careers for students?
6- Would you like to see Texas get more or future electricity from re-newable energy sources?	***6. Are you interested in implementing this applied renewable energy curriculum to promote Energy Education in your school?***
7. Facilities, materials, presentations, classroom demonstrations, and lab activities are selected well for this workshop.	7. Facilities, materials, presentations, classroom demonstra-tions, and lab activities are selected well for this workshop.
8. Overall quality of instruction was appropriate and useful for this class.	8. Overall quality of instruction was appropriate and useful for this class.
9. Did this workshop content and instructions change your future career interest or at least consider STEM related career?	9. This workshops may have a positive impact for students' future career interest or at least consider STEM related career?
10. I am interested in future workshops in these or similar subject mat-ters apply to STEM fields.	10. I am interested in future workshops in these or similar subject matters apply to STEM fields.

sion and conservation. It is estimated that 100 teachers will attend workshops by the end of 2013. So far, 251 students participated in workshops and provided very positive feed-back. It is expected that approximately 750 students will have attended by the end of 2013. Because rural school dis-tricts have few resources to enhance hands-on educational activities, the workshops will provide a valuable educational service. Similar to a science fair, the workshops allow par-ticipants to construct scientific projects, while using critical thinking skills. Furthermore, the alternative energy kits left at the school districts will help the science teachers as they engage students to formulate new ideas about energy pro-duction and conservation. Recent national studies have indi-cated that a combination of theoretical and hands-on learn-ing is the best way to promote an interest in STEM disci-plines. This project encompassed this approach and gave students from underserved rural areas the opportunity to participate in scientific and technological discovery.

Acknowledgements

Local companies provided some funding and equipment for workshops. The authors received $15,000 from a local electric utility company (Entergy Incorporated Charitable Foundation) to conduct workshops at local locations. For teachers, it is important to have professional development credits; thus, renewable energy workshops offer a good op-portunity to learn and earn credits.

References

[1] d'Archangelo, A. (2012, November 8). Brian Kelly discusses STEM gaps in the energy workforce pipe-line. Editor and Chief Content Officer of U.S. News & World Report. Retrieved from http://www.renewableenergyworld.com/rea/partner/total-energy-usa/news/article/2012/11/brian-kelly-discusses-stem-gaps-in-the-energy-workforce-pipelin

[2] Thomasian, J. (2011, December). Black Point Policy Solutions, LLC. NGA Center for Best Practices. *"Building A Science, Technology, Engineering, and Math Education Agenda"*. An Update of State Ac-tions. Retrieved from: http://www.nga.org/files/live/sites/NGA/home/nga-center-for-best-practices/col2-content/list-center-bottom/top-downloads/building-a-science-technology--@/1112STEMGUIDE.PD

[3] National Research Council. (2011b). *Successful STEM Education.* Retrieved from http://www.successfulstemeducation.org/content/nrc-report-successful-k-12-stem-education-identifying-effective-approaches-science-technolo

[4] National Research Council. (2011a). *Successful K-12 STEM Education: Identifying Effective Approaches*

in Science, Technology, Engineering, and Mathematics. The National Academies Press Washington, D.C. Retrieved from http://www.stemreports.com/wp-content/uploads/2011/06/NRC_STEM_2.pd

[5] National Science and Technology Council. (2011, December). Report from the Federal Inventory of STEM Education Fast-Track Action Committee on STEM Education. Retrieved from http://rise.uncg.edu/Fed%20stem%20report.pd

[6] Gonzalez, H. B., & Kuenzi, J. J. (2012 November 15). *Science, Technology, Engineering, and Mathematics (STEM) Education: A Primer*. CRS Report for Congress, Congressional Research Service.7-5700. R42642. Retrieved from http://www.stemedcoalition.org/wp-content/uploads/2010/05/STEM-Education-Primer.pdf

[7] National Science Board. (2010a). *Science and Engineering Indicators 2010*. Arlington, VA: National Science Foundation (NSB 10-01). Retrieved from http://www.nsf.gov/statistics/seind10/pdf/seind10.pd

[8] National Science Board. (2012). *Science and Engineering Indicators 2012*. Arlington VA: National Science Foundation (NSB 12-01). Retrieved from http://www.nsf.gov/statistics/seind12/pdf/seind12.pd

[9] National Science Board. (2010b, May 5). Preparing the Next Generation of STEM Innovators: Identifying and Developing Our Nation's Human Capital. Retrieved from http://www.nsf.gov/nsb/publications/2010/nsb1033.pd

[10] United States Government Accountability Office. (2012a, January). *Science, Technology, Engineering, And Mathematics Education Strategic Planning Needed To Better Manage Overlapping Programs Across Multiple Agencies*. Report To Congressional Requesters. GAO-12-108 Retrieved from http://gao.gov/assets/590/587839.pd

[11] United States Government Accountability Office. (2012b, February). *Science, Technology, Engineering, and Mathematics Education (page 214)*. 2012 Annual Report: Opportunities to Reduce Duplication, Overlap and Fragmentation, Achieve Savings, and Enhance Revenue. Report to Congressional Addressees. Retrieved from http://gao.gov/assets/590/588818.pd

[12] Snyder, T. D., & Dillow, S. A. (2011). *Digest of Education Statistics 2010* (NCES 2011-015). National Center for Education Statistics, Institute of Education Sciences, U.S. Department of Education. Washington, DC. Retrieved from http://nces.ed.gov/pubs2011/2011015.pd

[13] Snyder, T. D., & Dillow, S. A. (2012). *Digest of Education Statistics 2011* (NCES 2012-001). National Center for Education Statistics, Institute of Education Sciences, U.S. Department of Education. Washington, DC. Retrieved from http://nces.ed.gov/pubs2012/2012001.pd

[14] Carnevale, A. P., Smith, N., & Melton, M. (2011). Georgetown University Center on Education and the Workforce, Stem 23, 76. Retrieved from http://www9.georgetown.edu/grad/gppi/hpi/cew/pdfs/stem-complete.pd
Carnevale, Smith, and Melton, supra note 3.

[15] Chairman's Staff of the Joint Economic Committee. *Calculations using data from the Bureau of Labor Statistics. Employment Projections: 2010-20. Table 1.7 Occupational Employment and Job Openings Data, Projected 2010-20. Worker Characteristics, 2010.* February 2012. Available at bls.gov/emp/ Retrieved from esa.doc.gov/sites/default/files/reports/documents/stemfinalyjuly14_1.pdf

[16] STEM Education: Preparing for the Jobs of the Future (2012). *A report by the Joint Economic Chairman's Staff Senator Bob Casey, Chairman. United State Congress*. April, 10 2012. http://www.jec.senate.gov/public/index.cfm?p=Reports1&ContentRecord_id=92c8daf4-47c8-416a-bfa4-984cc8b6525

[17] U.S. Department of Education. (2012, September 28). Awards More Than $30.8 Million in Grants to Strengthen Math and Science Skills of Upward Bound Students. Retrieved from http://www.ed.gov/news/press-releases/us-department-education-awards-more-308-million-grants-strengthen-math-and-scie

[18] U.S. Department of Education. (n.d.). Upward Bound Math-Science. Office of Postsecondary Education Hom. Retrieved from http://www2.ed.gov/programs/triomathsci/index.htm

[19] Millersville University. (2012, March 15). 5th Annual Science Olympiad Retrieved from http://blogs.millersville.edu/exchange/2012/03/15/5th-annual-science-olympiad

[20] Millersville University. (n.d.). Summer Science Training Program Retrieved from http://www.millersville.edu/sstp

[21] BEST Robotics. (n.d.). Retrieved from http://www.bestinc.org

[22] VEX Robotics Competition. (n.d.) Retrieved from http://www.vexrobotics.com/vex/competition/vex-robotics-competition

[23] FIRST® Robotics Competition. (FRC). (n.d.). Retrieved from http://www.usfirst.org

[24] NEA. (2012). NEA to Expand STEM Teacher Training Program. Retrieved from http://neatoday.org/2012/10/02/nea-to-expand-stem-teacher-training-program

[25] National Center for the Advancement of STEM Edu-

cation. (n.d.). Retrieved from http://nacase.org
[26] U. S. News University Directory. (n.d.). Prepare for a Career as a STEM Teacher, Retrieved from http://www.usnewsuniversitydirectory.com/articles/prepare-for-a-career-as-a-stem-teacher_11980.aspx#.UO7JWFLNle
[27] ESRI. (n.d.). Advancing STEM Education with GIS. Retrieved from http://www.esri.com/library/ebooks/advancing-stem-education-with-gis.pd
[28] Texas STEM Network (T-STEM). (n.d.). Retrieved from http://www.ingenuitycenter.org/professional-development/texas-stem.html?PHPSESSID=d0b775dbc2580049c6be626c778738f
[29] Successful STEM Education. (n.d.a). Retrieved from http://successfulstemeducation.org/resource
[30] Successful STEM Education. (n.d.b). Culturally Relevant Ecology, Learning Progressions, and Environmental Literacy. Retrieved from http://successfulstemeducation.org/content/culturally-relevant-ecology-learning-progressions-and-environmental-literac
[31] Successful STEM Education. (n.d.c). Tornado, Hurricane and High Impact Weather Education and Research. Retrieved from http://successfulstemeducation.org/content/tornado-hurricane-and-high-impact-weather-education-and-researc
[32] Southwest Utah Renewable Energy Center (SUTREC). (n.d.). Retrieved from http://sutrec.org/page.php?id=4
[33] Oregon State University. (n.d.). On-site Renewable Energy Retrieved from http://oregonstate.edu/sustainability/renewabl
[34] Wordpress. (2012, April 19). Mobile Renewable Energy Education Trailer Retrieved from http://bysolar.wordpress.com/2012/04/19/mobile-renewable-energy-education-trailer
[35] Entergy. (n.d.). Charitable Foundation Grant Guidelines and Application. Retrieved from http://www.entergy.com/our_community/ECF_grant_guidelines.asp

Biography

FARUK YILDIZ is currently an Assistant Professor of Industrial Technology at Sam Houston State University. His primary teaching area is Electronics, Computer Aided Design, and Alternative Energy Technologies. Research interests include: low power energy harvesting, renewable energy technologies. Dr. Yildiz can be reached at fxy001@shsu.edu

DOUG KINGMAN has been involved with safety research for over 15 years. He is the inventor of the Liberty Rescue Tube that has been used to save the lives of farmers engulfed in grain. He also works with farmers with disabilities and teaches safety classes at Sam Houston state University. Dr. Kingman can be reached at dmk006@shsu.edu

DOUG ULLRICH is currently a Professor of Agricultural Education at Sam Houston State University. His primary teaching area is Career and Technology Mentorships, Professional Development and Agricultural Education. Research interests include: energy auditing, and Career and Technology Education. Dr. Ullrich can be reached at agr_dru@shsu.edu

KEITH L. COOGLER is an instructor of industrial technology at Sam Houston State University. He received a BS in Design & Development and holds a MA in Industrial Education and an Ed. D. in Higher Education from Texas A&M University – Commerce. His primary teaching area is Construction Management. Research interests include: automation, electronics, alternative energy, and “green” construction. Dr. Coogler can be reached at ith_klc@shsu.edu

BILL CROCKFORD is a registered Professional Engineer in Texas, is Lean Bronze Certified by SME, and holds three utility patents as sole inventor. His work experience includes the design, manufacture and sale of closed loop testing machines, and work in aviation and transportation materials related disciplines. During the course of this research, he taught as an Assistant Professor in Industrial Technology. Dr. Crockford can be reached at wwc@shedworks.com

JOE MULLER is currently an Associate Professor of Agricultural Engineering Technology at Sam Houston State University. He has 40+ years' experience in agricultural mechanization and engineering technology within areas of: curriculum development, high school and collegiate instruction, research, industry service and management. Dr. Muller can be reached at agr_jem@shsu.edu

COMPREHENSIVE STUDY OF THE NON-LINEAR COUPLING EFFECTS BETWEEN AN ULTRASOUND TRANSDUCER AND A TARGET UNDER INSPECTION IN SONIC IR IMAGING

Yuyang Song, Toyota Research Institute of North America; Xiaoyan Han, Wayne State University

Abstract

Sonic Infrared (IR) imaging is based on thermographic detection of temperature rise due to frictional heating at crack faces under ultrasonic excitation. It is a promising nondestructive evaluation (NDE) technique. In Sonic IR, a coupling material is a thin layered material that separates transducer and sample. This material was originally used to prevent any residual marks on the samples from the ultrasound transducer. However, it was discovered that coupling materials may play a role in crack detection. In this study, a series of coupling materials is investigated, and a comprehensive analysis, using vibration waveforms and IR images/ signals on an aluminum bar sample, is presented. Correlation analysis between the acoustic and thermal energy in the crack is discussed, as well. Results verify that coupling material can play a role in crack detection.

Introduction

NDE is a key process used in product evaluation, troubleshooting, and research. It has been demonstrated that, as a novel hybrid NDE technique, Sonic IR is able to detect surface and subsurface cracks, delaminations, disbands, etc. in metallic and composite materials [1-8]. Since this technology was patented, it has been widely developed in both academe and industry [9-14]. The technology is based on measuring frictional heat generation along cracks in a sample caused by the application of high-frequency sound waves. The technique uses pulses of ultrasonic excitation applied to a sample for a fraction of a second. The heating at the crack is then captured by calibrated infrared cameras using real-time video/digital imaging [9], [10].

Originally, coupling materials were used to prevent ultrasonic transducers from leaving marks on samples during testing. However, it was found that these materials affected thermal signal levels [13], [15-17]. The importance of coupling material was revealed through the discovery of acoustic chaos [18]. Therefore, the influence of coupling material was investigated, and some preliminary results were presented [15], [16,17]. However, currently there is no literature showing systematic results focused on coupling materials, either from tests or simulations [18-20].

There are some discussions between researchers and manufacturers regarding the design of ultrasound systems. The Branson ultrasound systems, which are used widely in Sonic IR, are not designed for metal to metal contact. Based on this, bare engagement is not suggested for use during testing. Therefore, there are no data to show the tradeoffs in couplant usage. However, the authors suspect that there could be some absorption/damping of sound through the coupling materials. Thus, an investigation into the effects of different coupling materials for Sonic IR is warranted. In this paper, the relationship between the vibrational acoustic and thermal energy at the crack is evaluated quantitatively using six different coupling materials.

Experimental Setup

The experimental setup is shown in Figure 1.

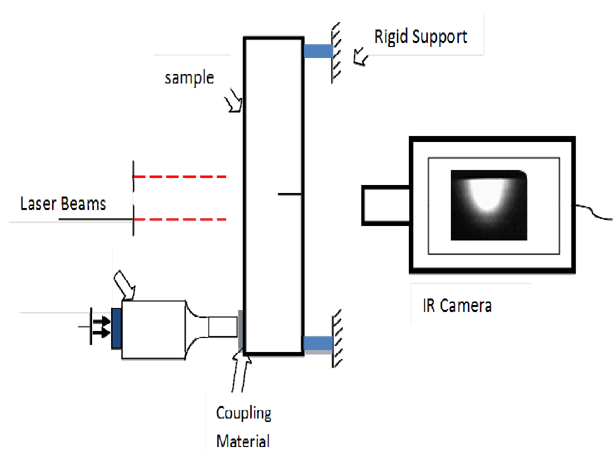

Figure 1. Schematic Drawing of Experimental Settings

The experiments used an aluminum (Al) bar with an edge -through crack as a test sample. All experimental conditions, as described below, are the same as in the previous work [12, 13]. The protocol difference in the current study is due to the coupling material. For each test iteration, a coupling material was placed between the ultrasound transducer tip and the sample. The coupling material used in the experiments was 25mm x 25mm x 0.6mm in size. The coupling materials were chosen based on previous experimentation [13]: folded duct tape (2LayerDT), laminated business cards (LamBC, with plastic films on both sides of the card), non-laminated business cards (NonLamBC, heavy cardstock paper), Teflon, gasket material, and leather. Photos of sample coupling materials are shown in Figure 2. The transducer was pressed against the test sample with a predefined load of 168 Newtons. Each coupling material test was repeated once without releasing the transducer. The sample was allowed a minimum of ten minutes to cool down between tests, so that all samples reached the same equilibrium temperature. For each test, the input ultrasound pulse was set to 800ms duration, the ultrasound transducer was placed on the coupling material at the same spot on the sample, and the camera position was kept constant.

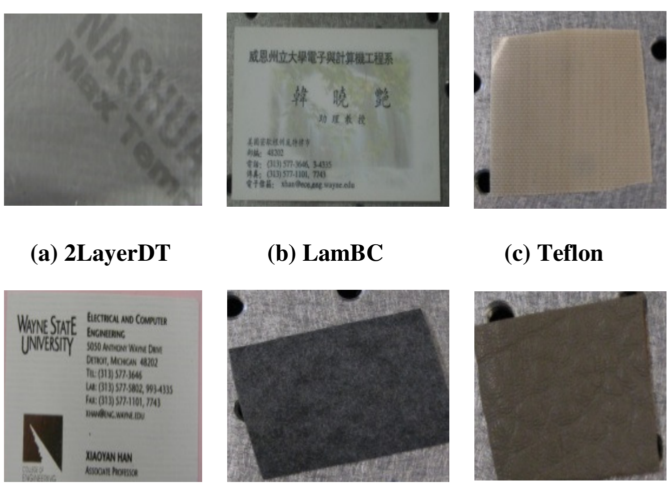

(a) 2LayerDT **(b) LamBC** **(c) Teflon**

(d) NonLamBC **(e) Gasket Material** **(f) Leather**

Figure 2. Photos of Six Different Coupling Materials used in the Experiments

In order to quantitatively characterize the experimental results, some energy calculation algorithms were developed [16], [17] to represent thermal energy and acoustic energy, though neither quantity is strictly energy. They are just a quantitative index. The thermal energy was calculated using Equation (1):

$$\sum_i \sum_j P(i, j, t) - \sum_i \sum_j B(i, j, t_{0^-}) \tag{1}$$

Details about the algorithm were shown in a previous paper [17]. The acoustic energy at a specific point on the crack was calculated according to Equation (2) [21]:

$$E = \int \left| S(t) \right|^2 dt \tag{2}$$

Experimental Results and Discussion

Quantitative Characterization of Coupling Material

Ultrasonic waves are reflected at boundaries where there is a difference between two materials. The difference in the acoustic impedance (Z) of the material on each side of the boundary causes the reflections [22], [23]. This difference in impedance is commonly referred to as an impedance mismatch. The greater the impedance mismatch, the greater the percentage of energy that will be reflected at the interface or boundary between one material and another. When the acoustic impedances of the materials on both sides of the boundary are known, the fraction of the incident wave intensity that is reflected can be calculated using Equation (3). The resultant transmitted wave energy propagates into the next material. The value produced is known as a reflection coefficient [23].

$$R = \left(\frac{(v1 \cdot d1 - v2 \cdot d2)}{(v1 \cdot d1 + v2 \cdot d2)} \right)^2 \tag{3}$$

Since the total amount of incident energy must equal the amount of reflected energy plus the transmitted energy, the transmission coefficient is calculated by simply subtracting the reflection coefficient from one. In Equation (3), v1 is the velocity of sound propagation through material 1 (coupling material), which is a function of both Young's modulus and density for the material, and d1 is the material's density. Similarly, v2 is the velocity of sound propagation through material 2 (Al bar), and d2 is the density of material 2. This is depicted in Figure 3.

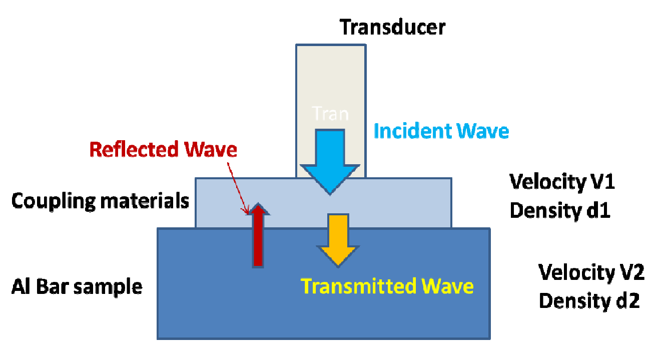

Figure 3. Acoustic Impedance and Refelection Coefficient

The camera was calibrated at room temperature, using the same parameter settings for all experiments. After each experiment, the thermal image of the crack area was saved, and then it was processed using custom imaging software. The pixel value automatically was determined at the point of interest. In each case, the temperature increase at the crack tip was converted by using Equation (4).

$$T = pixelvalue \times 4.19 \times 10^{-3} (1 \pm 1.35\%) \tag{4}$$

Dependence of Acoustic Energy on Coupling Materials

Figure 4 shows the results of the acoustic energy calculated using Equation (2), at a specific point on the crack, for the six coupling materials. The acoustic energy at the crack is plotted in order from highest to lowest: 2LayerDT, LamBC, Teflon, NonLamBC, Gasket Material, and Leather.

The relative vibration waveforms at the crack faces, as measured using a laser vibrometer, are plotted for the six coupling materials, as shown in Figure 5. The amplitudes of the waveforms for a) 2layerDT, b) LamBC, c) Teflon, d) NonLamBC, e) GasketMaterial, and f) Leather follow the same trend as the acoustic energy plot for the six coupling materials shown in Figure 4.

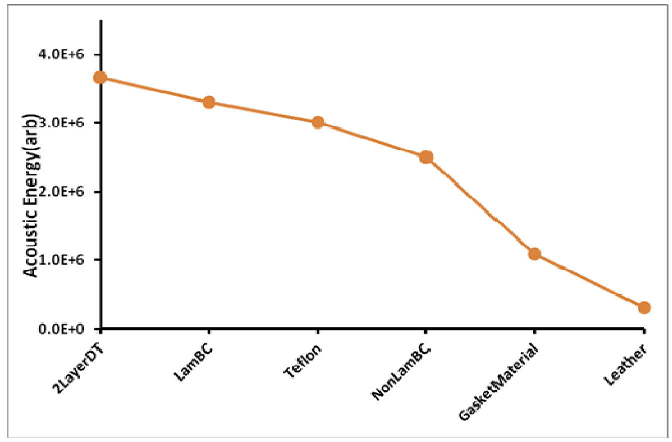

Figure 4. Acoustic Energy Calculated at a Specific Point on the Crack for the Six Coupling Materials.

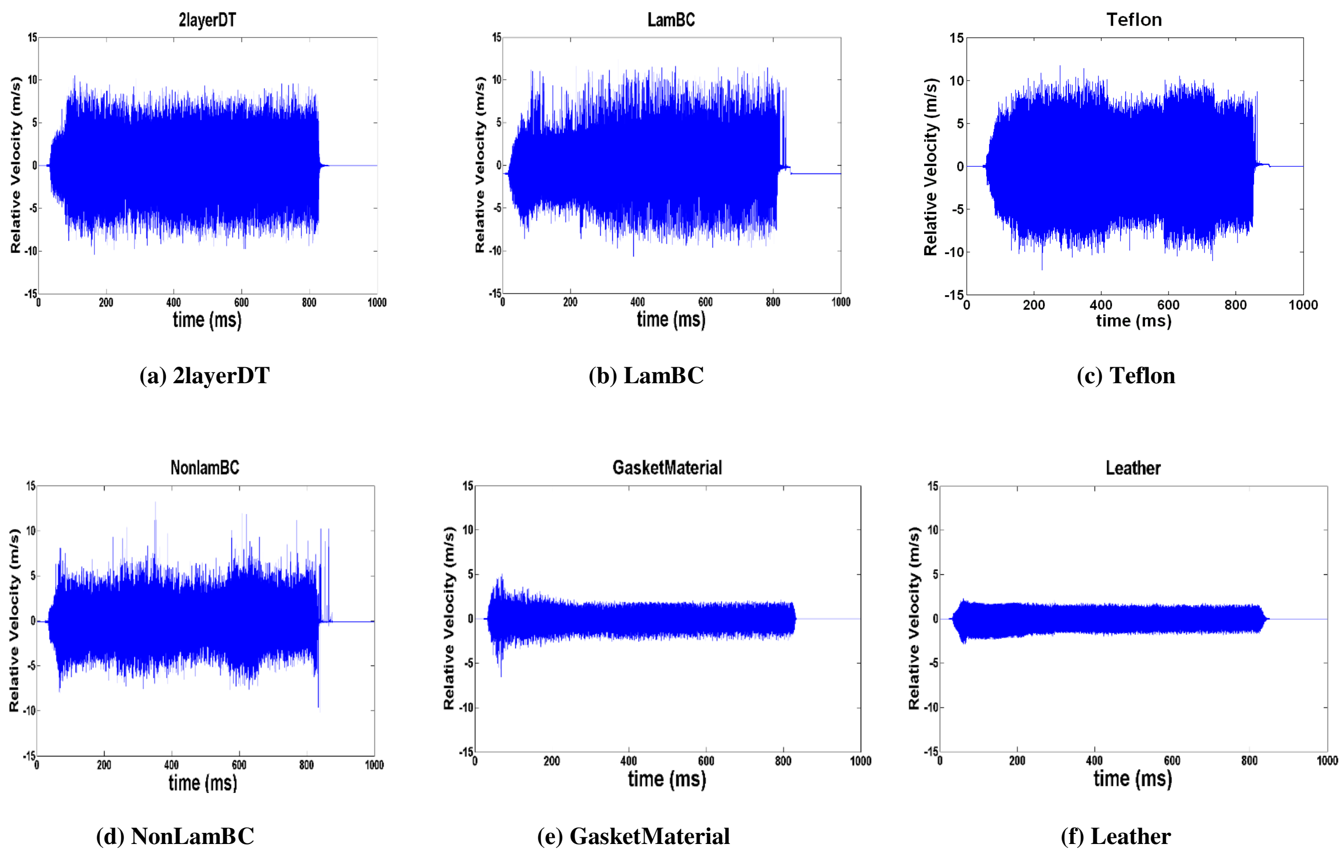

Figure 5. Relative Vibration Waveforms for the Six Coupling Materials

Dependence of Thermal Energy on Coupling Materials

In analyzing a 150x150 pixel area of interest around the crack, the first two background images were subtracted. Then, using Equation (1), the thermal energy levels were calculated from crack heating due to the energy transmitted through each of the six coupling materials, respectively. Figure 6 presents the thermal energy levels for each of the six coupling materials, in order from highest to lowest: 2LayerDT, LamBC, Teflon, NonLamBC, GasketMaterial, and Leather.

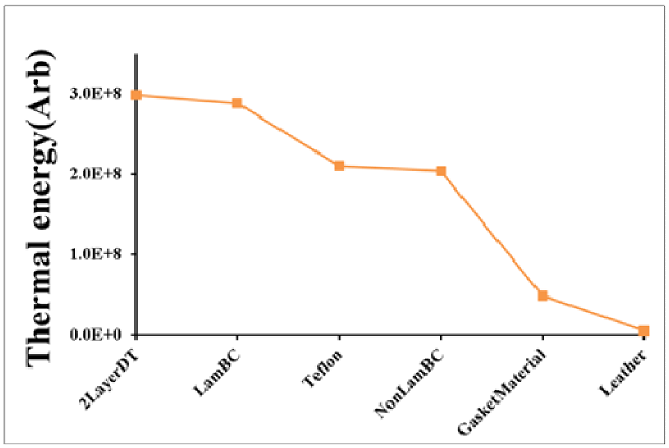

Figure 6. Thermal Energy Calculated from Crack Heating for the Six Coupling Materials

Figure 7 shows the IR images for all six coupling materials, taken at the time when the temperature of the crack is at its highest value. The same contrast was applied to all images for visual comparison. The corresponding temperature-time (T-t) plots at the crack interface are shown in Figure 8.

The maximum temperature increase among the experiments was approximately 16°C. It was assumed that frictional heating was the main contributor to the crack heating. Other mechanisms, such as plastic deformation, are unknown factors. This temperature increase, above room temperature, does not have an effect on the mechanical properties of the sample [24], [25]. Since the time intervals between experiments allowed the sample, including the crack area, to reach the equilibrium temperature of the lab, there was no residual heat left to skew subsequent testing. Figure 9 shows the initial thermal energy at the crack before each coupling material was engaged, just prior to the beginning of the test. The figure demonstrates that the boundary conditions for frictional heating were extremely similar for each test. Therefore, there was no bias due to previous experiments.

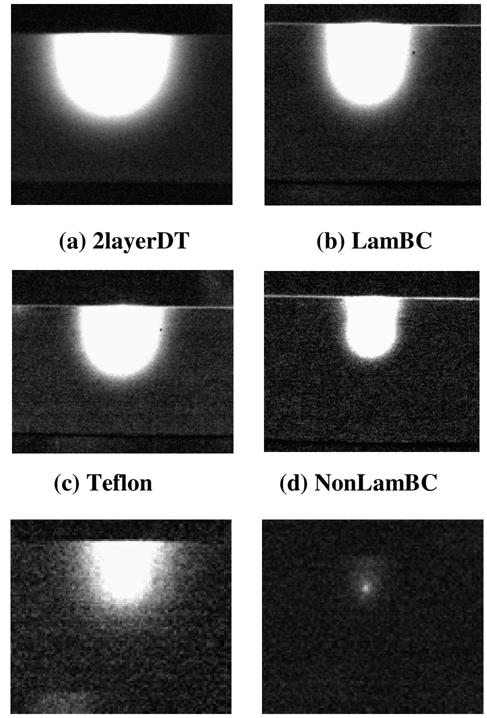

(a) 2layerDT **(b) LamBC**

(c) Teflon **(d) NonLamBC**

(e) GasketMaterial **(f) Leather**

Figure 7. IR Images of the Crack Taken with the Six Coupling Materials

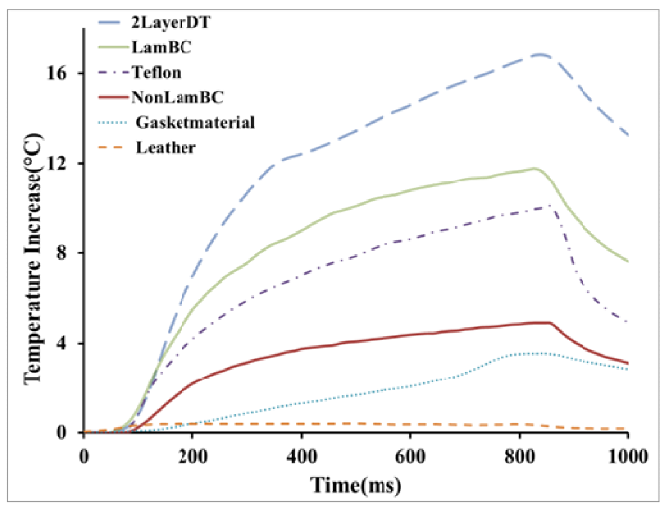

Figure 8. Temperature-Time Plots of the Crack for the Six Coupling Materials

Using Equation (3), the ultrasound reflection coefficients can be calculated. Correspondingly, the ultrasound transmission coefficients in the tests can be plotted. The transmission coefficients of the different coupling materials used in the tests were plotted in Figure 10, using the properties available in the database [23]. By inspection, it is clear that the trend of the coupling materials' transmission coefficients follow the same trend as both the thermal and acoustic energy. This is the inherent reason for the different results produced by these coupling materials.

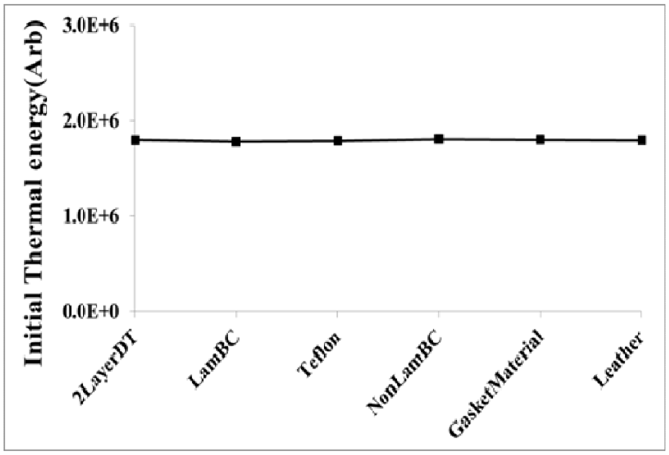

Figures 9. Initial Thermal Energy of the Crack Prior to each Coupling Material Test

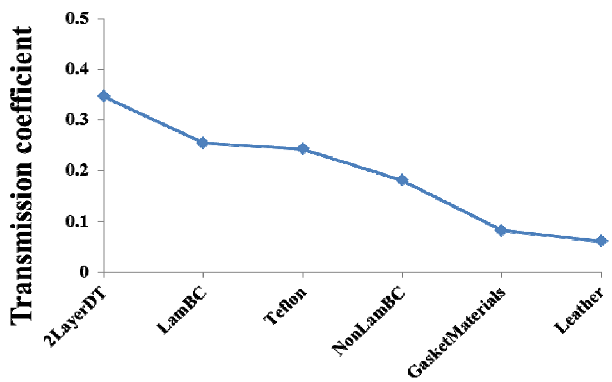

Figure 10. Transmission Coefficient and of Each Coupling Material

Further analysis into the reason for the different results from the coupling materials is shown as follows using a timeline alignment technique. The T-t plots, and their corresponding waveforms and spectra, for 2LayerDT, LamBC, and Teflon, are illustrated in Figures 11 through 13. These coupling materials produced the highest temperature increases at the crack tip. The alignment analysis gives a combination of both a global view and the local detail for the characterization of the coupling materials. Notice that the T-t plots have different slopes for different periods during the excitation pulse. In the case of 2LayerDT, the slope of the T-t curve in phase is higher than that in phase I. The same can be seen for LamBC & Teflon, and the trends for the slopes of the two phases are similar to 2LayerDT.

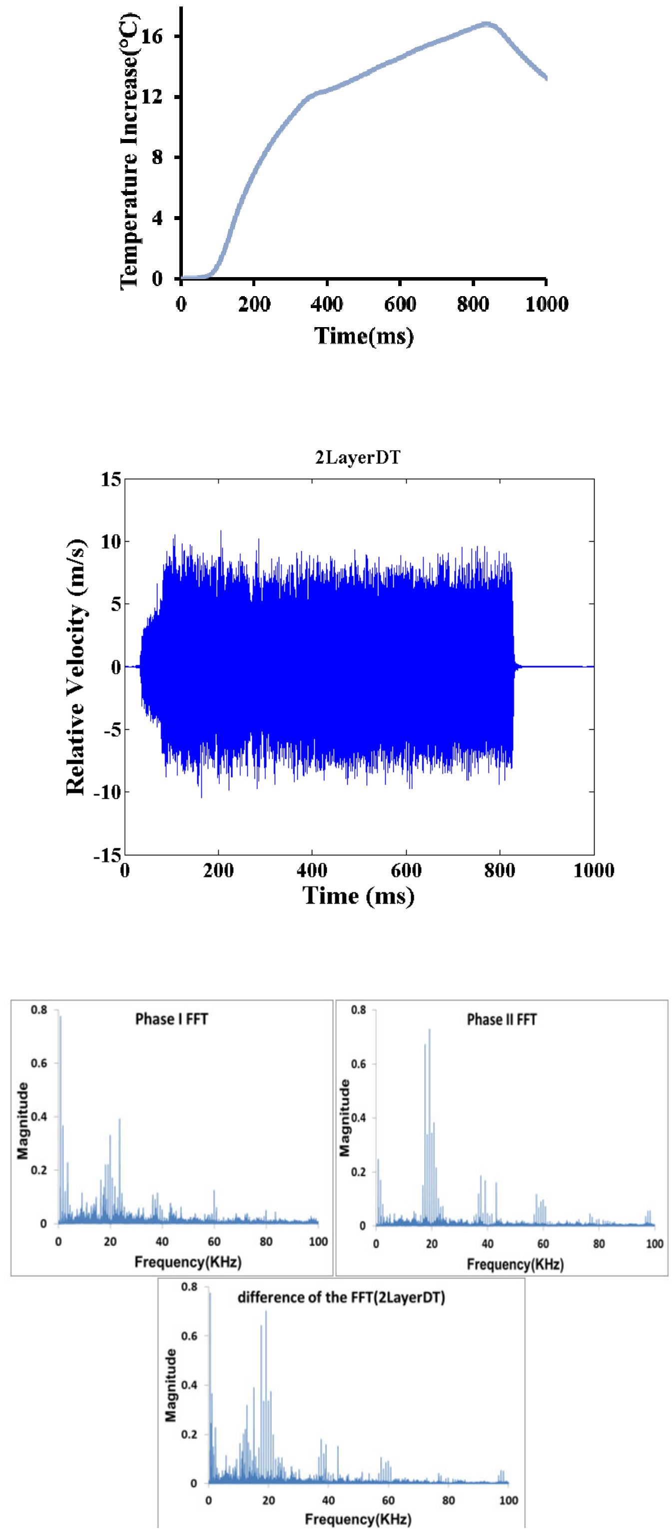

Figure 11. Correlating Crack Vibration and Crack Heating via Waveforms/Spectra and Temperature-Time Plot for 2layerDT

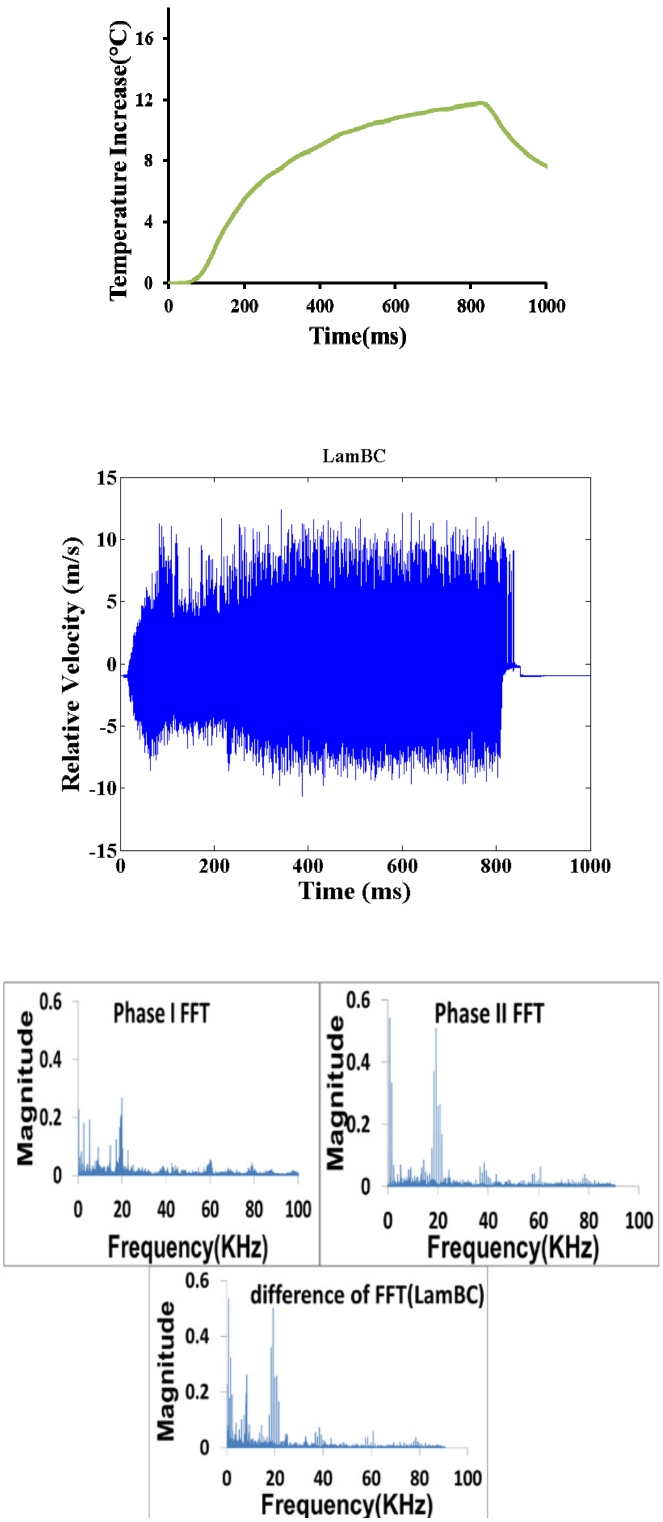

Figure 12. Correlating Crack Vibration and Crack Heating via Waveforms/Spectra and Temperature-Time Plot for LamBC

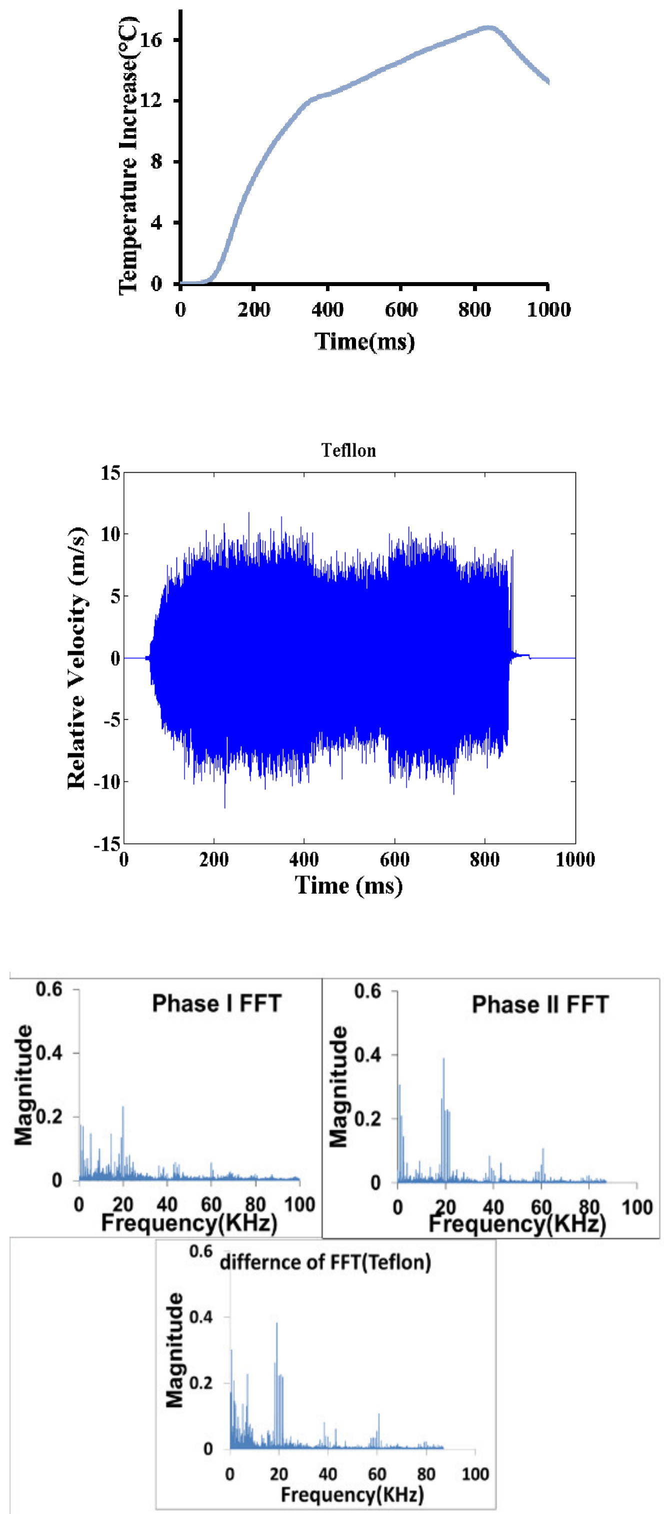

Figure 13. Correlating Crack Vibration and Crack Heating via Waveforms/Spectra and Temperature-Time Plot for Teflon

Numerical regression curve fitting was applied to the T-t plots, with the results shown in Figure 14. The slopes of the phase I T-t curves for these three coupling material tests, from highest to the lowest, are: 2LayerDT, LamBC, and Teflon. The waveform was divided into the time periods corresponding to phase I and phase II. The spectra for both phases were calculated as shown in Figures 11 through 13. The phase II spectrum shows a few dominated frequencies around which groups of frequencies are formed. However, the phase I spectrum is slightly more distributed. The difference between the phase I and II spectrums is plotted, as well. The magnitude of the FFT curve from differentiation also shows the same result.

Conclusions

Six different coupling materials were used between an ultrasound transducer and an Al bar test sample in Sonic IR imaging. The acoustic energy is correlated with the thermal energy. The amplitude of the vibration waveform at the crack interface decreases, as does the temperature change, for the coupling materials in the following order: 2LayerDT, LamBC, Teflon, NonLamBC, GasketMaterial, and Leather. In general, a higher waveform amplitude produces higher thermal energy in the region around the crack, although the relationship is not linear. Higher thermal energy makes a defect more detectable. The coupling material transmission coefficient through the Al sample plays an important role in this difference. Thus, choosing an appropriate coupling material, i.e., one that has a high transmission coefficient, leads to better crack detection in Sonic IR imaging. The correlation analysis between the ultrasound waveforms and their spectra shows further evidence of this conclusion. This study demonstrates that coupling materials can be an important factor in the detection of cracks.

Acknowledgements

This work was sponsored by Wayne State University.

References

[1] Favro, L., Han, X., Li, L., Ouyang, Z., Sun, G., Thomas, R., & Richards, A. (2001). Thermosonic imaging for NDE, *Review of progress in quantitative nondestructive evaluation*, *20*(2), 478.

[2] Favro, L., Thomas, R., Han, X., Ouyang, Z., Newaz, G., & Gentile, D. (2001).Sonic infrared imaging of

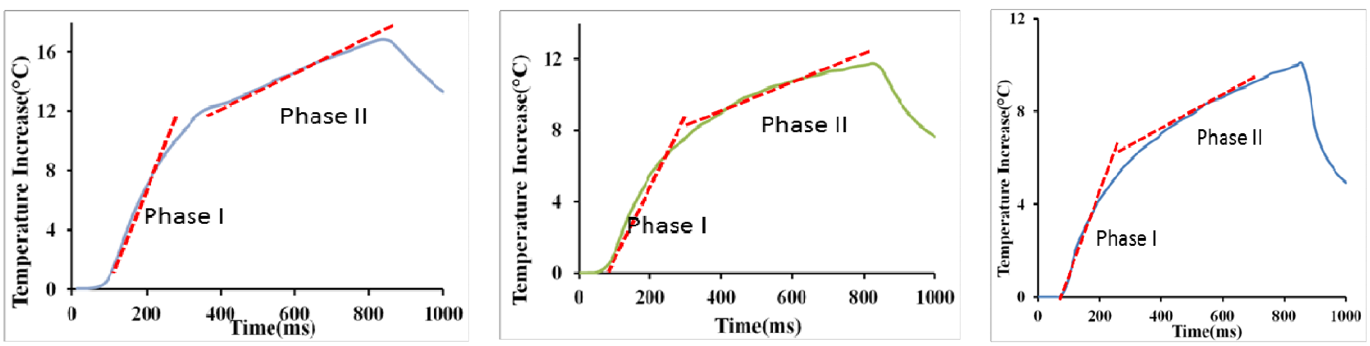

	Phase I	Phase II
2LayerDT	F(x)=0.046x-2.9449	F(x)=0.01x+8.3474
LamBC	F(x)=0.0325x-1.5856	F(x)=0.006x+6.4962
Teflon	F(x)=0.0213x-0.3907	F(x)=0.006x+4.4494

Figure 14. Fitted Curve for Two Phases of the Temperature-Time Plot for 2LayerDT, LamBC, and Teflon

fatigue cracks. *International Journal of Fatigue*, *23*, 471-476.

[3] Yi, H., Peng-Cheng, M., Zhong-Ning, Z., Shu-Yi, Z., Li, S., Xiu-Ji, S., et al. (2003).The Ultrasonic Infrared Thermography and its Application in NDE. *Journal of Nanjing University (Natural Sciences), 4*, 014.

[4] Zhu, Y.-K., Tian, G.-Y., Lu, R.-S., & Zhang, H. (2011). A Review of Optical NDT Technologies. *Sensors*, *11*, 7773-7798.

[5] Chen, C-H. (2007). *Ultrasonic and advanced methods for nondestructive testing and material characterization*. World Scientific.

[6] Han, X., Favro, L., Ouyang, Z., & Thomas, R. (2001). Thermosonics: detecting cracks and adhesion defects using ultrasonic excitation and infrared imaging. *The Journal of adhesion*, *76*, 151-162.

[7] Huang, S., Li, L., Yang, H., & Shi, K. (2001). In *NDE of composites delamination by infrared thermography*, NDE and Health Monitoring of Aerospace Materials and Composites II, 5046, 219-223.

[8] Li, G.-h., Wu, L.-x., Wu, M., & QU, J.-x. (2004). Current status and applications of infrared thermography. *infrared and laser engineering. 33*, 227-230.

[9] Mian, A., Han, X., Islam, S., & Newaz, G. (2004). Fatigue damage detection in graphite/epoxy composites using sonic infrared imaging technique. *Composites Science and Technology*, *64*, 657-666.

[10] Han, X., Lu, J., Islam, M. S., Li, W., Zeng, Z., Favro, et al. (2005). In *Sonic infrared imaging NDE, Proceedings of SPIE Smart Structures and Materials*, 5765(4), 142-147.

[11] Choi, M., Park, J., Kim, W., & Kang, K. (2008). In *Detection of delamination defect inside timber by sonic IR, Proceedings. of SPIE*, *6939*(2), 268-272.

[12] Song, Y., Godfrey, G., &Han, X.(2009). In What Role A Coupling Material Could Play In Sonic Ir Imaging, *AIP Conference Proceedings*, *1096*(1), 511.

[13] Han, X., Song, Y., & Godfrey, G. (2008). Investigation of non-linear effects of coupling materials in sonic IR imaging, *The 15th International Symposium on: Smart Structures and Materials & Nondestructive Evaluation and Health Monitoring*, *6932* (3), 225-228.

[14] Song, Y., & Han, X. (2012). Further study of coupling materials on aluminum sample using sonic IR, *AIP Conference Proceedings*, *1403*(2), 546.

[15] Han, X., & Song, Y. (2013). Study the effect of engagement force of ultrasound transducer on crack detectability in sonic IR imaging, *AIP Conference Proceedings*, *1511*(1), 532.

[16] Han, X., & Yu, R. (2007). Studying the effect of coupling materials in sonic IR imaging, *The 14th International Symposium on: Smart Structures and Materials & Nondestructive Evaluation and Health Monitoring*, *6529*(4), 869-972.

[17] Han, X., & He, Q. (2006). Developing thermal energy computing tools for sonic infrared imaging, *Proceedings of SPIE, Smart Structures and Materials, 6174*(3), 969-975.

[18] Gómez, T. E., & Montero, F. (2000). Bridging the gap of impedance mismatch between air and solid materials, *Proceedings of IEEE Ultrasonic Symposium,*.1072-1069 ,(6)1073

[19] Ke, W., Castaings, M., & Bacon, C. (2009).3 D finite element simulations of an air-coupled ultrasonic NDT system. *NDT & E International*, *42*, 524-533.

[20] Ballad, E., Vezirov, S. Y., Pfleiderer, K., & Solodov, I. Y., Busse, G. (2004). Nonlinear modulation technique for NDE with air-coupled ultrasound. *Ultrasonics*, *42*, 1031-1036.

[21] Cohen, L. (1995). *Time-frequency analysis*; Prentice Hall PTR, New Jersey.

[22] Auld, B. A. (1973). *Acoustic fields and waves in solids.* Wiley New York.

[23] Krautkrämer, H., & Krautkrämer, J. (1990). *Ultrasonic testing of materials*. (4^{th} ed.). Springer.

[24] Grewell, D. A. (1998).Welding system and method of setting welding machine parameters, US5772814 A,USPTO Office.

[25] Handbook, A. S. (1990). Aluminum and aluminum alloys. *ASM International*, *117*.

Biographies

YUYANG SONG is working at the Toyota Research Institute of North America as a Research Scientist, while concurrently working on his PhD at Wayne State University. His research focus is on nonlinear coupling effects of Sonic IR systems. His current research is related to application of NDE techniques in the automotive industry. Also, he is involved in lightweight material research at the Future Mobility Department at the Toyota Technical center in Ann Arbor. Mr. Song may be reached at yysongenator@gmail.com or yuyang.song@tema.toyota.com

XIAOYAN HAN is a Professor of Electrical and Computer Engineering at Wayne State University. Her research area is nondestructive evaluation and material characterization. She is part of a team that is receiving the Airlines for America (A4A) Better Way Award for their work on Implementing Sonic IR imaging on Critical Engine Components. Their WSU-patented technology uses sonic infrared imaging to detect flaws, such as cracks, in critical airplane engine components. Prof Han can be reached at xhan@eng.wayne.edu

INVESTIGATING THE SAFETY IMPACT OF RAISED PAVEMENT MARKERS ON FREEWAYS IN LOUISIANA

Subasish Das, University of Louisiana at Lafayette; Xiaoduan Sun, University of Louisiana at Lafayette; Yulong He, Beijing University of Technology, Beijing, China; Fan Wang, University of Louisiana at Lafayette; Charles Leboeuf, University of Louisiana at Lafayette

Abstract

Raised pavement markers (RPM) are intended as safety devices on roadways. Intuitively convinced by their safety benefits, the Louisiana Department of Transportation and Development (LADOTD) has been using RPMs for many years on all freeways in the state. Because of the not-so-positive RPM Crash Modification Factor published in the first Highway Safety Manual, the state has to evaluate safety benefits of RPMs in a warm climate. A study was conducted by the Louisiana Transportation Research Center to investigate RPM safety impact on freeway crashes with nine years of data. The safety effect of freeway striping was also evaluated, since the condition rating on RPMs and striping are made concurrently every year. The analysis results from the three methods indicated that RPMs have a significant effect in reducing crashes, particularly nighttime crashes at all AADT levels. For Annual Average Daily Traffic (AADT) under 20,000, the probability of getting a positive safety effect is given by the Highway Safety Manual (HSM) as 0.26 with a 1.13 Crash Modification Factor (CMF) and a standard error of 0.2. For the same AADT, the probability of a positive safety effect was estimated by this study as 0.97 on rural freeways. The analysis results also indicated that RPMs do not have any safety benefits on urban freeways.

Introduction

A raised pavement marker (RPM) is intended as a safety device installed on roadways. These devices are usually made with plastic, ceramic, or occasionally metal, and come in a variety of shapes and colors. Many varieties include a lens or sheeting that enhances their visibility by reflecting automotive headlights.

Intuitively convinced by its safety benefits, the Louisiana Department of Transportation and Development (LADOTD) has been using RPMs for many years on all freeways in the state. As with many highway devices, RPMs need to be replaced periodically to maintain their intended functionality, which requires significant resources. To select the most efficient crash countermeasure with the limited resources, the effects of all crash countermeasures need to be understood and qualitatively measured. Although the safety benefits of the RPMs are intuitively felt by drivers in Louisiana, there have not been many qualitative studies conducted showing their capabilities in crash reduction. The crash modification factor for the RPMs listed in the first edition of the Highway Safety Manual (HSM) has a CMF greater than one for AADT less than 20,000.

There is a need to substantiate the efficacy of RPMs in order to decide whether or not to continue the use of RPMs on freeways in Louisiana, which was precisely the purpose of this study.

Literature Review

Due to their popularity, numerous studies have been conducted on the evaluation of RPMs. The majority of these studies, however, were concerned with RPM installation procedures, durability, retro-reflectivity, costs, and optimum spacing. Relatively few studies have been conducted during the last 30 years on the safety effectiveness of RPMs. Wright et al. [1] evaluated the safety effectiveness of reflective raised pavement markers. From 1976 to 1978, the Georgia Department of Transportation installed reflective pavement markers on the centerlines of 662 horizontal curves. The study was intended to predict the change in nighttime crashes. Daytime crashes were also used at the same sites for comparative purposes. The results from the study showed a 22-percent reduction of nighttime crashes, compared with daytime crashes at the same sites.

A before-and-after study was conducted by Kugle et al. [2]. Two years of before-and-after crash data from 469 Texas sites (varying in length from 0.2 to 24.5 miles) were used for analysis. About 65 percent of the study sites were on two-lane roads; the rest were mostly on four-lane roadways. Three different evaluation methods were used in this study. The results showed the increment of nighttime crashes by 15 to 30 percent after RPM installation. Mak et al. [3] performed a study on the same dataset [2] in order to re-examine the impact of RPMs on nighttime crashes. In this current study, the RPM locations used in the previous study were reinvestigated to analyze the safety effect of RPMs rather than the influence of other countermeasures. A logit model was developed to evaluate the statistical significance by means of daytime crashes as the comparison group, which generated mixed results: 4.6 percent of the sites showed a significant decrease in nighttime crashes; 10.3 percent of the sites showed a significant crash increase; the rest, 85.1 percent, showed non-significant effects.

Griffin [4] analyzed the re-screened data from the Mak et al. [3] study by deploying a different statistical approach. Using a yoked comparison before-and-after methodology, the expected change in nighttime crashes following the installation of RPMs was estimated to be a 16.8 percent increase at the 95 percent confidence limits between a 6.4 and 28.3 percent increase. No information regarding the setting (urban or rural) of these roadways was mentioned in the study. Pendleton [5] used both traditional and empirical Bayes before-and-after methods to assess the safety impact of RPMs on the nighttime crashes on both divided and undivided arterials in Michigan. Seventeen locations (length = 56 miles) were considered as treatment sites, and 42 sites (approximate length = 146 miles) were used as control sites with no RPMs. Crash data for two years prior and two years after RPM placement were considered for the analysis. Undivided roadways showed a rise in nighttime crashes and divided roadways showed a decrease in nighttime crashes. The empirical Bayes methodology produced a smaller drop than the conventional before-and-after methodology. The New York State Department of Transportation (DOT) performed a simple before-and-after safety investigation of RPMs in New York [6].

In this study, the number of crashes before and after the placement of the RPMs was compared without controlling for other factors. On unlit suburban and rural roadways there was a non-significant 7 percent decrease in total crashes and a significant 26 percent decrease in nighttime crashes. On highway sections with proper lighting, nighttime crashes were reduced by 8.6 percent and total crashes were reduced by 7.4 percent. Orth-Rodgers and Associates, Inc. [7], used the same methodology as Griffin [4] to assess the effects of RPMs on nighttime crashes at 91 Interstate highway locations in Pennsylvania. The results showed a significant crash increase of 18 percent for nighttime crashes and 30 to 47 percent for nighttime under wet pavement conditions.

The aforementioned studies have conflicting conclusions on the impact of RPMs, which called for a comprehensive study by the National Cooperative Highway Research Program (NCHRP) in 2004 [8] to evaluate the safety effects of raised pavement markers. The data from two-lane and four-lane highways were collected from the six states for the analysis. The NCHRP study developed the Crash Modification Factors (CMF) for rural four-lane freeways that was published in the first edition of HSM, as shown in Table 1 [9].

Table 1. Potential Crash Effects of Installing Snowplowable Permanent Raised Pavement Markers from the HSM (Exhibit 13-51)

Setting (Road Type)	Traffic Vol. (AADT)	Crash Type (Severity)	CMF	Std. Error
Rural (Four-lane Freeways)	≤ 20,000	Nighttime All Types (All severities)	1.13	0.2
	20,001-60,000		0.94	0.3
	> 60,000		0.67	0.3

In summary, the previous studies on the safety effectiveness of RPMs had either a limited number of samples or did not separate rural from urban roadways in their analyses, which may explain some of their conflicting results. The NCHRP project did have a large sample size, but the results showed a negative impact of RPMs on roadway safety when AADT was less than or equal to 20,000. And, in Louisiana, 40 percent of rural freeways have AADT less than or equal to 20,000 (97.2 percent of Louisiana rural freeways are four-lane highways). None of the rural freeway segments in Louisiana before 2010 had AADT higher than 60,000.

Initial Data Analysis

The quality of RPMs along with pavement striping (center and edge lines) on Louisiana freeways is inspected annually by one designated engineer who gives subjective ratings. Three categories of ratings (good, fair, and poor) are used to describe the condition of the RPMs and striping. The segments in poor condition will be scheduled for either RPM replacement or re-striping. The nine years (2002-2010) of RPM and striping ratings for all Louisiana freeways were obtained for the analysis along with the corresponding nine years of crash data. On average, the good rating for RPMs lasts 2.2 years and 3.28 years for striping. During the nine years, a segment would experience several cycles (from good to poor) of ratings for RPMs or striping.

The RPM and striping ratings are made independently based on the control section, a segmentation method used by LADOTD. In total, there are close to 900 miles of freeways in 533 segments. Within each defined segment, the roadways' major attributes, such as lane width, shoulder width, number of lanes, type of pavement, AADT, etc., remain the same. The nine years' worth of crashes were populated into each segment based on their longitudinal and latitudinal codlings. Because of the difference in segment length and AADT, crash frequency could not be directly used for comparison. Thus, the crash rate (crashes per 100 million Vehicle Mileage Traveled [VMT]) was calculated for each segment. Due to the difference in freeway design and operation, the analysis was conducted for rural and urban highways separately. There are nine possible annual rating combinations—GG, GF, GP, FG, FF, FP, PG, PF, and PP—with the first letter for RPM and the second for striping (G as good, F as fair, and P as poor). Sample crash years of data for the used categories are shown in Table 2 and the summary of ratings is listed in Table 3.

Table 3. Summaries of Freeway Segments in Different Ratings

Freeway Location	Number of Segments in Each Rating Group								
	GG	GF	GP	FG	FF	FP	PG	PF	PP
Rural	606	85	171	63	110	140	75	31	285
Urban	1,028	189	280	156	214	266	141	88	734
Total	1,634	274	451	219	324	406	216	119	1,019

Note: segments under major maintenance/reconstruction marked as C are not counted

Excluding the mixed ratings from RPMs and striping, the first focus of the analysis was only on the cases with both ratings in the same category. Figure 1 shows a comparison of the crash rates for the rural freeway segment, where the overall average crash rate for both RPMs and striping with quality rating k is computed as:

$$\overline{R}_k = \frac{\sum_i \overline{r}_{k\,i}}{N} \tag{1a}$$

$$\overline{r}_{k\,i} = \frac{\sum_j r_{k\,i\,j}}{M_k} \tag{1b}$$

where,

$\overline{r}_{ki}$ = average crash rate over nine years on segment j with both ratings as k

$r_{k\,i\,j}$ = crash rate of segment j at year i with both ratings as k

N = number of segments

M_k = number of years both ratings in k for segment j

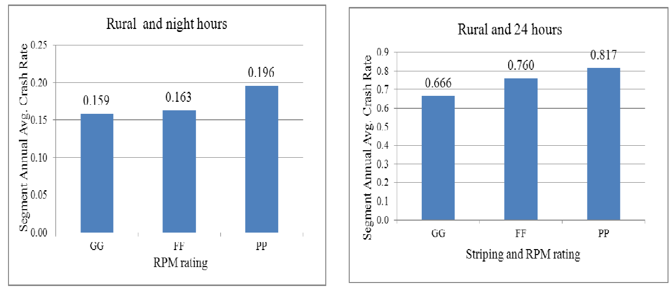

(a) Rural and Night Hours **(b) Rural and 24 Hours**

Figure 1. Average Crash Rates on Rural Freeways

It is encouraging to see that the quality of RPMs and striping does make a difference in the crash rate. As the combined ratings go from good to poor, the overall average crash rate increases. Since the RPM is particularly important at night for outlining traveled lanes, the nighttime crash rate is also computed with the 24-hour AADT, which shows the same trend. The increasing crash rate from good rating to poor rating was 22 percent for the 24-hour crash rate calculation, and 23 percent for nighttime crash rate estimation. However, as shown in Figure 2, the overall average crash

Table 2. Sample Crash Years of Data for the Used Categories

		2004		2005		2006		2007		2008		2009		2010	
Control Section	Length	Rating	Crash-es/ Mile	Rating	Crashes/ Mile	Rating	Crashes/ Mile	Rating	Crashes/ Mile	Rating	Crashes/ Mile	Rating	Crashes/ Mile	Rating	Crashes/ Mile
450-91	1.36	GP	1	GG	2	GF	1	FP	1	FP	3	FP	2	PG	1
450-91	3.4	GP	2	GG	3	GF	2	FP	2	FP	2	FP	1	PG	1
450-91	1.17	GP	0	GG	1	GF	1	FP	0	FP	0	FP	0	PG	0
450-91	0.13	GP	0	GG	0	GF	0	FP	0	FP	0	FP	0	PG	0
450-91	0.38	GP	0	GG	0	GF	0	FP	0	FP	0	FP	0	PG	0
450-91	0.58	FF	4	PC	1	CC	1	FP	1	FP	0	GP	1	GG	0
450-91	1.04	PP	2	PP	2	PP	2	PP	3	CC	1	GG	1	GG	1
450-03	0.76	GF	1	GP	1	GG	1	GF	1	FP	1	GG	1	GG	1
450-03	3.35	GF	2	GP	2	GG	3	GF	3	FP	1	FP	2	PG	2
450-03	5.62	GF	2	GP	4	GG	3	GF	3	FP	2	FP	2	PG	2
450-03	0.73	GF	0	GP	0	GG	1	GF	0	FP	0	FP	0	PG	0
450-03	1.79	GG	1	GP	1	GG	1	FP	0	FP	0	FP	0	PG	0
450-03	3.01	GG	1	GP	1	GG	2	FP	1	FP	1	FP	2	PG	1
450-03	4.7	GG	3	GP	4	GG	5	FP	4	FP	2	FP	3	PG	3
450-06	0.38	PP	0	PP	1	PP	0	GG	0	GF	0	GP	0	PG	0

rates do not reveal any positive effect of RPMs and stripping. It is a challenge to estimate the safety effect of RPMs and striping separately, since both have somewhat similar functionalities. Figure 3 illustrates how overall average crash rates on rural freeways vary by either RPM or striping ratings over both nighttime and 24-hour periods.

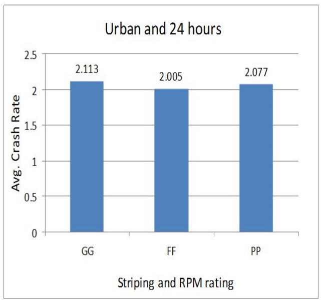

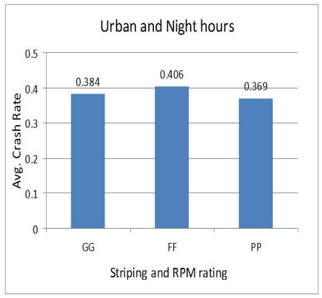

(a) Urban and 24 Hour **(b) Urban and Night Hours**

Figure 2. Average Crash Rates on Urban Freeways

The positive safety effect is still evident even with only one single rating, as shown in Figure 3, where the lowest crash rate is always associated with a good rating on either RPMs or striping. It can be seen that with one feature (RPM or striping) at rating k, the rating for the other feature can be in all three categories. That is, a RPM can have a good rating, while the rating for striping can be good, fair, or poor at the same time and location, which explains why the difference in the average crash rates between good ratings and poor for a single feature is not as big as the difference in the combined ratings between GG and PP. Nevertheless, the initial data analysis did demonstrate the safety effect of RPMs and striping independently.

Statistical Testing

The initial analysis results showed the difference in crash rates between good and poor ratings for RP and striping. Whether or not these differences were significant in statistical terms was then examined, where the ratings from each year on all rural freeway segments were used in the statistical test as one independent data sample instead of the segment averages. The differences between crash rates for good and poor ratings were examined by using a t-test at three AADT levels. The results of the statistical testing are listed in Table 4.

The statistic testing results show the safety effect of RPMs varies slightly by AADT. The crash rate difference between the two ratings was, indeed, statistically significant for RPMs alone and RPMs plus striping for AADT bigger than 20,000, as shown at the bottom of Table 3. The negative lower and upper bounds of the estimated mean difference at the 95-percent confident level ascertains the positive effect of RPMs and striping, jointly and separately, for rural freeways with AADT bigger than 20,000. Although similar results can also be seen in the upper part of the table showing the results for all rural freeways, the test results in the middle part of the table are slightly different. For the rural freeway segments with AADT less than 20,000, the crash rate difference between two RPM ratings was only statistically significant for nighttime data (at the 90-percent confidence level). The positive upper bound of 0.003 indicates the existence of uncertainty.

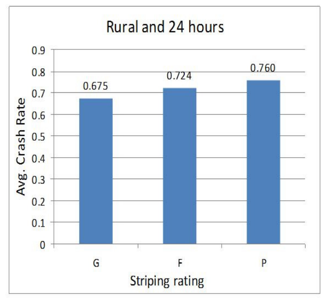

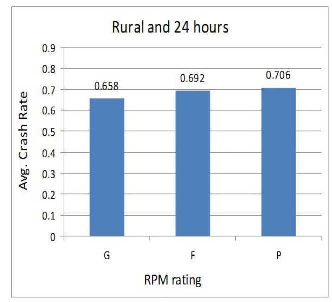

(a) Striping for Rural and 24 Hours **(b) RPMs for Rural and 24 Hours**

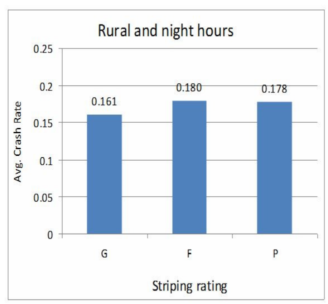

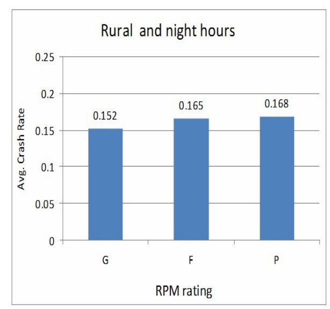

(c) Striping Ratings for Rural and Night Hours **(d) RPM Ratings for Rural and Night Hours**

Figure 3. Average Crash Rates by Single Rating

The results from this study were somewhat different from the CMF given by the HSM. Since crash rate (used in this current study) and CMF are two different concepts, one cannot simply compare their values. However, the RPM effect expressed by the CMF and crash rate difference can be illustrated by the probability calculation based on the information listed in Table 1 and from this study. For AADT under 20,000, the probability of getting a positive safety effect was calculated as 0.26 with 1.13 CMF and a standard error of 0.2. For the same AADT, the probability of a positive safety effect was calculated as 0.97 with the crash rate difference of -0.033 and a standard error of 0.018. Both calculations are displayed in Figure 4.

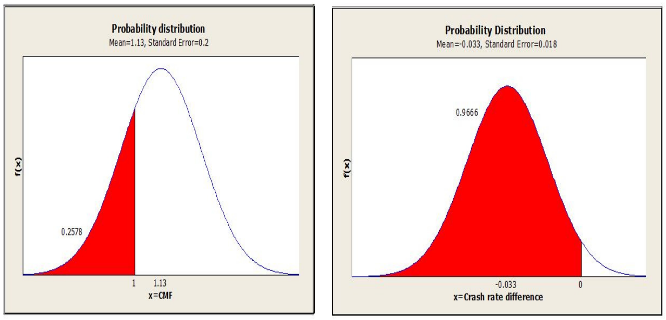

(a) CMF **(b) Crash Rates**

Figure 4. Probability of Positive Safety Effects of RPMs

For AADT between 20,000 and 60,000, the probability of getting a positive RPM effect is 1 from this study and 0.58 from the HSM. As expected, the test on the urban freeways showed no significant difference (either positive or negative) in crash rates under all scenarios.

With and Without Analysis

Although the analysis with crash rates was considered the most reliable method for the evaluation, another method was also used to explore the safety effects of RPMs and striping at nighttime. Lacking a Safety Predictive Model for the freeway, the direct application of many safety evaluation methods recommended by the HSM was not suitable for this unique case. A so-called "with and without" crash analysis was performed, which not only considered AADT changes but also accommodated the difference in segment length.

The analysis method divided the ratings of each segment from nine years into two groups as "with" (with good rating) and "without" (with poor rating). Two adjustment factors, $r_{a(j)}$ and $r_{s(j)}$, were developed to account for AADT changes during the analysis years and different sample sizes between the "with" and "without" groups.

$$r_a(j) = \frac{\overline{A}_{wj}}{\overline{A}_{WTj}} \tag{2}$$

$$r_s(j) = \frac{N_{Wj}}{N_{WTj}} \tag{3}$$

where,

$\overline{A}_{wj}$ = average AADT of "with" group for segment j

$\overline{A}_{wTj}$ = average AADT of "without" group for segment j

N_{Wj} = number of years under "with" group for segment j

N_{WTj} = number of years under "without" group for segment j

The analysis results are given in Table 5, which show a clear crash reduction at night for RPMs.

Table 5. "With" and Without" Crash Analysis for Rural Freeways at Nighttime

		Expected Crashes			
Feature Type	**Number of Sections**	**With (Good)**	**Without (Good)**	**Expected Crash Reduction**	**% Reduction**
RPM	114	641	675	34	5.30%
Stripping	77	476	477	1	0.20%

Table 4. Results of Statistical Tests

Roadway Type	Feature	Crash Rate at	t-test for Equality of Means					95% Confidence Interval of the Difference	
			t	**df**	**Sig. (2-tailed)**	**Mean Difference**	**Std. Error Difference**	**Lower**	**Upper**
AADT ≤ 20,000									
Rural	RPM	Night	-1.781	489	0.076	-0.033	0.018	-0.069	0.003
Rural	RPM	24 Hrs	-1.101	489	0.271	-0.065	0.059	-0.181	0.051
Rural	RPM+Striping	Night	-2.603	309	0.010	-0.063	0.024	-0.110	-0.015
Rural	RPM+Striping	24 Hrs	-2.591	309	0.010	-0.212	0.082	-0.373	-0.051
20,000≤AADT ≤ 60,000									
Rural	RPM	Night	-2.665	816	0.008	-0.038	0.014	-0.066	-0.010
Rural	RPM	24 Hrs	-3.249	816	0.001	-0.142	0.044	-0.228	-0.056
Rural	RPM+Striping	Night	-2.285	492	0.023	-0.047	0.020	-0.087	-0.007
Rural	RPM+Striping	24 Hrs	-2.840	492	0.005	-0.168	0.059	-0.284	-0.052
AADT ≤ 60,000									
Rural	RPM	Night	-2.128	1339	0.033	-0.025	0.012	-0.049	-0.002
Rural	RPM	24 Hrs	-2.573	1339	0.010	-0.102	0.040	-0.180	-0.024
Rural	RPM+Striping	Night	-2.800	889	0.005	-0.045	0.016	-0.077	-0.013
Rural	RPM+Striping	24 Hrs	-3.504	889	0.000	-0.186	0.053	-0.289	-0.082

Discussion and Conclusion

Among the three analyses that all show the positive impact of RPMs on rural freeway safety in Louisiana, it was believed that the results from the statistical test offered the most reliable information. The other two analyses were based on the segment average over the nine years for either AADT or crashes; this not only greatly reduces the number of samples but also loses the accuracy of the results. It is possible that other crash countermeasures were implemented on the rural freeways during these nine analysis years. Since the RPM condition cycle is short (average 2.2 years in good rating) and annual RPM ratings are different at different locations, the effect of other crash countermeasures would not significantly affect the results. Based on the analysis, the work zone presents the biggest impact on freeway safety. The highest crash rates are consistently associated with the freeway segment under construction. When a freeway segment was under construction or major maintenance, the RPM and striping rating was coded as C, and thus excluded from the analysis. Although the ratings on RPMs and striping were subjective, it was believed that the errors caused by the subjective evaluation from one designated engineer could be consistent over space and time. The effect of subjective ratings on the analysis results should be minimal if not totally ignorable when the analysis is focused on the difference between good and poor conditions. Concerning potential errors in the subjective rating, the RPMs under fair conditions were not included in the analysis.

In summary, this study clearly showed that RPMs do make a difference on rural freeway safety under all AADT conditions in Louisiana. The RPM should be continually maintained on rural freeways in the state. The study also confirmed that there are no safety benefits for RPMs on urban freeways, probably due to lighting conditions. For well-lit urban freeways, there is no need to implement RPMs.

Acknowledgements

This study was supported by the Louisiana Transportation Research Center on a project entitled the “Development of Crash Modification Factors for Louisiana Roadways”.

References

[1] Wright, P. H., Zador, P. L., Park, C. Y., & Karpf, R. S. (1982). *Effect of Pavement Markers on Nighttime Crashes in Georgia.* Insurance Institute for Highway Safety, Washington DC.

[2] Kugle, C. L., Pendleton, O. J., & Von Tress, M. S. (1984). *An Evaluation of the Accident Reduction Effectiveness of Raised Pavement Markers.* Texas Transportation Institute.

[3] Mak, K. K., Chira-Chavala, T., & Griffin, L. I. (1987) *Evaluation of the Safety Effects of Raised Pavement Markers.* Texas Transportation Institute.

[4] Griffin, L. I. (1990). *Using the Before-and-After Design with Yoked Comparisons to Estimate the Effectiveness of Accident Countermeasures Implemented at Multiple Treatment Locations.* Texas Transportation Institute.

[5] Pendleton, O. J. (1996). *Evaluation of Accident Analysis Methodology.* Report No. FHWA-RD-96-039, Texas Transportation Institute.

[6] New York State Department of Transportation (1989). *Highway Safety Improvement Program—Annual Evaluation Report*. Albany, NY.

[7] Orth-Rodgers and Associates, Inc. (1998). *Safety and Congestion Management Research and Advanced Technology Applications— Final Report (Technical Assistance to the RPM Task Force).* Research Work Order Number 1, Philadelphia, PA, pp. 1–20.

[8] Bahar, G., Mollett, C., Persaud, B., Lyon, C., Smiley, A., Smahel, T., et al. (2004). *Safety Evaluation of Permanent Raised Pavement Markers*. NCHRP Report 518, Transportation Research Board, Washington DC.

[9] American Association of State Highway and Transportation Officials (2010). *Highway Safety Manual*. 1st Edition.

Biographies

SUBASISH DAS is a Ph.D. candidate of Systems Engineering in University of Louisiana at Lafayette. He earned his B.S. degree from Bangladesh University of Engineering and Technology (Civil Engineering, 2007) and M.S. (Civil Engineering, 2012) from the University of Louisiana at Lafayette. His interests are in big data in traffic safety, nonparametric statistical modeling, and data mining. Mr. Das may be reached at sxd1684@louisiana.edu.

XIAODUAN SUN is a Professor of Civil Engineering at the University of Louisiana at Lafayette. Dr. Sun has been working on the forefront of highway safety for the past decade evidenced by her active role in various highway safety related committees and NCHRP panels for nine highway safety projects. About 30 safety related research papers and project reports have been published by Dr. Sun in the past 10 years plus close to one hundred presentations made at conferences and professional meetings on the topic of highway safety including the most recent one as an invited key-note speaker to the upcoming the 5th International Conference on Urban Traffic Safety in Canada.

YULONG HE is a well-recognized safety researcher in China. She works for Beijing University of Technology as an associate professor at Center for Transportation Research. While teaching roadway safety classes, Dr. He has involved in numerous research projects on roadway safety and published close to 100 papers most in Chinese and few in English such as publications on Journal of Transportation Research (TRB). She also works as safety experts to review various World Bank projects in China.

FAN WANG and CHARLES LEBOEUF are the graduate students of Civil Engineering at the University of Louisiana at Lafayette.

IMPORTANCE OF JUST-NOTICEABLE-DIFFERENCES (JNDS) IN AUDITORY SIGNAL DETECTION TASK-GENDER DIFFERENCES

Bankole K. Fasanya, North Carolina A&T State University; Benedict M. Uzochukwu, Virginia State University;
Emeka P. Idoye, North Carolina A&T State University

Abstract

The importance of just-noticeable-differences (JNDs) in auditory signal detection is important in human factor related fields. Gender differences associated with JNDs are an important consideration when designing auditory information processing systems. In this study, participants were asked to indicate when they detected an increase or decrease in the signal intensity of a sound presented in a quiet condition. The minimum intensity of the signals was 57.5 dBA, and the maximum intensity of the signals was 63.5 dBA. The intensity changes were carried out in increments of 1.0, 1.5, 2.0, and 3.0 dBA. The results showed that female subjects outperformed male subjects in signal detection tasks, where the incremental change was small. This difference was significant, p=0.0019, when signal intensity was decreased by 1.0 dBA.

Results showed that the number of males and females who detected both increases and decreases in signal intensity were equivalent when the changes were in 2.0 and 3.0 dBA increments. When the signal was increased by 1.5 dBA, no significant difference was noticed between genders. However, female participants performed better when signal intensity was decreased by 1.5 dBA by approximately 15% more than the male participants. The results of this study are applicable in telecommunications, specifically earphone design, for auditory signal detection tasks in power plants, for intelligent alarm design, in hospital telemetry units, where a single person is doing multiple tasks, as well as in research environments.

Introduction

JNDs in auditory signal detection can impact human physiological and/or psychological response to varying conditions. As these conditions may affect sensory perception, any distinct gender differences associated with JNDs should be considered when designing auditory information processing systems.

Additionally, abnormalities in auditory perception, due to developmental, physiological, and/or psychological medical conditions, potentially can indicate serious implications for auditory signal detection relating to task-gender differences.

Background

Recently, researchers have questioned the role of gender in auditory detection tasks. However, few researchers have addressed gender differences in active listening performance tasks. It has been postulated that females have finer auditory acuity [1]. In a (2007) study by Ruytjens et al. [2], on human primary auditory cortex functional sex differences, the authors discerned gender differences in the part of the brain activated when comparing music to noise. The authors found that noise gave a significantly higher primary auditory cortex activation level in females, and that the males showed a deactivation level in the right prefrontal cortex. Szymaszek et al. [3] discussed the effect of age, gender, listener practice, and stimuli physical properties on auditory perception of temporal order in humans. They found that age-related deterioration is dependent upon the physical properties of the stimuli that are presented (which remains resistant to gender and practice). Bradley and Lang [4] showed that emotional reactions to acoustically presented stimuli mimic those elicited by visually presented stimuli.

Roberts and Bell [5] studied sex differences in the area of spatial ability, and found that males performed better on mental rotation tasks when compared to females. However, as the authors noted, there is dispute about the genesis of these gender differences, such that these abilities might derive from previous experience with spatial activity or from biological processes such as biological development or differences in hormonal levels. Further, they found that performance on mental rotation tasks has been linked to right parietal activation levels. The study focused on the relationships among gender, age, electroencephalogram (EEG) hemispheric activation, and 2-dimensional mental rotation task ability. The participants of the study included 19 eight-year-olds, 10 boys and 9 girls, and 20 college aged adults, 10 men and 10 women. The researchers recorded both a baseline EEG, and one while participants did mental rotational tasks. The study showed greater spatial ability for men, when compared to women, with no significant differences between boys and girls.

Newcombe et al. [6] studied sex differences in both spatial ability and spatial activities. The authors used a spatial experience questionnaire as the means for collecting data. The study listed 81 adolescent activities; exercises that involved spatial abilities. Forty-one of the activities were categorized as masculine, including football, darts, and carpentry. Twenty-one of the activities were categorized as feminine, including figure skating, gymnastics, and interior decorating. Finally, twenty of the exercises were categorized as sex neutral, including bowling, diving, and sculpting. The study revealed that male college students engaged more with spatially related tasks as compared to their female counterparts.

Miller et al. [7] examined factors, including gender and clinical history variables, which influenced the relation between EEG measures. The authors found that EEG asymmetry between childhood depression probands and a control group varied not only with the clinical variables, but also that gender was a significant factor.

Jausovec and Jausovec [8] “examined gender related differences in brain activity for the tasks of verbal and figural content [shown] in the visual and auditory modality.” The researchers used 30 participants each, female and male, who were asked to work on four tasks while their EEGs were recorded. The study showed that the main differences between genders were due to either visual or auditory, or a combination of both visual and auditory, processing modalities. “Gender related differences in neuroelectric brain responses could be observed during the solution of auditory and visual tasks; on the behavioral level only for visual tasks did females display shorter reaction times than males.” McFadden [1] studied sex differences in the auditory system. He found that females “have greater hearing sensitivity, greater susceptibility to noise exposure at high frequencies, shorter latencies in their auditory brain-stem responses, more spontaneous otoacoustic emissions (SOAEs), and stronger click-evoked otoacoustic emissions than the males, as a group” [1].

Additionally, he found that males were better at the localization of sound than their female counterparts, which included identifying binaural beats and signals in difficult masking tasks. The challenge, according to [1] is identifying the differences in gender auditory perception, since their origin and evolutionary importance is still unknown. McFadden argued that there was some indication that prenatal hormones could have something to do with the sex differences in auditory perception. Meanwhile, the study conducted by Fasanya et al. [9] on gender differences in multitasking activity related to auditory tasks revealed no gender differences in participants’ ability to perform divided attention tasks such as computational and auditory detection.

Research on cognition has brought about many theories on the role of gender in auditory detection tasks. Many researchers attributed some of these differences to brain activities and hormonal levels. Recent research has questioned the role of gender in auditory detection tasks, yet little scrutiny has been focused on gender related active listening engagement. Gender differences in signal detection are important in order to understand gender performance in a particular working environment. As Fasanya et al. [9] reported on gender differences in auditory perception and computational divided attention tasks, “It is a common knowledge that women are often said to be better at performing combined tasks than their male counterparts” [sic]. Weber [10] documented the percentage differences of intensity increments that can be considered as JNDs for different activities. The detectable differences in weight, hearing, and vision are ten percent, five percent, and eight percent, respectively. These percentage differences were determined in the 18th century. 20th century generations have increased in height, body size, capacity, information processing, understanding, perception, and knowledge. The question then arises, “Is the 5% for hearing still applicable, or as it changed?” This question prompted the current study.

Kiehl et al. [11] hypothesized that the processing of target and novel stimuli would elicit robust activation in all brain regions previously shown to have time-locked hemodynamic activity. According to the authors, all participants across age and gender would show suprathreshold activity in brain regions that were previously associated with target detection and novel stimulus processing. They concluded, given the narrow grasp of the relationship between scalp recorded electrical activity and hemodynamic activity recorded with fMRI, that no precise conclusion could be made relating the brain region activation to age and gender. The overall goal of the current research is to determine differences in auditory perception due to gender. It is hypothesized that females demonstrate increased performance at detecting JNDs in background signal intensity levels.

Method

Twenty-four subjects participated in this study: 12 males and 12 females. All participants involved in the study were students enrolled in the North Carolina Agricultural and Technical State University’s Industrial and Systems Engineering graduate program. Their ages ranged from 22 to 40 years (female mean = 27.4 yrs., SD = 4.11; male mean = 30 yrs., SD = 4.5). All participants were recruited through posted flyers and personal acquaintance.

Apparatus and Testing Materials

The apparatus and testing materials used to conduct the study included a model RE-143MC sound attenuating booth (shown in Figure 1), a Larson Davis System 824 sound level meter, a Gateway desktop computer, a Fonix audiometer, two loudspeakers, a CD recording of pink noise, ear muffs, a table, and a chair. Figure 2 shows the experimental set-up for the study. The auditory signals were delivered by the two loudspeakers placed three feet away from, and at 0^{o} and 180^{o} azimuths to, the seating position of the subject.

Figure 1. Acoustic Chamber

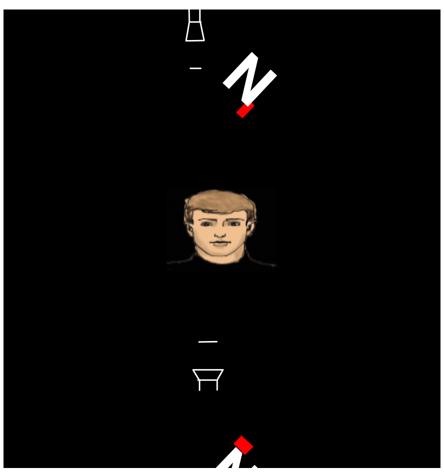

Figure 2. Experiment Set-up

Procedure

Preliminary procedures included obtaining "informed consent" through the University's Institutional Review Board (IRB). Prior to the start of the experiment, the noise file was opened on the computer. The audiometer was set-up, and all loudspeakers for noise in the acoustic chamber were set to ready. Pre-run tests on the loudspeakers were carried out to ensure that they were in good working condition. Once a participant arrived, he or she was welcomed and briefed on the purpose of the experiment. Questions from the participants were addressed at that time. Participants who agreed to proceed with the experiment were asked to sign an informed consent, and to complete a hearing pre-test screening form. Next, participants received instruction on the tasks for the screening exercise. Participants were instructed to push a button each time they detected/heard a pure tone in the acoustic chamber. Further, they were directed to do nothing if they heard no tone. During the screening, participants were seated in the center of the sound attenuating booth. The screening was conducted on each participant to ensure that they possessed normal hearing in both ears, as defined by hearing thresholds of 20 dB or below per octave for frequencies between 250 and 4000Hz. The audiometric testing was performed using a Fonix Hearing Evaluator (FA-10 Digital Audiometer) and a TDH-39P, C13357 Telephonics earphone, calibrated according to ANSI specifications for audiometers (ANSI, 1996). Listeners who passed the audio screening continued with the experiment. Those who failed the screening exercise were released from participation.

On completion of the screening exercise, the remaining subjects participating in the auditory detection task portion of the study received general instructions. A control trial was conducted with the first seven participants. During this process, background noise was played to determine each participant's background noise tolerance level (BNTL). The auditory detection task involved only the identification of background signal intensity changes. If the listener detected an increase or decrease in the level of background noise, the subject was directed to push the response button once or twice, respectively. The procedure was repeated. Upon completion of the first trial run, the experimenter notified the participant that the second trial would start. Each trial was completed in a five (5) minute time frame.

When the participant pushed the response button, the experimenter recorded a "Yes," indicating a correct response, or a "No," indicating an incorrect response. The decibel level for the background noise varied from 57.5 dB to 63.5 dB, with an average level of 60.5 dB. The intensity differences used in the study were 1.0, 1.5, 2.0, and 3.0 dB. The intensity ranges were determined based on the results of the pre-test conducted on the first seven participants. These intensities were considered as a participant's background noise tolerance level (BNTL). There were a total of twelve variations in the noise level, which encompassed all of the four decibel intensity differences. Each participant was required to detect signal level changes twenty four times in the combined trials, twelve intensity levels per trial. An incorrect response (i.e. clicking the response button twice without an actual increase or decrease in the noise level) was counted as a false alarm. Figure 3 shows the frequency spectrum cross section of the signal from the Sound Forge software.

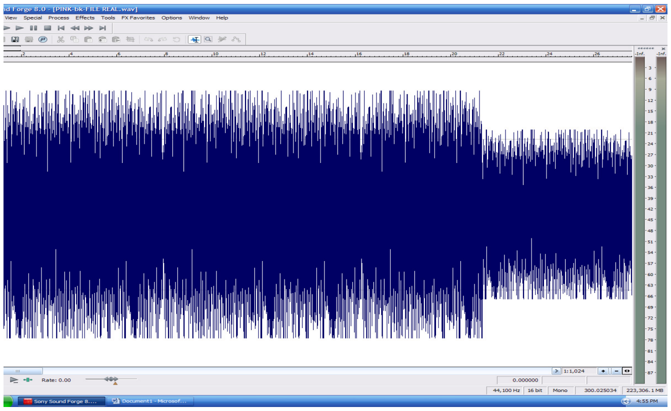

Figure 3. Frequency Spectrum of the Signal

Results

Descriptive statistics for the analysis are explained in this section. Table 1 shows the total number of participants that detected changes in signal level intensity during both trials. The results indicate that female participants demonstrated a higher level of auditory accuracy than their male counterparts in three of the eight intensity level trials. Table 1 shows the differences in the number of times a participant detected changes in the signal level as the intensity increased or decreased. Larger differences were noticed between the genders in the case where the signal intensity changed by 1.0 dBA. In the decreased intensity level of 1.5 dBA, nineteen females detected the changes in both trials, while only fourteen males were able to detect the decrease. No noticeable differences were observed between gender responses for other changes in noise intensity levels.

Table 1. Total Number of Participants that Detected Signal at the Different Intensity Levels in the Two Trials

Gender	1.0 dB Inc	1.0 dB Dec	1.5 dB Inc	1.5 dB Dec	2.0 dB Inc	2.0 dB Dec	3.0 dB Inc	3.0 dB Dec
Female	17	13	18	19	22	21	23	24
Male	6	4	17	14	22	20	22	24

Note: Inc. = Increase, and Dec. = Decrease

Table 2 shows the average score and the standard deviation for the signal detection task in both trials. From the table, it can be seen that females' signal detection in the first trial was greater by approximately 5% and by about 8% in the second trial than males'. Likewise, the number of false alarms made by the female participants was 11.33% lower in the first trial and approximately 6% lower in the second trial.

Table 2. Average and Standard Deviation of the Number of Signal Intensity Level Changes Detected Correctly, and the Number of False Alarms Made, in Both the First and Second Trials

Gender	SDDT 1	FAT1	SDDT 2	FAT2
Female	10.33 (1.30)	1.33 (1.87)	10.83 (1.03)	2.08 (2.68)
Male	9.42 (1.67)	1.67 (1.92)	9.33 (1.56)	2.33 (2.77)

Note: SDDT1 = Signal detected correctly in trial one; FAT1 = the # of false alarms made in trial one; SDDT2 = Signal detected correctly in trial two; and FAT2 = the # of false alarms made in trial two.

To better demonstrate these results, Figure 4 shows the graphical representation of the differences noticed in detection tasks between genders during the first and second trials, as well as the differences for recorded false alarms. This information is for the average scores of the detections by all participants in trials I and II.

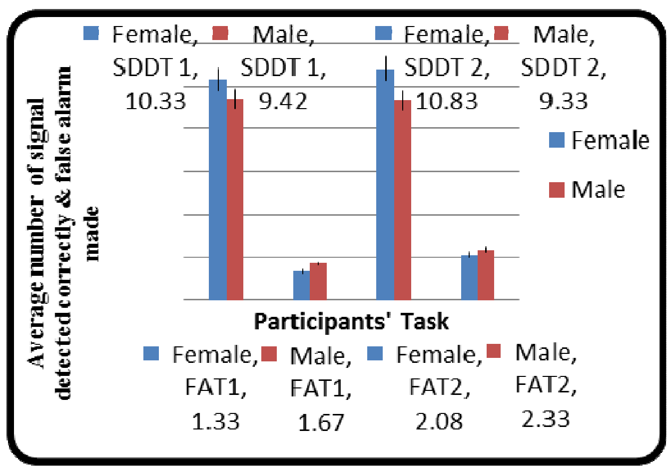

Figure 4. Graphical comparison of gender on auditory detection task

Figure 5 shows the relationship between gender responses at different signal intensity levels. In this figure, no difference, by gender, in the number of signal intensity level changes was observed when the signal level was increased by 2.0 dBA or when it was decreased by 3.0 dBA. Differences were observed in gender response when the signal intensity level was increased or decreased by 1.0 dBA. For a decrease in the signal intensity of 1.5 dBA, females detected level changes by approximately 15% more often than their male counterparts. For an increase in signal intensity of 1.5dBA, the difference was too small to conclude a statistically significant result between the genders. Next, an inferential statistic was conducted.

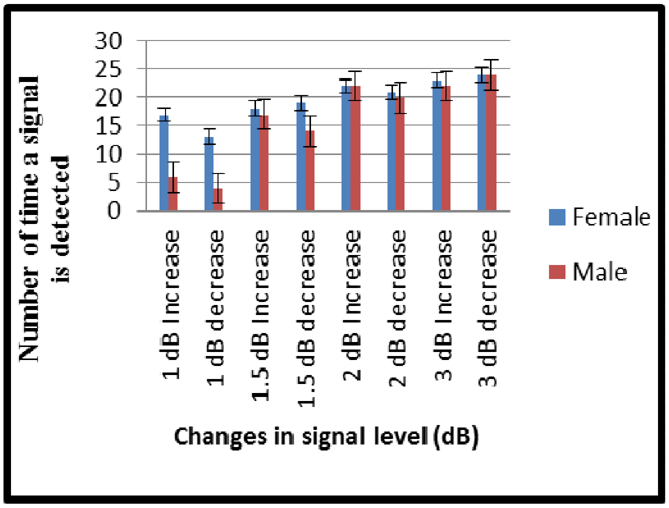

Figure 5. Level-by-Level Comparison of Gender Performance in Signal Level Detection

Further analyses to assess the differences between genders were conducted using Statistical Analysis Software (SAS) [12]. Prior to the analyses, data were checked for normality using the Shapiro-Wilk test and the Jarque-Bera test.

In the analyses, an unpaired t-test on the data for the ± 1.0 dB signal level change showed a statistically significant difference between genders in favor of females [α 0.05, t (46) = 3.30, p = 0.0019] (see Table 3). Likewise, the results of the unpaired t-test for the overall signal detection tasks showed a statistically significance difference, where the female participants outperformed their male counterparts [α = 0.05, t (46) = 3.00, p = 0.0043]. No statistically significant difference between the genders was found in false alarms [α = 0.05, t (46) = - 0.430, p = 0. 6661] see Table 4.

Table 3. Output of Participant t-test for ± 1.0 dBA Signal Intensity Level

Method	Variances	DF	t-value	Pr > \t\
Pooled	Equal	46.000	3.30	0.00190
Satterthwaite	Unequal	32.84	3.30	0.00230

Table 4. Output of Participant t-test for the Entire Signal Intensity Level Trials, both for Number of Signals Detected and the Number of False Alarms Made

Signal Detected Output				
Method	Variances	DF	t-value	Pr > \t\
Pooled	Equal	46.000	3.000	0.0043
Satterthwaite	Unequal	42.470	3.000	0.0045
False Alarm Output				
Pooled	Equal	46.000	-0.430	0.6661
Satterthwaite	Unequal	45.963	-0.430	0.6661

Discussion

The results of this study supported the initial hypothesis that females more accurately detect just-noticeable differences in background signal intensity levels. The results corresponded with previous studies that suggest females outperform their male counterparts in auditory sensitivity activities. In addition to noticing the differences during the 1.0 dB sound intensity level changes, this study indicated that females outperformed males by approximately 15% during the decrease in sound intensity of 1.5 dB. Overall, females' accuracy was shown to be statistically higher than males' accuracy. It is clear from Figure 5 that either gender can effectively detect both increases and decreases in signal intensity at the 2.0 dBA threshold, and above, which is approximately 3% of the original magnitude (either 57.5dBA or 63.5 dBA). Therefore, currently, the JND of change in sound level intensity for the combined genders is as little as three percent. This contradicts Weber's [10] five percent finding on the threshold of incremental change.

Limitations and Recommendations

There are some limitations that should be mentioned with regard to this experiment. First, no form of performance incentive was offered. This limited the number of subjects recruited for the experiment. However, participants were motivated to find out which gender performed more accurately in signal level change detection. Second, the experiment involved only a small cross section of students; the cohort population and recruitment should be expanded in future studies.

For future research, the following recommendations should be considered:

1. A larger sample size should be considered for better statistical power.
2. The number of trials should be increased from two to five, and the experiment should be spread, at a minimum, over a seven day window.
3. The time of day when this experiment is conducted may be put into consideration.
4. Participant age should be taken into consideration as an extenuating factor.

Conclusions

Based on the analyses of the empirical data, female subjects showed greater accuracy than their male counterparts in detecting just-noticeable-differences of 1.0 dB changes in background auditory sound intensity (both an increase and a decrease). Differences were also noticed during detection of a 1.5 dB decrease in background signal intensity level. Overall, the results showed that females outperformed their male counterparts in signal level change detection tasks. Results further showed that, instead of a JND of 5 percent in background noise level change, a three percent JND change is appropriate. The results of this study are applicable to situations involving signal level change detection tasks.

References

[1] McFadden, D. (1998). Sex Differences in the Auditory System. *Developmental Neuropsychology, 14*(2-3), 261-298.

[2] Ruytjens, L., Georgiadis, J. R., Holstege, G., Wit, H. P., Albers, F. W. J., & Willemsen, A. T. M. (2007). Functional Sex Differences in Human Primary Auditory Cortex. *European Journal of Nuclear Medicine and Molecular Imaging, 34*(12), 2073-2081.

[3] Szymaszek, A., Szelag, E., & Sliwowska, M. (2006). Auditory Perception of Temporal Order in Humans: The Effect of Age, Gender, Listener Practice and Stimulus Presentation Mode. *Neuroscience Letters, 403*(1–2), 190–194.

[4] Bradley, M. M., Lang, P. J. (2000). Affective Reactions to Acoustic Stimuli. *Psychophysiology, 37*, 204 –215. doi: 10.1111/1469-8986.3720204.

[5] Roberts, J. E., & Bell, M. A. (2000). Sex Differences on a Mental Rotation Task: Variations in Electroencephalogram Hemispheric Activation Between Children and College Students. *Developmental Neuropsychology, 17*(2), 199-223.

[6] Newcombe, N., Bandura, M. M., & Taylor, D. G. (1983). Sex Differences in Spatial Ability and Spatial Activities. *Sex Roles, 9*(3), 377-386.

[7] Miller, A., Fox, N. A., Cohn, J. F., Forbes, E. E., Sherrill, J. T., & Kovacs, M. (2002). Regional Patterns of Brain Activity in Adults with a History of Childhood-Onset Depression: Gender Differences and Clinical Variability. *American Journal of Psychiatry; 159,* 934-940.

[8] Jaušovec, N., & Jaušovec, K. (2009). Gender Related Differences in Visual and Auditory Processing of Verbal and Figural Tasks. *Journal of Brain Research, 1300,* 135-145. doi: 10.1016/j.brainres.2009.08.093.

[9] Fasanya, B. K., McBride, M., Pope-Ford, R., & Ntuen, C. (2012). Gender Differences in Auditory Perception and Computational Divided Attention Tasks. J*ournal of Computer Technology and Application (JCTA) 3*(9) 636-641.

[10] Weber, E. H. (1795-1878). Leipzig physiologist. *Journal of the American Medical Association,* 199 (4), 272–273.

[11] Kiehl, K. A., Stevens, M. C., Laurens, K. R., Godfrey, P., Calhoun, V. D., & Liddle, P. F. (2005). An Adaptive Reflexive Processing Model of Neurocognitive Function: Supporting Evidence from a Large Scale (n = 100) fMRI Study of an Auditory Oddball Task. *Neuroimage, 5*(25), 899–915.

[12] SAS Institute Inc., (2010). Statistical Analysis Software.

Biographies

BANKOLE K. FASANYA is currently working part-time as an Adjunct Instructor at Forsyth Technical Community College, Winston-Salem, North Carolina. He earned his B.S. degree from The Polytechnics Ibadan Nigeria, M.S.E. from Morgan State University, Baltimore, MD (Industrial, Manufacturing, and Systems Engineering, 2008), and Ph.D. (Industrial and Systems Engineering, 2013) from North Carolina Agricultural and Technical State University (NCA&T), Greensboro, NC. His areas of interests include Ergonomics and Human Factors, Safety, Environmental Noise Assessment, Quality, Continuous Process Improvement and Auditory Acoustics. Dr. Fasanya has published in several academic journals including the *Journal of Computer Technology and Application*, *Growing Science Journal*, and conference proceedings, both national and international. Dr. Fasanya can be reached at omdomd79@gmail.com

BENEDICT M. UZOCHUKWU is an Assistant Professor of Industrial and Logistics Technology at Virginia State University. His research interests include Human Factors and Ergonomics, Sustainment, Logistics, Supply Chain Management, Life Cycle Systems, Systems Integration and Management of Technology Systems. He has a Ph.D. degree in Industrial Engineering from North Carolina A & T

State University, Greensboro, and has several peer-reviewed publications to his credit. He belongs to a number of professional organizations, such as the Institute of Industrial Engineers (IIE), Society for Engineering Management (SEM), Society for Health Systems (SHS) and Association of Technology Management and Applied Engineering (ATMAE). He is also a member of Alpha Pi Mu and Phi Kappa Phi Honors societies. Dr. Uzochukwu can be reached at benuzo@hotmail.com

EMEKA P. IDOYE is currently a Ph.D. student in the Industrial & Systems Engineering Department at North Carolina A&T State University in Greensboro, NC, pursing a degree in Human Factors Engineering. His interests are in Cognitive, Quality, and Manufacturing Engineering. He received his Bachelor's degree from Tennessee State University in Nashville, TN, in Business Information Systems in 2002. He received a Master's degree in Industrial Engineering, with a concentration in Management Systems from North Carolina A&T State University in Greensboro, NC, in 2007. He is currently completing his dissertation on Risk Perception and Trust in Cyberspace. His goal is to develop a model that can help mitigate risky behavior while using the internet. Emeka can be reached at idoyeemeka@aol.com

TRANSIENT THERMAL ANALYSIS OF ELECTRIC GENERATORS

Ahmad Sleiti, Embry-Riddle Aeronautical University

Abstract

Transient thermal analysis of electric generators under realistic operating conditions and thermal losses was studied. Presented in this paper is an innovative modeling approach of the rotor, where both were modeled together, and in which the details of the thin layers of insulation and conductors were considered. A symmetrical portion of the stator and rotor was modeled and all thermal losses and boundary conditions were applied according to an operational duty cycle. It was found that there is a temperature gradient across the stator of more than 30 ^{o}C; across the rotor of more than 70 ^{o}C; and, across the whole machine of more than 100 ^{o}C. These temperature gradients could cause high thermal stresses and lead to significant reduction in the life of the machine. It is extremely important in future designs to consider reducing the temperature gradients by optimizing the design of the electric machines and using advanced cooling techniques and strategies.

Introduction

Thermal performance of electric generators in general depends on stress, rotor vibrations, and thermal behavior. Once the physical size of the machine has been established by mechanical constraints, the only remaining way by which the power output may be increased is via increases in the electrical and magnetic loadings in the stator and rotor. The implied consequential increase in the absolute level of general inefficiencies (resulting from the stator and rotor copper I^2R losses of the windings in the core and end turns, the windage and friction losses, and the iron losses) within the machine necessitates that a reliable cooling system be incorporated into the fundamental design concept. This is to ensure that the thermal losses are dissipated at temperature levels compatible with an acceptable lifespan of the electrical insulation materials used in generator construction.

Calculation of the temperature distribution in electrical machines is a complicated problem. This is due to the complicated geometry, the combination of different heat transfer modes, the rotor rotation, the on/off duty cycle, and the difficulty in calculating the thermal losses, which requires determination of the convection heat transfer coefficients and effective thermal conductivities. As a result, many researchers simplify the problem, at least in the critical components and the insulation layers of the machines.

Researchers have used several assumptions and approximations for their thermal analyses. For example, some authors consider only the stator [1-5], others only the rotor [6], [7], and yet others only the adiabatic rotor cage [8]. Some of these studies treated only the steady-state conditions [1-3], [9], [10] or the conditions with a stationary rotor [6]. In some approaches [4], [10], an equivalent thermal conductivity for slot copper and slot insulation combined was introduced.

The assumptions made about the losses are equally important. For example, in some cases, only copper losses were considered [4], [7], [8], [11]. Other assumptions, for example that temperature in the air gap is constant and independent of load, are not accurate. In many studies (e.g., Hatziathanassiou et al. [12]), iron losses and the deep bar effect were neglected. Also, 2-D models were commonly utilized because 3-D models require excessive computing time and expensive computer equipment [13]. For long-duration processes such as successive starting events, 3-D analyses are almost non-existent. It is worth noting that, although Sarkar et al. [4] at first presented a 3-D method, they later proposed and preferred a 2-D method [10], both for induction motors. A 2-D method with correct assumptions is better than a 3-D method with poor assumptions.

Researchers, such as Xypteras and Hatziathanassiou [14], have utilized Finite Element Method (FEM) to calculate the temperature distribution of an electrical machine, taking into account the iron losses and the deep-bar effect. They found that, in the case of a steady-state condition with constant losses in time, the problem is only thermal in nature. However, in the transient condition, the problem is both an electrical and thermal one, because current, losses, slip, and torque are all dependent on the temperature. The method has been developed mainly for three-phase, totally enclosed fan-cooled (TEFC), asynchronous electrical machines with negligible axial heat flows and yields accurate enough results, generally on the safe side.

Although many researchers have investigated different aspects of electric machine thermal designs, a transient analysis approach is rarely found in open literature. The objective of this current study was to simulate the thermal performance of electric machines under actual transient operational conditions, according to a predefined on/off duty cycle, which is accurately calculated and correctly models thermal losses and boundary conditions.

Problem Description

Geometry

The geometry of the electrical machine considered for this study involved a 30^o slice cross section of the generator as shown in Figure 1. The 30^o slice consisted of six stator slots and one rotor slot with a 0.02-inch gap, *t*, between them. Since there are a large number of stator slots, the rotor position with respect to the stator was considered close to the worst-case scenario because this position of the rotor, with respect to the stator, will generate the most heat loss possible due to friction.

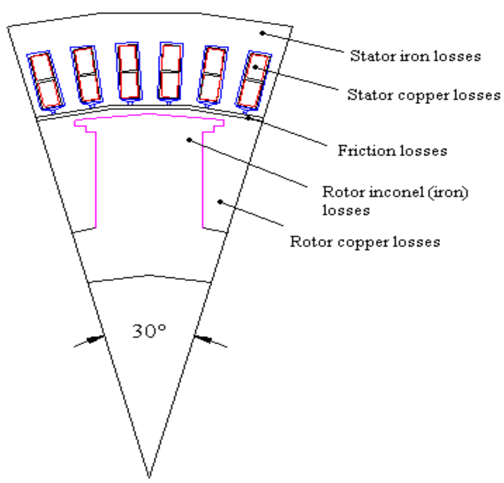

Figure 1. Symmetrical Cross-Section of the Generator under Consideration

Heat Losses

The stator and rotor copper I^2R losses of the windings in the core and end turns, the windage and friction losses, and the iron losses were considered. Stator winding losses were obtained by simple I^2R calculations with the nominal resistance corrected for temperature. There are two types of iron losses: eddy-current loss and hysteresis loss. Eddy-current loss is due to induced current, which flows in closed paths within magnetic material and is a function of the square of frequency. Hysteresis loss is the rate of change of energy used to affect magnetic domain wall motion and is a function of frequency and independent of load.

Windage loss in a generator is the power absorbed by the fluid surrounding the rotor as a result of the relative motion between the rotor and the stator. Since this absorbed power is supplied by motor or turbine and is not converted into useful energy, the presence of windage loss decreases the overall efficiency of the machine. Another undesirable characteristic of windage loss, and sometimes the most important, is that the power absorbed is converted into heat, which increases the temperature of the rotor. The power to overcome drag resistance of a rotating cylinder is given by Equation (1)

$$P = C_d \pi \rho \omega^3 r^4 l \qquad (1)$$

where,
r is the density of the fluid, in this case oil, *w* is the angular velocity, *l* is the length of the cylinder, and *r* is the radius. C_d, the friction coefficient, depends on the flow regime and the structure of the surface. In this case, the flow is laminar, so C_d is 2/*Re*, and the surface is assumed to be smooth. *Re* is the Reynolds number of the flow, given as (*rwrt)/m*, where *r* is the fluid density and *m* is the viscosity. The heat loss calculations for the case study, including the friction and windage losses, are given in Table 1.

Table 1. Thermal Losses

Item	Minimum steady state speed	Maximum steady state speed	Cruise speed	Operational conditions
Speed (RPM)	16475	21966	16974	-
Windage and friction loss (W)	2451	5810	2681	Full and no load
Stator iron loss (W)	3614	3007	3497	Full and no load
Stator I^2R loss (W)	0	0	0	No load
Stator I^2R loss (W)	24993	33005	25610	Full load
Rotor I^2R loss (W)	4046	2237	3785	No load
Rotor I^2R loss (W)	19925	15621	19251	Full load
Total loss (W)	50983	57443	51039	Full load
Efficiency	95.10%	94.60%	95.10%	Full load

The cooling oil used was Mobil DTE 790 Series. The oil inlet temperature was 93 ^{o}C, which is a typical value for aerospace applications. For stator cooling, an impingement oil cooling technique was employed, which is documented in the study by Sleiti and Kapat [15]. For rotor cooling, the oil was allowed to flow through the copper conductors, which was documented by Sleiti [16]. The stator insulation temperature must not exceed 250 ^{o}C, while the temperature of the rotor insulation material must not exceed 220 ^{o}C. This is because the insulation materials of the stator and the rotor are not capable of handling much higher temperatures. The thermal properties of the materials used are provided in Table 2.

Table 2. Thermal Properties of Materials

Material properties	Density (kg/m^3)	Specific heat (J/kg·^{o}C)	Thermal conductivity (W/m·^{o}C)
Copper	8978	381	387.6
Polyimide	1000	2000	0.385
Nomex	1000	2000	0.3
Rotor copper	8978	381	365
Hiperco50	8200	421	30
Vacuum gap	0.8	1020	0.04
Kapton	1000	2000	0.3

Duty Cycle

For the minimum, maximum, and cruise speed modes, the duty cycle consisted of 75 seconds of total running time. This included 5 seconds of full-load operation followed by 10 seconds of no-load operation, and then repeated 5 times. This kind of duty cycle is typical for aerospace applications. The duty cycle is shown in Figure 2.

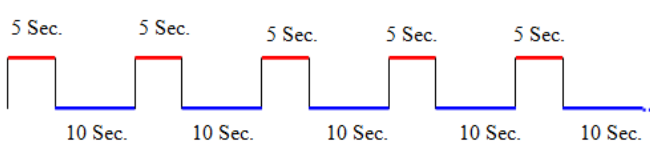

Figure 2. Duty Cycle

Cooling Techniques for Stator and Rotor

A particular area with high-heat transfer coefficients is the impingement cooling area. An array of round jets was used to cool the stator (see Figure 3). This technique has been used to cool the stator with high-heat flux and has been verified experimentally by the author [15].

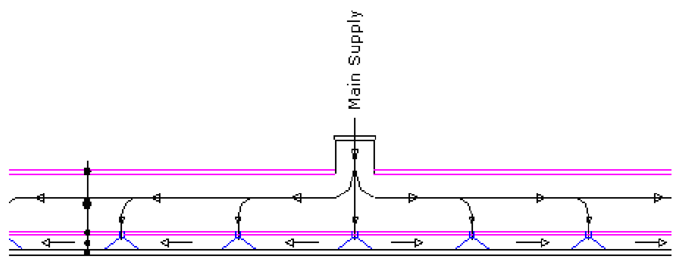

Figure 3. Stator Cooling via Impinging Jets (2-D View)

Based on the experimental results and the derived heat transfer correlation for Nusselt Number based on jet diameter ($Nu_{d)}$ in [15], the following impingement cooling design (see Table 3) for the stator was used.

Table 3. Impingement Cooling Design Parameters

Impingement nozzle diameter	2	mm
Jet-to-jet spacing	144	mm^2
Stator main oil inlet diameter	0.75	in
Stator main oil outlet diameter	1	in

The heat transfer coefficient was determined based on these parameters. In the rotor cooling system, the cooling oil was allowed to flow through rotor conductors and in the rotor-stator gap, as detailed in the study by Sleiti [16].

Heat Transfer Finite Volume Model

One symmetrical slice of 15^{o} out of 360^{o} of the full stator and rotor model was used to model the stator and rotor. The model grid was generated using a GAMBIT [17] grid generator, which is shown in Figure 4. An unstructured hybrid grid was used with at least seven grid points placed in the thin insulation layers. The final grid was adopted based on a grid convergence study. The FLUENT [17] solver package was used for the simulation. The thermal boundary conditions and assumptions are summarized in Table 4.

In addition to these conditions, heat loads were imposed as heat generation in the models. The thermal conductivity, specific heats, and density of the solids and all oil properties were taken as a function of temperature. In solid regions, the energy transport equation takes the form given by Equation (2):

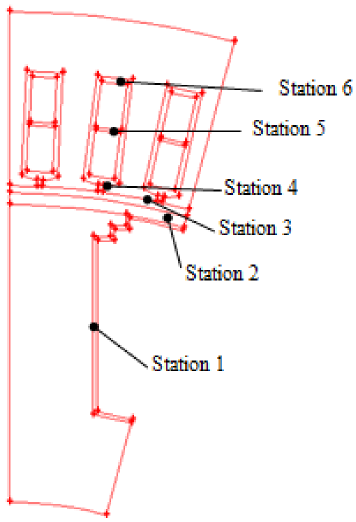

Figure 4. Geometry and Numerical Grid for Stator and Rotor Computational Model

Table 4. Thermal Boundary Conditions [16]

Coolant	Mobil DTE 790 Series oil	
Oil Inlet temperature for stator cooling	93.3	°C
Coefficient of convective heat transfer, h, at stator side	2500	W/(m$^{2.o}$C)
Coefficient of convective heat transfer, h, at rotor walls (full load operation)	1276	W/(m$^{2.}$K)*
Bulk fluid temperature for full load operation	401	K*
Coefficient of convective heat transfer, h, at rotor walls no load operation)	1364	W/(m2.K)*
Bulk fluid temperature for full load operation	390	K*

$$\frac{\partial}{\partial t}(\rho h) + \nabla \cdot (k \nabla T) + S_h = 0 \qquad (2)$$

where,
ρ is density, h is sensible enthalpy, k is thermal conductivity, T is temperature, and S_h is the volumetric heat source. The second term on the left-hand side of Equation (2) represents convective energy transfer due to rotational or translational motion of the solids. The velocity field was computed from the motion specified for the solid zone. The terms on the right-hand side of Equation (2) are the heat flux due to conduction and volumetric heat sources within the solid, respectively.

A convective heat transfer coefficient boundary condition at the stator and rotor walls was specified, and the solver used inputs of the external heat transfer coefficient and external heat sink temperature to compute the heat flux to the wall, as given in Equations (3) and (4)

$$q = h_f\left(T_w - T_f\right) + q_{rad} \qquad (3)$$

$$q = h_{ext}\left(T_{ext} - T_w\right) \qquad (4)$$

where,
h_{ext} is the external heat transfer coefficient, T_{ext} is the external heat sink temperature, and q_{rad} is the radiative heat flux.

The solver assumed a zero flux of all quantities across a symmetry boundary. There was no convective flux across a symmetry plane, and the normal velocity component at the symmetry plane was, thus, zero. There is no diffusion flux across a symmetry plane, and the normal gradients of all flow variables were zero at the symmetry plane. The symmetry boundary condition was defined as a zero normal velocity at a symmetry plane and zero normal gradients of all variables at a symmetry plane. These conditions determine a zero flux across the symmetry plane, which is required by the symmetry definition.

Results and Discussion

Figure 5 shows the temperature distribution on the stator and the rotor after a total operation time of 226 seconds for a rotor steady state speed of 16,475 rpm. At this time, the machine is in the OFF operation mode after a 75-second duty cycle and has an additional 151 seconds in OFF operation. The maximum temperature of about 191 °C was found in the stator-rotor gap, which is away from stator and rotor convective cooling.

The temperature history as a function of time was studied at six stations, which are identified in Figure 4. As shown in Figure 6, after 65 seconds, the maximum temperature of 245 °C was reached at station 5 , which is located at the stator insulation in between the conductors. At this location, the temperature increases rapidly by about 40 ºC during the 5 seconds of ON operation, and also decreases rapidly for the 10 seconds of OFF operation, though in the amount of only about 30 °C. The steady state condition was reached after about 270 seconds of total operation time, including 75 seconds of ON/OFF duty cycle and about 205 seconds of OFF operation. The same temperature history behavior at station

6 was also observed. However, the maximum temperature reached was 217 °C, compared to 245 °C at station 5.

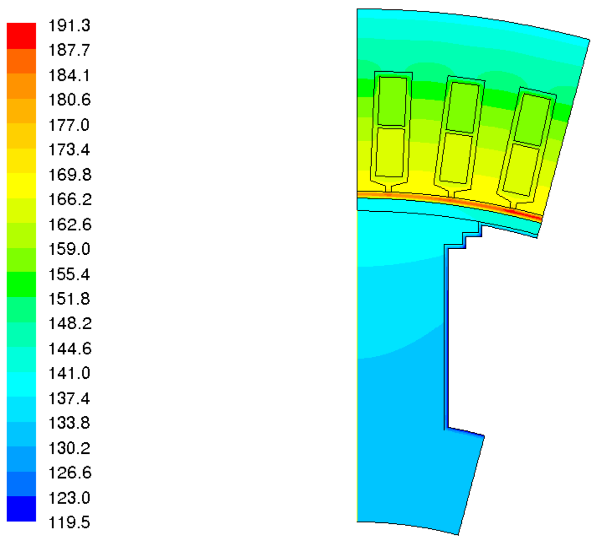

Figure 5. Temperature Distribution in Degrees Centigrade on the Stator and the Rotor after 226 Seconds

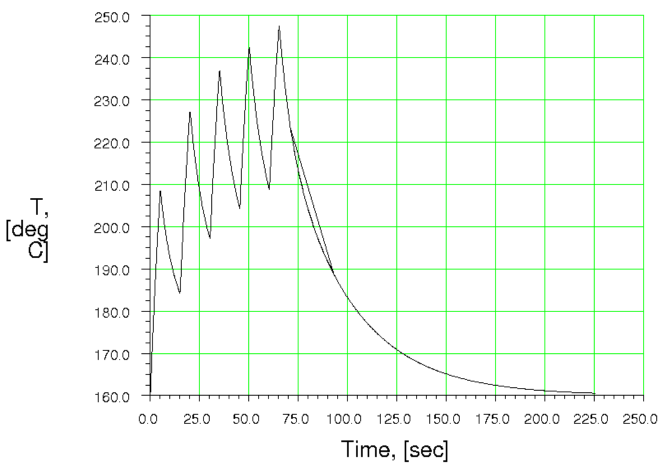

Figure 6. Temperature History at Stator Insulation (Station 5)

At station 4, which is located at the stator insulation on the rotor side, the temperature history , given in Figure 7, shows that the maximum temperature reached was about 217 °C, which is similar to the maximum temperature at station 5. Here, however, the temperature increased by only about 12 °C for the 5 seconds of ON operation and decreased by about 6 to 7 °C for the 10 seconds of OFF operation. These results show that there was an unfavorable temperature difference across the stator slots of about 30 °C, which can cause thermal stresses that degrade the stator materials and can lead to a shorter operational life of the whole machine.

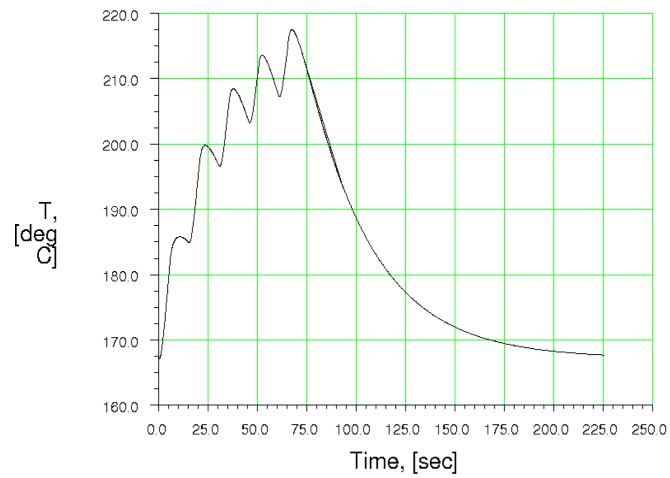

Figure 7. Temperature History at Stator Insulation (Station 4)

For the rotor, the temperature history for the given conditions was less critical compared to the stator. The maximum temperatures were found in the gap between the stator and the rotor, which is station 3, and is shown in Figure 8. The maximum temperature was about 210 °C with about a 5 °C increase for the 5 seconds of ON operation and only 2 to 3 °C decrease for the 10 seconds of OFF operation. At the top of the rotor, which is station 2, the temperature reached its maximum of about 149 °C after 70 seconds of the duty cycle, as seen in Figure 9. A temperature increase of about 2 °C for the 5 seconds of ON operation and a decrease of only 1.5 °C for the 10 seconds of OFF operation was predicted. The temperature history at station 1, not shown, is less important, with a maximum temperature of only 138 °C only after 65 seconds of operation.

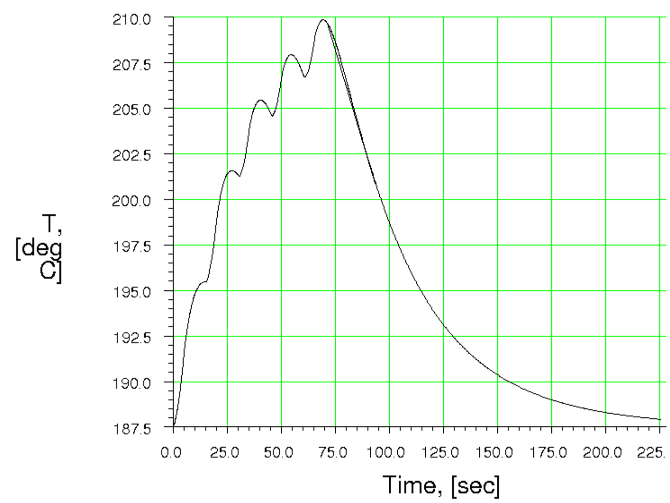

Figure 8. Temperature History at the Gap Between Stator and Rotor (Station 3)

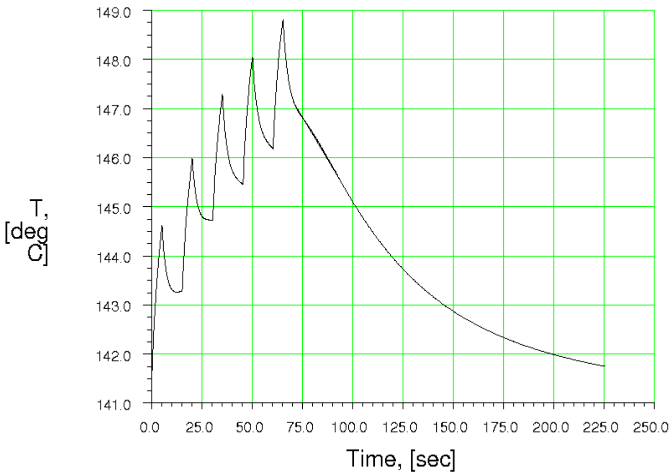

Figure 9. Temperature History at the Top of the Rotor (Station 2)

These temperature history diagrams show that there was a temperature gradient across the stator of greater than 30 ^{o}C, a temperature gradient across the rotor of greater than 70 ^{o}C, and a temperature gradient across the whole machine of greater than 100 ^{o}C. These temperature gradients could cause high thermal stresses that would cause severe reduction in the life of the machine. It is extremely important for future designs to consider reducing the temperature gradients by redesigning the machine accordingly.

Conclusion

A transient thermal analysis of electric machines was modeled reported under realistic operation conditions and thermal losses. A symmetrical portion of the stator and rotor was modeled and all thermal losses and cooling boundary conditions were applied according to an operational duty cycle. It was found that there was a temperature gradient across the stator of more than 30 ^{o}C, across the rotor of more than 70 ^{o}C, and across the whole machine of more than 100 ^{o}C. These temperature gradients could cause high thermal stresses and lead to severe reduction in the life of the machine.

The following was concluded:

- In optimizing the design of the electric machines, reducing the temperature gradients across all components must be considered.
- The duty cycle is a primary factor that determines the performance of the electric machine and the allowable thermal losses; therefore, a case-by-case study is recommended when optimizing the design of electric machines that operate in a duty cycle.
- Advanced cooling techniques, such as impingement and spray cooling for the stator, provide enhanced performance; however, more studies are required to optimize these methods. More advanced cooling techniques are to be explored in future work.

References

[1] Armor, A. F., & Chari, M. V. K. (1976). Heat flow in the stator core of large turbine-generators, by the method of three-dimensional finite elements," Part I and II. *IEEE Transactions on PAS*, PAS-95 (5), 1648 -1668.

[2] Armor, A. F. (1980). Transient, three-dimensional, finite-element analysis of heat flow in turbine generator rotors. *IEEE Transactions on PAS*, PAS-99 (3), 934-947.

[3] Ohishi, H. (1987). Analysis of temperature distribution in coil-strands of rotating electric machines with one turn coil. *IEEE Transactions on Energy Conversion*, EC-2 (3), 432-438.

[4] Sarkar, D., Mukherjee, P. K., & Sen, S. K. (1992). Temperature rise of an induction motor during plugging. *IEEE Transaction on Energy Conversion*, *7* (1), 116-124.

[5] Sarkar, D., Mukherjee, P. K., & Sen, S. K. (1993). Approximate analysis of steady state heat conduction in an induction motor. *IEEE Transaction on Energy Conversion*, *8* (1), 78-84.

[6] Griffith, J. W. (1987). Induction motor squirrel cage rotor winding thermal analysis. *IEEE Transactions on Energy Conversion*, EC-1 (3), 22-25.

[7] Garg, V. K., & Raymond, J. (1990). Magneto-thermal coupled analysis of canned induction motor. *IEEE Transactions on Energy Conversion*, EC-5 (1), 110-114.

[8] Siyambalapithiya, D. J. T. (1988). Transient thermal characteristics of induction machine rotor cage. *IEEE Transactions on Energy Conversion*, EC-3 (4), 849-854.

[9] Glises, R., Miraoui, A., & Kaufmann, J. M., (1993). Thermal modeling for an induction motor," *J. Ph. III France,* (3), 1849-1859.

[10] Gazley, C., (1958). Heat transfer characteristics of the rotational and axial flow between concentric cylinders. *Journal of Heat Transfer*, *80*, 79-90.

[11] Bastos, J. P., Cabreira, M. F. R. R., Sadowski, N., & Aruda, S. R. (1997). A thermal analysis of induction motors using a weak coupled modeling. *IEEE Transaction on Magnetics, 33*(2), 1714-1717.

[12] Hatziathanassiou, V., Xypteras, J., & Archontoulakis, G. (1994). Electrical-thermal coupled calculation of an asynchronous machine. *Archiv für Electrotechnik 77*, 122-177.

[13] Chan, C. C., Lieton, Y., Chen, P., Wang, Z., & Chau K. T. (1994). Analysis of electromagnetic and thermal fields for induction motors during stanting. *IEEE Transaction on Energy Conversion*, *9*(1), 53-60.

[14] Xypteras, J., & Hatziathanassiou, V. (1999). Thermal analysis of an electrical machine taking into account the iron losses and the deep-bar effect. *IEEE Transactions on Energy Conversion*, *14*(4), 721-727.

[15] Sleiti, A. K., & Kapat, J. S. (2006). An Experimental Investigation of Liquid Jet Array and Single Phase Spray Impingement Cooling Using Polyalphaolefin. *Experimental Heat Transfer Journal, 19*(2), 149-163.

[16] Sleiti, A. K. (2007). Advanced cooling technology for rotors of high-power low-duty cycle generators using polyalphaolefins. *Journal of Synthetic Lubrication, 24* (2), 77-90.

[17] Fluent 6.3 and Gambit documentations. Retrieved October 27, 2012, from: http://www.ipt.ntnu.no/manuals/Fluent.Inc/fluent6.3.26/help/index.htm, and http://202.118.250.111:8080/fluent/Gambit13_help/gambit.htm.

Biographies

AHMAD SLEITI is an Associate Professor of Mechanical Engineering at Embry-Riddle Aeronautical University. He earned his B.S. and MS (Mechanical Engineering, 1991) degrees from RISI University, Russia, MS (Mechanical Engineering, 2001) from University of Jordan, and Ph.D. (Mechanical Engineering, 2004) from University of Central Florida. Dr. Sleiti is currently teaching and conducting research on energy and thermofluids at Embry-Riddle Aeronautical University. He is the leader of the energy track. His interests are in thermofluids, energy harvesting, conversion, and storage systems for renewable and conventional energy sources. Dr. Sleiti may be reached at sleitia@erau.edu

INSTRUCTIONS FOR AUTHORS: MANUSCRIPT REQUIREMENTS

The INTERNATIONAL JOURNAL OF ENGINEERING RESEARCH AND INNOVATION is an online/print publication, designed for Engineering, Engineering Technology, and Industrial Technology professionals. All submissions to this journal, submission of manuscripts, peer-reviews of submitted documents, requested editing changes, notification of acceptance or rejection, and final publication of accepted manuscripts will be handled electronically. The only exception is the submission of separate high-quality image files that are too large to send electronically.

All manuscript submissions must be prepared in Microsoft Word (.doc or .docx) and contain all figures, images and/or pictures embedded where you want them and appropriately captioned. Also, for all accepted manuscripts, each figure, image or picture that was imported into your Word document must be saved individually as a **300dpi or higher JPEG (.jpg)** file and submitted separately; your manuscript and figure numbers must be used in the title of the file (e.g., **J13-F-18 Figure 4**); that means one additional file for each image imported into your manuscript. These 300dpi images do NOT need to be embedded in your manuscript. For tables or graphs created directly in Word, you do not need to submit them as separate files.

Included below is a summary of the formatting instructions. You should, however, review the sample Word document on our website (www.ijeri.org/formatting_guidelines) for details on how to correctly format your manuscript. The editorial staff reserves the right to edit and reformat any submitted document in order to meet publication standards of the journal.

The references included in the References section of your manuscript must follow APA-formatting guidelines. In order to help you, the sample Word document also includes numerous examples of how to format a variety of scenarios. Keep in mind that an incorrectly formatted manuscript will be returned to you, a delay that may cause it (if accepted) to be moved to a subsequent issue of the journal.

1. **Word Document Page Setup**: Two columns with ¼” spacing between columns; Top of page = ¾"; Bottom of page = 1" (from the top of the footer to bottom of page); Left margin = ¾"; Right margin = ¾".

2. **Paper Title**: Centered at the top of the first page with a 22-point Times New Roman (Bold), Small-Caps font.

3. **Page Breaks**: Do not use page breaks.

4. **Body Fonts**: Use 10-point Times New Roman (TNR) for body text throughout (1/8” paragraph indention); 9-point TNR for author names/affiliations under the paper title; 16-point TNR for major section titles; 14-point TNR for minor section titles; 9-point TNR BOLD for caption titles for tables and figures; other font sizes as noted in the sample document.

5. **In-text Referencing**: List and number each reference when referring to them in the body of your document (e.g., [1]). The first entry must be [1] followed by [2], [3], etc., continuing in numerical order to the final entry in your References section. Again, see the sample Word document for specifics. Do not use the End-Page Reference utility in Microsoft Word. You must manually place references in the body of the text.

6. **Tables and Figures**: Center all tables and figures. Captions for tables must be above the table, while captions for figures are below; all captions are left-justified.

7. **Page Limit**: Manuscripts should not be more than 15 pages (single-spaced, 2-column format).

8. **Page Numbering**: Do not use page numbers.

9. **Publication Charges:** Manuscripts accepted for publication are subject to mandatory publication charges.

10. **Copyright Agreement:** A Copyright Transfer Form must be signed and submitted by all authors on a given paper before that paper will be published.

11. **Submissions:** All manuscripts and associated files must be submitted electronically.

    MANUSCRIPTS should be submitted to Dr. Philip D. Weinsier, manuscript editor, at philipw@bgsu.edu along with a copy to editor@ijeri.org.

    FILES containing your high-quality images should ONLY be submitted to philipw@bgsu.edu.

The International Journal of Engineering Research & Innovation (IJERI) is the second official journal of the International Association of Journals and Conferences (IAJC). IJERI is a highly-selective, peer-reviewed print journal which publishes top-level work from all areas of engineering research, innovation and entrepreneurship.

IJERI Contact Information

General questions or inquiry about sponsorship of the journal should be directed to:

Mark Rajai, Ph.D.

Founding and Editor-In-Chief

Office: (818) 677-5003

Email: editor@ijeri.org

Department of Manufacturing Systems Engineering & Management

California State University-Northridge

18111 Nordhoff St.

Room: JD3317

Northridge, CA 91330